

# **COMSAT**

## **Technical Review**

Volume 15 Number 1, Spring 1985

*Advisory Board* Joseph V. Charyk  
John V. Evans  
William W. Hagerty  
John L. McLucas

*Editorial Board* Geoffrey Hyde, Chairman  
Richard A. Arndt  
Ali E. Atia  
S. Joseph Campanella  
Dattakumar M. Chitre  
Russell J. Fang  
Howard W. Flieger  
Ivor N. Knight  
Robert K. Kwan  
David W. Lipke  
William P. Osborne  
Larry C. Palmer  
Edward E. Reinhart  
David V. Rogers  
Hans J. Weiss  
Albert E. Williams  
Pier L. Bargellini, Editor Emeritus

*Editorial Staff* Daniel N. Crampton,  
MANAGING EDITOR  
Margaret B. Jacocks  
Judith A. Lewis  
Barbara J. Wassell  
TECHNICAL EDITORS  
Edgar Bolen  
PRODUCTION  
Shirley T. Cofield  
CIRCULATION

COMSAT TECHNICAL REVIEW is published twice a year by Communications Satellite Corporation (COMSAT). Subscriptions, which include the two issues published within a calendar year, are: one year, \$10 U.S.; two years, \$15; three years, \$20; single copies, \$7; article reprints, \$1.50. Air mail delivery is available at an additional cost of \$10 per year. Make checks payable to COMSAT and address to Treasurer's Office, Communications Satellite Corporation, 950 L'Enfant Plaza, S.W., Washington, D.C. 20024-2198, U.S.A.

© COMMUNICATIONS SATELLITE CORPORATION 1985  
COMSAT IS A TRADE MARK AND SERVICE MARK  
OF THE COMMUNICATIONS SATELLITE CORPORATION

## COMSAT TECHNICAL REVIEW

### Volume 15 Number 1, Spring 1985

- 1** AERONAUTICAL SATELLITE DATA LINK STUDY **W. Sandrin, H. Chen, W. Haggmann, K. Mackenthun, and S. Rhodes**
- 39** AN L-BAND ACTIVE ARRAY SYSTEM FOR GLOBAL COVERAGE **S. Siddiqi, A. I. Zaghoul, S. M. Chou, and R. E. Eaves**
- 71** FADE DURATION STATISTICS FROM COMSTAR 20/30-GHZ BEACON MEASUREMENT PROGRAM **P. N. Kumar**
- 89** A FIELD TEST FOR COMPANDED SINGLE SIDEBAND MODULATION: IMPLICATIONS FOR CAPACITY ENHANCEMENT AND TRANSMISSION PLANNING **E. Wallace, C. Adams, and D. Arnstein**
- 113** FORMATION OF HIGH-QUALITY N-LAYERS IN GAAS BY ION IMPLANTATION **P. J. McNally**
- 127** SIMULATION OF DEPLOYMENT DYNAMICS FOR INTELSAT VI TRANSMIT AND RECEIVE BOOM/ANTENNA SYSTEMS **P. K. James**
- 149** CTR NOTE: GEOSTATIONARY SATELLITE LOG **C. H. Schmitt**
- 179** TRANSLATIONS OF ABSTRACTS  
FRENCH 179 SPANISH 183
- 187** AUTHOR INDEX, CTR 1984
- 190** INDEX OF 1984 PUBLICATIONS BY COMSAT AUTHORS

# ***Aeronautical satellite data link study***

W. SANDRIN, H. CHEN, W. HAGMANN,  
K. MACKENTHUN, AND S. RHODES

(Manuscript received May 21, 1984)

## ***Abstract***

A system is described that can provide data communications via L-band satellite to transoceanic commercial aircraft. This system will provide both air traffic control and company communications data services. The modest satellite capacity that is required can be provided by the INMARSAT space segment. Besides the cost benefits obtained through the shared use of satellites and earth stations in the INMARSAT system, a design that minimizes aircraft equipment costs is also described. This design feature is achieved in part by the use of low-gain, flush-mounted, aircraft antennas. Low data rates are assumed (200 to 400 bit/s) by using differential phase-shift keying (DPSK) modulation and a rate  $\frac{1}{2}$  convolutional code with interleaved code symbols and soft detection Viterbi decoding. This modulation/coding scheme was chosen to allow reliable operation in the multipath fading environment. After a summary description of the recommended system, this paper examines propagation, aircraft antenna, modulation and coding, acquisition and synchronization, and network design issues.

## ***Introduction***

It has long been recognized that improvements in communications capabilities would be highly beneficial for trans-oceanic commercial aircraft.

A continuous communications system would result in improved air traffic control (ATC), making possible a reduction in flight separation standards in

heavily used airspace, such as the North Atlantic region. Such a system would result in substantial fuel cost savings. Also, an improved ATC system would verify aircraft navigation system operation by constantly comparing position reports with intended flight paths, thus permitting instant emergency communications. This communications link could also permit much needed company communications and public correspondence services.

A satellite communications system is a logical choice for such a system, and the International Maritime Satellite Organization (INMARSAT) system offers a unique opportunity for introducing aeronautical satellite data communications. Sharing satellites and earth stations would permit flexible, incremental services by ocean region as requirements demand.

Early efforts conducted in the mid-1970s to establish an aeronautical satellite system (AEROSAT) were terminated because of the high cost of a dedicated aeronautical system. Recently, however, there has been renewed interest in such a system [1],[2], based on the shared use of space segments. It has been determined that both space segment and aircraft-terminal design requirements can be reduced from the initial estimate made for AEROSAT because of lower data rates and the exclusion of voice links. Because of these factors and the adjacent allocation of L-band frequencies for maritime and aeronautical mobile satellite services, the shared use of INMARSAT facilities has become economically attractive.

If satellites are to be used for ATC and company communications, their use will be contingent on a low-cost approach. The system concept described in this paper is the result of a study conducted at COMSAT Laboratories to investigate a practical and economical implementation of an aeronautical satellite data-link service.

An aeronautical satellite data system would have two main purposes:

- a. to ensure improved communications for ATC and
- b. to provide company communications and public correspondence.

In a study conducted by SRI International [3], it was estimated that a total average information rate of about 90 bit/s for the forward (ground-to-air) link and about 300 bit/s for the return (air-to-ground) link would be needed to meet ATC requirements in the North Atlantic region through the year 2005. (As discussed below, these rates are not the same as the individual carrier transmission rates for the forward and return links.) This estimate was based on a peak instantaneous count in the North Atlantic region of 210 to 230 aircraft, with polling required for each aircraft once every 5 min., or once every 0.5 min. when aircraft are in proximity. It is assumed that 70 aircraft will require polling at 30-s intervals and that a maximum of 60 aircraft per

hour will enter the network. At that rate, close to 200 messages per minute would be transmitted in each direction.

Typical ATC messages include position requests and reports, altitude clearance requests and acknowledgments, meteorological reports, rerouting requests and clearance messages, waypoint verifications, heading information, traffic reports, and emergency messages.

Data transmission requirements for company and public correspondence communication services are difficult to project, but the architecture of the system described here permits the growth of these services through multiple, low data-rate carriers and through multiple earth stations with direct access to the system.

The primary objective in designing the system described here is keeping costs to the users as low as possible. This objective is achieved in a system design with the following key features:

a. *Low-Gain Aircraft Antennas.* Two requirements of the aircraft antenna are that it have very little drag penalty and be inexpensive to install. In this system, an aircraft antenna gain requirement of 0 dBi (circularly polarized) is assumed over 90 percent of azimuth for elevation angles above 10°. As discussed below, microstrip patch configurations are a preferred solution to this requirement.

b. *Low Data-Rate Transmissions.* To minimize aircraft terminal costs and satellite power requirements, low data-rate signals would be used; additional carriers would be transmitted as the requirements increased. A basic transmission data rate of 200 bit/s for the forward (ground-to-aircraft) link, and either 200 or 400 bit/s for the return link are assumed. The forward link consists of a continuous time-division multiplexed (TDM) carrier; the return link operates in a time-division multiple-access (TDMA) burst mode. Multiple carriers on both the forward and return links are used to satisfy ATC and other data communications traffic requirements. Because the resulting network structure and power levels are not unlike the INMARSAT maritime system, the effect of the space segment on a shared system can be minimized.

c. *Protection Against Multipath Fading.* A modulation/coding scheme is planned that can be easily implemented and provide protection against the effects of multipath fading (discussed below). Multipath effects can be minimized by using an aircraft antenna equipped with either a narrow beam, and/or adaptive null formation techniques, which can reduce the carrier-to-multipath (C/M) ratio. In this application, however, simple antennas are dictated by cost and operational factors, and power budgets do not allow for the high fading margin required if no anti-multipath

provisions are made. Hence, a coding/interleaving scheme has been selected to combat multipath effects. This scheme consists of forward error correction (FEC) coding with symbol interleaving. In the system described here, a rate 1/2 convolutional FEC code is used along with Viterbi decoders with soft decision. The modulation used is DPSK.

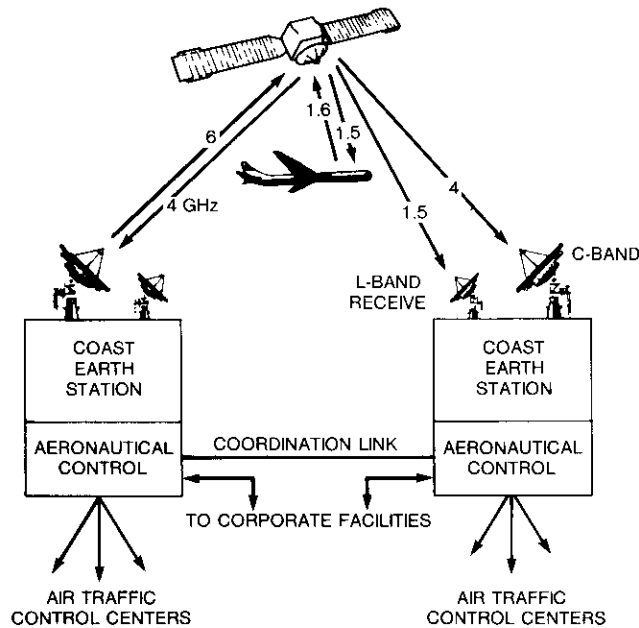


Figure 1. Network Configuration

Figure 1 illustrates the basic system configuration, and Figure 2 shows the frequencies that have been allocated for this service.

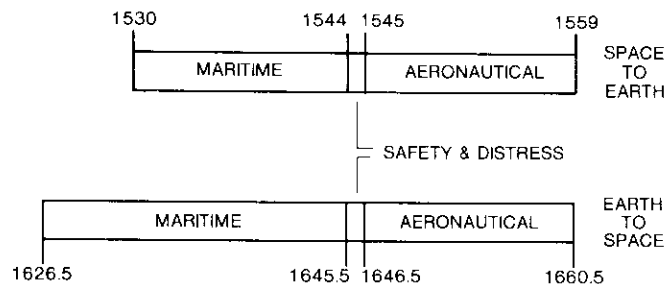


Figure 2. Allocations to the Mobile Satellite Services (MHz)

### Link budgets

Link budgets for the recommended system are shown in Tables 1 and 2. The data rate of 200 bit/s for forward and return links was selected on the basis of system traffic requirements and link parameter considerations. A rate of 400 bit/s for the return link may also be a practical choice, depending on satellite characteristics and aircraft terminal performance. With multiple carriers, however, system capacity is not limited if a transmission rate of 200 bit/s is selected.

TABLE 1. EXAMPLE OF FORWARD LINK BUDGET (200-bit/s LINK)

LINK PARAMETER	VALUE
<b>Ground-to-Satellite Link (6.4 GHz)</b>	
e.i.r.p.	61.4 dBW
Miscellaneous Random Losses	1.1 dB
Atmospheric Loss	0.2 dB
Freespace Loss	200.5 dB
Satellite Gain-to-Noise Temperature	- 15.0 dBi/K
Boltzmann's Constant	- 228.6 dBW/(Hz-K)
Up-link $C/N_o$	73.2 dB-Hz
<b>Satellite-to-Aircraft Link (1.54 GHz)</b>	
e.i.r.p.	20.8 dBW
Freespace Loss	188.4 dB
Ionospheric Scintillation	0.2 dB
Atmospheric Loss	0.2 dB
Polarization Loss	0.3 dB
Aircraft Noise (412.3 K)	26.2 dBK
Aircraft Antenna Gain	0.0 dBi
Boltzmann's Constant	- 228.6 dBW/(Hz-K)
Down-Link $C/N_o$	34.1 dB-Hz
<b>Combined Link</b>	
Combined Up- and Down-Link $C/N_o$	34.1 dB-Hz
Symbol Rate (Bit Rate = 200 bit/s, Code Rate = 1/2)	400.0 symbol/s
Combined Up- and Down-Link $E_s/N_o$	8.1 dB
Assumed $C/M$ (Intermodulation)	15.0 dB
Available $E_s/N_o$ for Direct Path	7.3 dB
Required Direct Path $E_s/N_o$ in Presence of Multipath ( $C/M = 10$ dB) for Decoded Bit Error Rate of $10^{-5}$	6.3 dB
Difference Between Available and Required $E_s/N_o$ †	1.0 dB

\* Because of coding/interleaving, the effect of multipath interference is included as a detection performance loss, as discussed in the text. For this reason, fading margin is not included in the link budget.

† A 1.0-dB margin is assumed to allow for unforeseen impairments.

TABLE 2. EXAMPLE OF RETURN BUDGET  
(200-bit/s LINK)

LINK PARAMETER	VALUE
<b>Aircraft-to-Satellite Link (1.64 GHz)</b>	
Aircraft Transmitter Power	11.5 dBW
Cable, Diplexer (if needed) and Miscellaneous Losses	1.5 dB
Aircraft Antenna Gain	0.0 dBi
Freespace Loss	188.9 dB
Atmospheric Loss	0.2 dB
Scintillation Loss	0.2 dB
Polarization Loss	0.3 dB
Satellite Gain-to-Noise Temperature	-15.0 dBi/K
Boltzmann's Constant	-228.6 dBW/(Hz-K)
Up-link $C/N_o$	34.0 dB-Hz
<b>Satellite-to-Earth Station Link (4.2 GHz)</b>	
Satellite Transponder Gain (equivalent to MARECS SAR High Gain Mode)	138.5 dB-m <sup>2</sup>
Satellite e.i.r.p.	-19.6 dBW
Freespace Loss	197.1 dB
Miscellaneous Random Losses	1.1 dB
Atmospheric Loss	0.3 dB
Earth Station Gain-to-Noise Temperature	32.2 dBi/K
Boltzmann's Constant	-228.6 dBW/(Hz-K)
Down-Link $C/N_o$	42.7 dB-Hz
<b>Combined Link</b>	
Combined Up- and Down-Link $C/N_o$	33.5 dB-Hz
Symbol Rate (200 bits/s, Rate 1/2 Code)	400.0 symbol/s
Combined Up- and Down-Link $E_s/N_o$	7.5 dB
Assumed $C/IM$ (Intermodulation)	20.0 dB
Available $E_s/N_o$ for Direct Path	7.3 dB
Required Direct Path $E_s/N_o$ in Presence of Multipath ( $C/IM = 10$ dB) for Decoded Bit Error Rate of $10^{-5}$ *	6.3 dB
Difference Between Available and Required $E_s/N_o$ †	1.0 dB

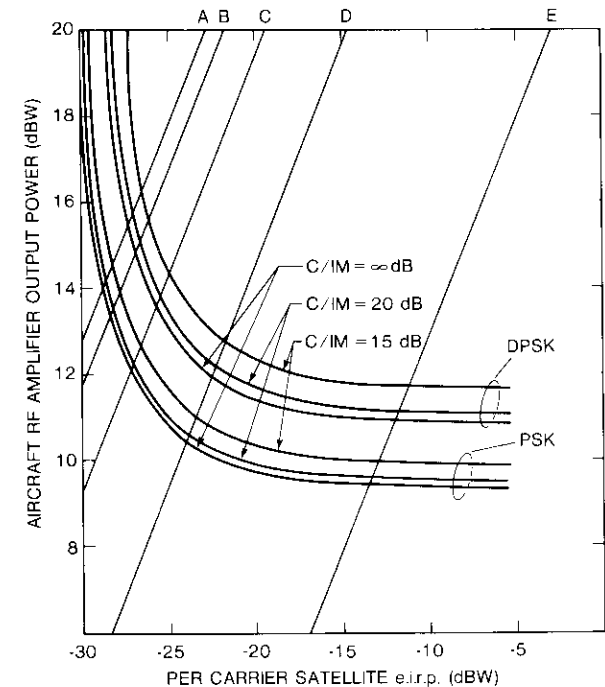
\* Because of coding/interleaving, the effect of multipath interference is included as a detection performance loss, as discussed in the text. For this reason, fading margin is not included in the link budget.

† A 1.0-dB margin is assumed to allow for unforeseen impairments.

Because of the coding/interleaving scheme, multipath interference is accounted for in Tables 1 and 2 as a modem performance loss (as discussed in the section on modulation); therefore, a separate fading margin entry is not included. The penalty resulting from multipath fading is 1 dB with the assumed coding/interleaving scheme. By comparison, for a conventional

DPSK system with Ricean fading and a C/M of 10 dB, a margin of 5.8 dB would be required to ensure that the received level is above a specified level for greater than 99 percent of the time, and that a margin of 12.9 dB is maintained for 99.99 percent of the time.

Figure 3 shows that the selection of transponder gain is an important parameter in optimizing the performance of the return link. If the satellite gain is too low, the link is down-link (satellite-to-earth station) limited, and the aircraft's equivalent isotropically radiated power (e.i.r.p.) required to maintain a certain link quality becomes too high. Conversely, if the satellite gain is too high, the overall link is up-link (aircraft-to-satellite) limited,



CONSTANT SATELLITE TRANSPONDER GAIN CONTOURS (LINEAR REGION):  
 A—SECOND GENERATION INMARSAT DRAFT RFP—NOMINAL 122.5 dB·m<sup>2</sup>  
 B—MARISAT SPECIFICATION—HIGH GAIN ≈ 123.5 dB·m<sup>2</sup>  
 C—INTELSAT V MCS HIGH GAIN SPECIFICATION ≈ 126.0 dB·m<sup>2</sup>  
 D—GOOD CHOICE FOR DPSK, C/M = 20 dB 130.8 dB·m<sup>2</sup>  
 E—SECOND GENERATION INMARSAT DRAFT RFP HIGH GAIN SETTING—HIGH GAIN TRANSPONDER 142.5 dB·m<sup>2</sup>

Figure 3. Aircraft RF Power for Return Link

and an unnecessarily large satellite e.i.r.p. per carrier is needed. Although Figure 3 gives the required power for both PSK and DPSK, as discussed later, DPSK is the preferred modulation technique because of carrier synchronization considerations.

Also shown in Figure 3 are lines of constant satellite transponder gain for various satellite transponders. The required aircraft RF amplifier power is obtained by the intersection of a curve and a line of constant transponder gain—the minimum power required to support the assumed quality of transmission (decoded  $P_e = 10^{-5}$ ), operating with a satellite of that gain. Line D in Figure 3 represents a value of satellite transponder gain that would be a good choice for this system.

Other factors that may influence the selection of the aircraft RF power amplifiers are expense, power consumption, and heat dissipation. The values of required RF amplifier power shown in Figure 3 (less than 100 W) are well below those possible with state-of-the-art L-band amplifier technology.

### **Multipath propagation characteristics**

Multipath fading can be a major impairment in an aeronautical mobile satellite service for transoceanic regions, since the intended aircraft antennas will have low gain and broad patterns, thus providing little pattern protection to the reflected energy, especially at low elevation angles.

During the early and mid-1970s, comprehensive analytical and experimental investigations of oceanic aeronautical satellite L-band links were conducted [4]–[6]. From these and other investigations [7]–[11], the following points summarize the multipath propagation characteristics assumed in this study:

- a. For elevation angles above  $10^\circ$ , multipath fading is essentially a diffuse process that can be modeled with Ricean statistics, with little variation caused by different sea states [4]–[6].
- b. For a low-gain, circularly polarized antenna, a worst-case  $C/M$  ratio of 10 dB occurring at an elevation angle of  $10^\circ$  (the limit of coverage) can be assumed. This value has been taken as a basis for link parameters and for the selection of a modulation/coding technique.
- c. The maximum decorrelation time (resulting from Doppler spread) will be 20 ms. This value is important in determining how long coded symbols must be interleaved.
- d. The coherence bandwidth (resulting from differential delay) can be as high as 400 kHz.

The approach to multipath propagation in this study has been to adopt a limiting multipath condition upon which the system design and design trades

are based. This is, multipath propagation data and antenna performance data have been used to determine the probable worst-case multipath fading characteristics, which in turn have been used in the design of the modulation, coding, and network control schemes.

Although most available multipath propagation data are evaluated in terms of linearly polarized components, the polarization assumed for the recommended system is circular. For this reason, the available propagation had to be evaluated in terms of parameters relevant to this study, since  $C/M$  is highly sensitive to polarization, antenna characteristics, and elevation angle. However, polarization does not significantly alter delay spread, coherence bandwidth, Doppler spread, or decorrelation time characteristics. For those parameters, therefore, the results presented in Reference 1 were assumed to be directly applicable to this study. The decorrelation time of 20 ms noted above is based on extrapolation of a worst-case, 3-dB decorrelation time value of 10 ms (i.e., assuming that the decorrelation time function has a Gaussian shape, the decorrelation value at 20 ms is approximately 20 dB).

To determine the worst-case level of  $C/M$  for which the system should be designed, emphasis was placed on a  $10^\circ$  elevation angle, for which it was determined that a  $C/M$  value of 10 dB would be conservative; this value was then selected for system design purposes. Consideration was also given to higher elevation angles, but it was concluded that  $C/M$  values worse than 10 dB were unlikely to occur at any elevation angle.

Figure 4 illustrates coverage regions, as suggested in References 3 and 12, and gives elevation angle contours of  $5^\circ$ ,  $10^\circ$ , and  $15^\circ$  for a satellite at  $26^\circ\text{W}$ . Calculations have shown that with the exception of the region north of Iceland, coverage of the North Atlantic region (with minimum elevation angles of about  $15^\circ$ ) can be obtained over a fairly large range of subsatellite longitudes.

### **Aircraft antennas**

In this system, the aircraft antenna must be kept as simple as possible: its installation must be simple and its aerodynamic drag must be as small as possible. To achieve these objectives, the performance required of the aircraft antenna has been specified at a minimum of 0-dBi gain (with respect to circular polarization) for elevation angles above  $10^\circ$ , over 90 percent of azimuth. In the design of the overall system, transmission rates and modulation/coding/interleaving schemes were selected that permitted the use of an antenna with such a low gain and a relatively small amount of multipath rejection.

Several candidate antenna types, some of which have been previously developed for aeronautical satellite communications, were examined in the

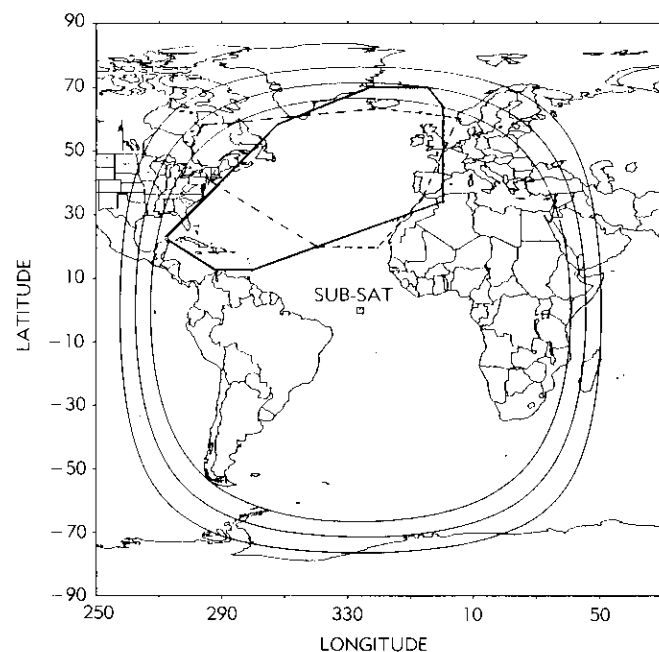


Figure 4. *Satellite Coverage for North Atlantic*

initial phase of the study. The summarized results shown below suggest the use of microstrip radiators in a multiple antenna or in a phased-array configuration because they can be flush mounted without cutting large holes in the aircraft skin, and they have acceptable electrical performance. For this reason, most of the antenna study concentrated on microstrip antennas.

#### **Aircraft antenna survey**

Antennas that may be suitable for this application can be divided into two categories: those formed by a single antenna element, and those consisting of multiple antennas. The single-element antennas include bent, crossed-dipole antennas [13], cavity-backed spirals [14], cavity-backed cross-slots [15], slot-dipole antennas [16], and microstrip patch antennas [17]. A summary of the characteristics of these antennas, presented in Table 3, shows that only the bent, crossed-dipole antenna can achieve the desired objective of more than 0 dBi above a  $10^\circ$  elevation angle.

The bent, crossed-dipole antenna consists of two orthogonal dipole elements driven in phase quadrature to provide circular polarization. The complete

antenna, approximately 1.5 in. high, must be mounted at least 2 in. above the fuselage to minimize the effects of the metallic aircraft skin on the elevation pattern, resulting in a total height of approximately 3.5 in.

Aircraft design specialists helped estimate that a small, dome-like radome, 3.7 in. high and 4 in. wide at the base (dimensions required for a bent, crossed-dipole design), top mounted on a Boeing 747 behind the flight deck, would result in an increased drag of 0.04 percent, equivalent to an increase in empty operating weight of around 200 lb (or about one passenger). Assuming 3,550 flight hours each year, this would result in an annual fuel penalty of about 5,000 gallons. Because of the drag penalty associated with even a small radome, microstrip patch antennas, which can be flush mounted without cutting large holes in the aircraft's body, were considered instead.

#### **Microstrip antenna configurations**

Because the radiation pattern of a microstrip radiator is not wide enough to provide a 0-dBi gain within the required coverage, multiple antenna systems must be used. To verify the feasibility of this design concept, detailed coverage computations were made on several possible configurations by using the computed pattern of a microstrip patch antenna element [18]. Analytic models representing good, first-order approximations were used so that the performance of various configurations could be compared.

The configurations investigated were as follows:

- a. Single-element/multiple-switched antennas. This included two (side-mounted) or three (top- and side-mounted) antenna configurations, with each antenna consisting of one microstrip radiator.
- b. Multiple-element/multiple-switched antennas. Similar to configuration (a) except that each antenna is a linear array formed by two or three microstrip radiating elements.
- c. Top-mounted, electrically steerable, linear phased arrays consisting of two or three elements.

Since a single microstrip radiating element extends its 0-dBi coverage only down to a  $20^\circ$  elevation, as shown in Table 3, configuration (a) always incurs a gain deficiency in the nose and tail direction while having large overlapped coverage in the wing directions. By replacing the single radiating element with a linear array of two or three radiating elements that have been mounted circumferentially on the fuselage, as in configuration (b), the radiation pattern in the roll plane is narrowed, minimizing the overlapped coverage and improving gain in the fore and aft directions. Compared with a two-element array, the three-element array offers design flexibility, since the excitation

TABLE 3. CHARACTERISTICS OF SINGLE ANTENNA ELEMENTS

ANTENNA TYPE	SIZE* (in.)	BEAMWIDTH (3-dB BANDWIDTH) (deg)	ELEVATION ANGLE (2 dBi) (deg)	ELEVATION ANGLE (0 dBi) (deg)	GAIN AT 10° ELEVATION (dBi)
Crossed Dipole	4 × 4 × 4	110	14	8	1
Crossed-Slot	H > 4, D = 6			45	
Spiral	H = 2.5, D = 9	70 to ~80	45	40	-4
Slot Dipole	H ~ 2.5		50	40	
Microstrip Patch	H < 0.25, D < 4	80	35	20	-3

\* H = height; D = diameter.

distribution can produce a shaped beam optimized for a particular antenna location. A three-element array also generates a sharper gain slope than a two-element array, thereby providing better multipath rejection. Four-element arrays were not considered because the array radiation pattern is so narrow that four antenna locations are needed for complete coverage.

An alternate approach to the multiple antenna system of configuration (b) is configuration (c), a top-mounted electrically steerable phased array, which provides multiple-switched beams. Unlike the multiple antenna system, which requires interconnect cabling, a small, top-mounted phased array has the significant advantage of a single mounting location. The gain coverage of a uniformly excited, three-element, linear phased array is illustrated in Figure 5 for a 0° beam (dashed lines) and a 48° beam (solid lines). Even though the coverage of this configuration does not quite meet the requirement, it does demonstrate the potential of a small, top-mounted phased array as a likely candidate, given that the design is optimized for number of elements, element location, and excitation.

It was concluded that a small, three- or four-element, top-mounted, planar phased array could be designed to meet the desired objectives. Such an array would have a simple, multiport feed network that would be controlled by automatic switching. This configuration is clearly more desirable from the standpoint of cost and installation than a two- or three-location switched antenna system.

### Modulation and coding

In this system, not only is the available  $C/N_o$  for the direct link between satellite and aircraft restricted to a low value, but multipath interference,

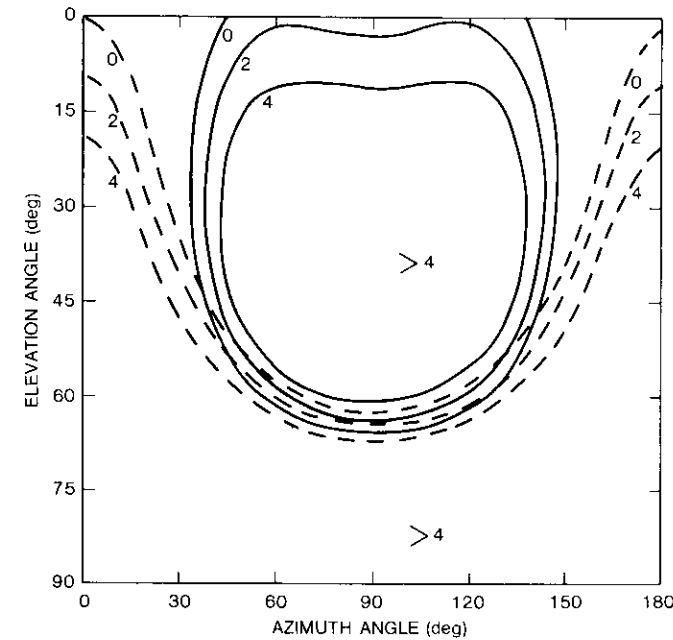


Figure 5. Radiation Pattern for Top-Mounted, Three-Element Linear Phased Array

which can cause the composite signal to fade to even lower  $C/N_o$  values, is also present. Moreover, at the low-modulation symbol rates of interest and the high (1.5 to 1.6 GHz) carrier frequencies, frequency stability and phase noise are also important factors. Further, the transmissions are affected by Doppler shift caused by terminal and satellite motion.

Several modulation types were considered for their theoretical performance and applicability to the aeronautical satellite channel. Because of the low values of  $C/N_o$  and the requirement of a bit error probability,  $P_b$ , of  $10^{-5}$ , various FEC coding schemes were also investigated.

Modulation and FEC coding cannot be treated independently, since the  $E_b/N_o$  at which the modem must operate is a function not only of the modulation but also of the coding. A combination of DPSK and convolutional FEC coding with Viterbi decoding of soft-detected code symbols was chosen as the recommended modulation/coding technique.

The best way to achieve low  $P_b$  at low  $E_b/N_o$  requires a method of randomizing the multipath interference so that it appears noise-like rather than impulsive, along with efficient modulation and FEC coding. Certain

systems can employ frequency diversity to combat fading, or spread-spectrum coding to randomize multipath interference. At the low modulation symbol rates,  $R_s$ , of interest here, the fading correlation bandwidth is too large (as high as 400 kHz) for such methods to be practical. However, because interleaving of transmitted symbols can be very practical for the randomization of multipath interference, it was the technique selected for this system.

### Modulation considerations

It is essential that the modem used for the aircraft units be simple and cheap. Consequently, binary modulations are desirable. The binary modulations of interest include PSK, DPSK, and incoherent frequency shift keying (FSK) with orthogonal tone spacings. For multilevel or  $M$ -ary signaling, only MFSK, with orthogonal tones and incoherent detection, is considered. Figure 6 depicts the ideal performances of these modulations for a channel impaired only by additive white Gaussian noise (AWGN).

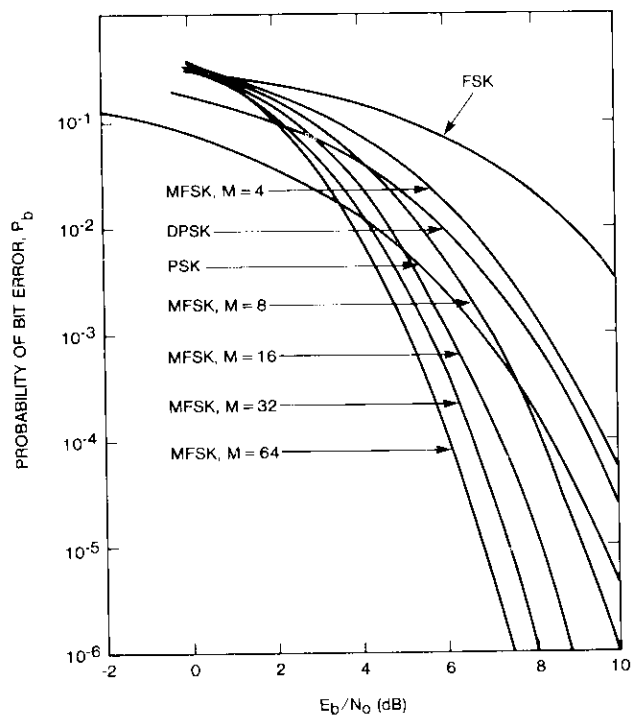


Figure 6. Detection Performances for Different Modulations Transmitted Over AWGN Channel

Because of its superior power efficiency for binary modulation, PSK would be the most desirable choice if the symbol rate  $R_s$  were sufficiently high so that coherence could be maintained over many symbol intervals. With the dynamic channel conditions of multiplicative noise from oscillators and Doppler spread of the multipath interference, the received carrier phase may change too rapidly for reliable carrier phase synchronization to be obtained. Thus, the question of carrier synchronization makes PSK a somewhat risky choice at the low  $R_s$  values of 200 to 800 symbols per second.

For good detection performance with DPSK, the carrier phase must be quasi-static only over one or two symbol intervals. Also, the theoretical detection performance is only slightly worse than that for PSK, and it has a perfect coherent phase reference. Because DPSK does not require a coherent phase reference from carrier synchronization, its performance is not nearly as sensitive to channel dynamics as that of PSK. Therefore, DPSK appears to be a good choice for the aeronautical application.

FSK is less sensitive than DPSK to channel dynamics, but its poor performance disqualifies FSK as a good choice. MFSK can perform well for large  $M$ , but its implementation is unduly complicated.

### Channel parameters

As discussed previously, it is assumed that the multipath is a diffuse signal. Hence, the multipath can be modeled as individual quadrature components that are Gaussian with a zero mean and a variance of  $\sigma_I^2$ . Thus, the average multipath interference power level of  $S_I = 2\sigma_I^2$ . With  $S_D$  used to denote the received power level of the direct transmission, the composite signal is Ricean with power  $S_D + S_I$  and a signal-to-interference power ratio of  $\gamma$ , which is defined as the "Rice factor."

$$\gamma \triangleq \frac{S_D}{S_I}$$

The Rice factor (in decibels) is

$$\Gamma = 10 \log \gamma$$

As discussed previously, a value of  $\Gamma = 10$  dB is assumed, corresponding to  $\gamma = 10$ .

Fade level is defined as the difference  $\beta$  between the power level,  $S_D$ , of the direct transmission and the instantaneous power,  $S_C$ , of the composite transmission (direct plus indirect).

$$\beta = S_D - S_C$$

Corresponding to any given fade margin  $B = 10 \log \beta$ , is an "outage" probability  $P_f$  from fading. Table 4 gives  $B$  for different  $P_f$ , parametric in the Rice factor. For  $\Gamma = 10$  dB, an outage probability of only 0.01 will require a fade margin of almost 6 dB.

TABLE 4. REQUIRED FADE MARGIN vs OUTAGE PROBABILITY FROM FADING PARAMETRIC IN RICE FACTOR

OUTAGE PROBABILITY ( $P_f$ )	REQUIRED FADE MARGIN $B$ (dB) (RICE FACTOR $\Gamma = 10 \log \gamma$ )				
	6 dB	8 dB	10 dB	12 dB	14 dB
0.100	4.05	3.25	2.58	2.05	1.62
0.050	5.88	4.59	3.56	2.77	2.17
0.020	8.45	6.38	4.82	3.68	2.83
0.010	10.57	7.81	5.77	4.34	3.30
0.005	12.90	9.30	6.73	4.98	3.75
0.002	16.02	11.50	8.05	5.84	4.34
0.001	19.02	13.35	9.10	6.49	4.78

The multipath channel fading dynamics are determined by the Doppler "spread," which is the Fourier transform of the time autocorrelation function. By using an upper limit of 10 ms for the 3-dB fading decorrelation time (as reported in Reference 4), and assuming a Gaussian-shaped fading spectrum, the fading from multipath interference should be virtually independent for signal levels at times separated by 20 ms. Hence, 20 ms is taken as the minimum interleaving depth for randomization of multipath interference.

Theoretical expressions of average detection performances for Ricean fading may be obtained in References 19 through 23. Figure 7 depicts the detection performance DPSK for a range of Rice factors and a range of symbol correlation coefficients.

**FEC coding**

At the low data rate for aeronautical communications, the modulation bandwidth is considerably smaller than the frequency uncertainty of the carrier location. Thus, the required bandwidth allocation per channel will not be significantly increased by the higher modulation symbol rate required to accommodate the redundancy for FEC coding. FEC codes of rate  $r = 0.5$  can be more powerful and simpler to decode than codes of higher rates. For this reason, such a code rate is desirable in this application.

After investigating candidate FEC codes, including block [24] and convolutional codes, as well as methods of practically implementing decoding

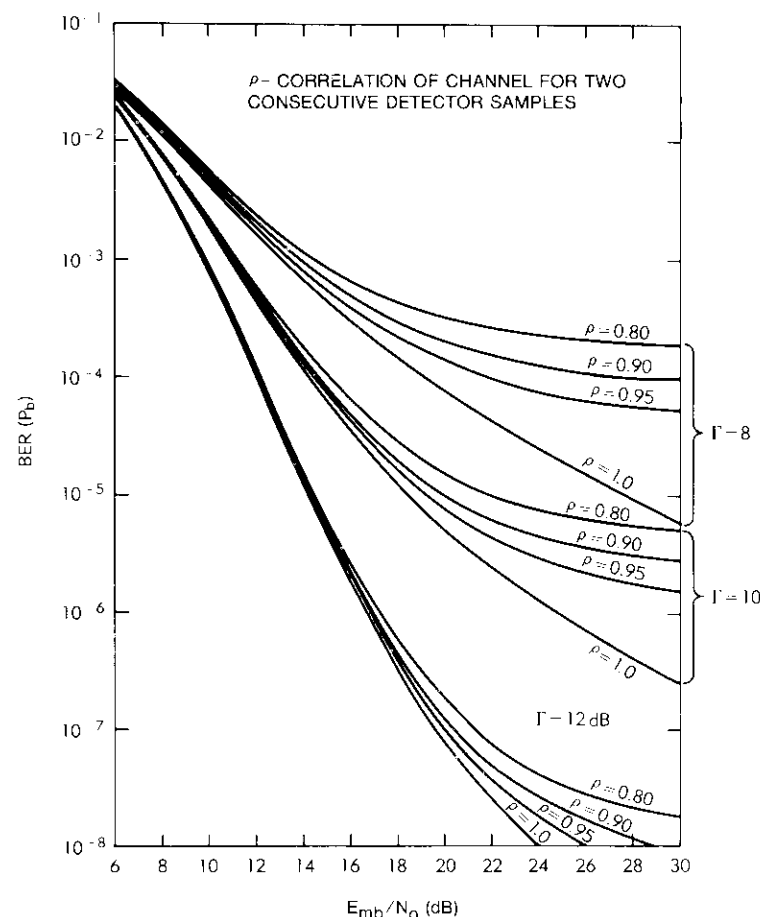


Figure 7. Ideal DPSK Detection Performance for Ricean Channel With Rice Factor of  $\Gamma = 10 \log \gamma$

schemes [25]–[27], it was concluded that because of the large coding gain, a convolutional code with soft detection and Viterbi decoding is the preferred scheme for this application.

Viterbi decoding [28],[29] of soft-detected code symbols is easy and reasonably cheap to implement at the data rates assumed for the system. A minimum free Hamming distance of  $d_f = 10$  can be obtained from a binary convolutional FEC code with a code rate of  $r = 0.5$  and a memory of  $\gamma = 6$  bits. Figure 8 illustrates the encoder used to produce the recommended convolutional FEC code. For this code, with constraint length  $K = \gamma + 1 = 7$ , a Viterbi decoder with  $S = 2 \gamma = 64$  code states is required. Together

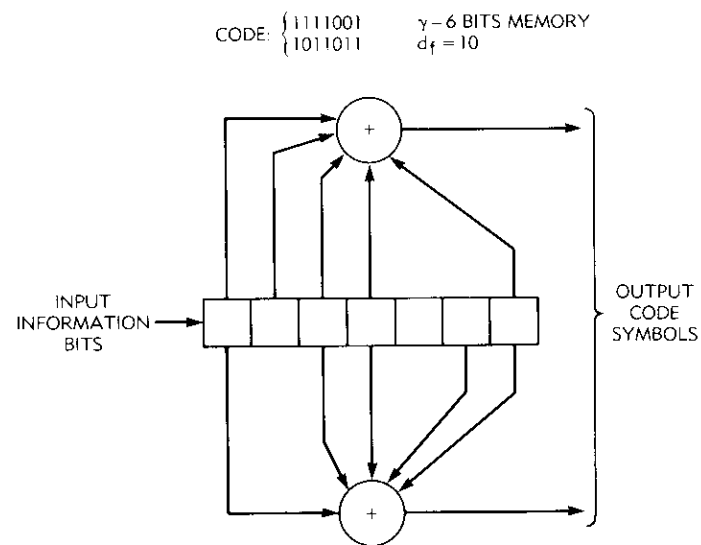


Figure 8. Recommended FEC Code

with 8-level soft detection of PSK, Viterbi decoding can achieve  $P_b = 10^{-5}$  with an  $E_b/N_o$  of about 4.4 dB for the AWGN channel [30]. Thus, the potential coding gain is greater than 5 dB at  $P_b = 10^{-5}$ .

#### Combined modulation and coding

The combination of modulation and coding, including the use of interleaving, must be considered in communications performance. Because multipath interference is the primary source of performance loss, interleaving is of great importance in making performance assessments.

There are two areas of concern in interleaving: the row length  $L$  and the column width  $W$ . Modulator output is interleaved after FEC encoding by storing the encoder output in rows and reading the stored symbols into the modulator by columns. On the receiving end, the output of the demodulator is read out by columns and then deinterleaved by reading the stored symbols into the Viterbi decoder by rows. The overall dimensions,  $L \times W$ , of the interleaving matrix should be equal to both the total message length for the outbound TDM frames and the message length for the inbound TDMA bursts.

With interleaving, the deinterleaved input to the decoder will appear to have independent fading of successive symbols over two or more constraint lengths of the code. Since input to the decoder comes from rows, the arrival time of adjacent symbols in each row should be separated by at least the

decorrelation interval of 20 ms. Hence, column size should be the number of modulation symbols corresponding to a 20-ms transmission interval. With an FEC coding of rate  $r = 0.5$ , the symbol rate  $R_s$  is  $2R_b$ , where  $R_b$  is the information bit rate. Therefore,  $W = 20 \text{ ms} \times 2R_b$  is desired. Most paths of near minimum distance re-merge with the desired code sequence within two constraint lengths of the code. For the code of interest,  $K = 7$  information bits, corresponding to 14 code symbols. It follows that the row length should be at least 28 symbols, or  $L \geq 28$ . In this case, the length chosen was  $L \geq 32$ .

As an indication of interleaving matrix size, consider the case of  $R_b = 200$  bit/s or  $R_s = 400$  symbol/s. In this case,  $W$  is greater than or equal to 8 symbols. If  $R_b = 400$  bit/s or  $R_s = 800$  symbol/s,  $W$  is greater than or equal to 16 symbols. The row length  $L$  can be any integer value at least equal to 32. Thus, the minimum allowable burst length for TDMA or frame length for TDM is 256 symbols or 128 information bits for  $R_b = 200$  bit/s, and 512 symbols or 256 information bits for  $R_b = 400$  bit/s. For information bits per burst or frame, the allowable number is  $128 + 4I$  for  $R_b = 200$  bit/s and  $256 + 8I$  for  $R_b = 400$  bit/s, where  $I$  is any non-negative integer.

Multipath interference affects modulation performance by increasing the required  $E_b/N_o$  to obtain a given channel error probability  $p$ . Interleaving is used to randomize the effect of this interference on FEC decoding. For the code of interest,  $d_f = 10$ , which means that any two code sequences must differ in at least 10 symbol locations. After deinterleaving is performed, the multipath interference for these 10 symbols should be independent and appear equivalent to AWGN.

A summary of estimated performances for the three modulations, coded and uncoded, is given in Table 5 for the aeronautical satellite channel discussed previously. PSK performance is listed only for the case of  $R_b = 800$  bit/s because the dynamics of the channel and phase noise might not allow reliable coherent detection at lower signaling rates.

The use of coherent detection would allow coded PSK to be quite efficient in power utilization if the signaling rate is sufficiently high, as shown in Table 5. At  $R_b = 800$  bit/s or higher, coherent detection may be feasible. However, the actual rate at which coded PSK is usable would have to be determined by experiments. Without knowing what range of  $R_b$  will allow good coded PSK performance, coded DPSK communications would be a feasible choice because at the  $R_b$  values of interest, coded DPSK would perform considerably better than coded FSK. Only at very low rates (50 bit/s or less) would the use of DPSK be questionable, and only then might FSK perform better than DPSK. At the  $R_b$  values of most interest (200 and 400 bit/s), coded DPSK is the recommended signaling method.

TABLE 5. ESTIMATED PERFORMANCES AT  $P_b = 10^{-5}$  FOR THE RICEAN AERONAUTICAL SATELLITE CHANNEL ( $\Gamma = 10$  dB;  $B_f = 100$  Hz)

MODULATION	ASSUMED IMPLEMENTATION LOSS (dB)	INFORMATION BIT RATE $R_b$ (bit/s)	REQUIRED $E_b/N_o$ (dB)		CODED GAIN (dB)	DECODING LOSS FROM MULTIPATH INTERFERENCE (dB)
			UNCODED	CODED		
PSK	2.6	200	—	—	—	—
		400	—	—	—	—
		800	21.6	8.2	13.4	1.2
DPSK	1.6	200	*	9.3	*	1.0
		400	26.0	9.1	16.9	0.8
		800	20.7	8.9	11.8	0.6
FSK	1.2	200	22.6	11.5	11.1	0.6
		400	22.6	11.5	11.1	0.6
		800	22.6	11.5	11.1	0.6

\* Dynamic multipath interference does not allow  $P_b = 10^{-5}$  to be obtained from uncoded DPSK.

For the chosen case of coded DPSK, Table 6 gives an estimate of the required  $C/N_o$  for the direct path, parametric in different Rice factors and different transmission rates.

TABLE 6. REQUIRED  $C/N_o$  vs INFORMATION BIT RATE FOR CODED DPSK

INFORMATION BIT RATE, $R_b$ (bit/s)	REQUIRED $C/N_o$ (dB-Hz) FOR DIFFERENT RICE FACTORS $\Gamma$ (dB)*					
	8	9	10	12	14	16
100	31.4	30.5	29.9	29.2	28.7	28.4
200	33.2	32.7	32.3	32.0	31.8	31.6
400	35.7	35.4	35.1	34.9	34.8	34.7
800	38.3	38.1	37.9	37.7	37.5	37.4

\* Convolutional FEC Coding: Rate 0.5, distance 10. Interleaving, soft detection, Viterbi decoding. Assumed implementation loss of 1.6 dB.

**Acquisition and synchronization**

Signal acquisition and tracking are two important factors that affect overall system performance. Fast signal acquisition is of major concern on the return link where traffic is bursty and long acquisition times are undesirable because

of a large signaling overhead that reduces system throughput. On the forward link, where continuous carriers are used, signal acquisition time is less consequential.

Because it is usually more difficult to achieve reliable signal tracking for the more efficient modulations, tracking a PSK signal is more difficult than tracking a DPSK signal. In addition, synchronizer tracking performance can be influenced by channel dynamics, phase noise, and fading.

**Channel dynamics**

Channel dynamics include static frequency offsets resulting from translation errors in the aircraft, and time-varying effects caused by aircraft motion and satellite inclination. Translation errors in the shore station and the satellite are removed by an automatic frequency control (AFC) loop in the coast earth station [31]. The static and slowly varying frequency errors are listed in Table 7. Aircraft acceleration values are given in Table 8, with the resulting Doppler rate at 1.5 GHz.

TABLE 7. FREQUENCY ERRORS

SOURCE	SHORE TO AIRCRAFT (Hz)	AIRCRAFT TO SHORE (Hz)	COMPENSATION BY AFC
Satellite translation	48,830	25,565	Yes
Shore station up- and down-converters	960	630	Yes
Shore satellite Doppler from orbit inclination (5°)	640	420	Yes
Aircraft motion Doppler (300 m/s)	1,500	1,600	No
Aircraft/satellite Doppler from orbit inclination (5°)	205	209	No
Aircraft down- and up-converters*	240	250	No

\* Assumed aging rate is  $1.5 \times 10^{-7}$ .

TABLE 8. AIRCRAFT ACCELERATION VALUES

SITUATION	MAXIMUM ACCELERATION (10 m/s <sup>2</sup> )	RESULTING DOPPLER RATE* (Hz/s)
Level flight	0.2	10
Clear air turbulence	1.5 to 2.0	75 to 100

\* At 1.5 GHz.

The Doppler and acceleration values that have been assumed in this study are as follows:

$$\begin{aligned} \text{Maximum Doppler} &= \pm 2,000 \text{ Hz and } \pm 12,567 \text{ rad/s} \\ \text{Doppler rate} &= \pm 100 \text{ Hz/s and } \pm 628 \text{ rad/s}^2. \end{aligned}$$

Channel dynamics of the magnitude described here can only be handled by a second-order tracking loop. To keep steady-state tracking errors at acceptable levels, it was found that the minimum one-sided, low-pass bandwidth of the synchronizer must be larger than 35 Hz.

#### Influence of phase noise and AWGN

The effect of phase noise on synchronizer tracking performance is evaluated here by linear filter theory. The phase noise is specified by its spectral density  $S_{\phi}(f)$ , which is assumed to be of the form

$$S_{\phi}(f) = \frac{a_2}{f^2} + \frac{a_3}{f^3} \quad f > 0 \quad (1)$$

Two cases of phase noise for  $a_2$  and  $a_3$  are assumed here. Case 1 corresponds to the receive phase-noise specifications given in the original MARISAT specifications [31] and represents a worst case:  $a_2 = 4 \times 10^{-2}$ ;  $a_3 = 4$ . Case 2 represents a typical case:  $a_2 = 4 \times 10^{-3}$ ;  $a_3 = 0.4$ . Recent developments in oscillator technology have demonstrated that a 10-dB improvement can be expected for case 1. For this reason, case 2 has been included here as the more typical specifications.

The synchronizer tracking variance resulting from phase noise and AWGN can be written as

$$\sigma^2 = \frac{8.71 a_3}{B_n^2} + \frac{B_n}{C/N_o}$$

where  $B_n$  is the one-sided, low-pass synchronizer bandwidth and  $C/N_o$  is the available carrier power-to-AWGN spectral density ratio.

#### Tracking performance in Ricean fading

The tracking performance of the carrier synchronizer in a fading environment was analyzed during this study. The resulting expression for tracking variance resulting from a Ricean fading process is given by

$$\sigma_f^2 = \frac{1}{2\gamma(1 + B_n/B_f)}$$

where  $\gamma$  is the Rice factor,  $B_n$  is the synchronizer noise bandwidth, and  $B_f$  is the one-sided fading bandwidth. The above formula is accurate for reasonably large Rice factors  $\gamma$ , say  $\gamma = 4$ . The total tracking variance, then, including AWGN phase noise and Ricean fading effects, is

$$\sigma^2 = \frac{B_n}{C/N_o} + \frac{8.71 a_3}{B_n^2} + \frac{1}{2\gamma(1 + B_n/B_f)}$$

The cycle slip rate of a synchronizer is approximated by the cycle slip rate of a phase-locked loop (PLL) [32],[33] with 6 dB less  $C/N$  in the loop because the carrier synchronizer is effectively tracking twice the phase error of the equivalent PLL because of modulation removal.

#### Effect of cycle slips on DPSK performance

The effect of synchronizer cycle slips on the overall link performance can be approximated for DPSK modulation if perfect interleaving is assumed. A synchronizer cycle slip creates an effect that is very similar to a deep fade. It results in an error burst with a symbol error rate of approximately  $1/2$ , which increases the average symbol error rate.

By examining the simulation results given in Reference 34, it can be concluded that the average symbol error rate resulting from the synchronizer cycle slips,  $P_{cs}$ , is

$$P_{cs} = \frac{1}{2B_n \cdot \bar{T}_{slip}} \quad (2)$$

The effect of cycle slips on overall performance is negligible if  $P_{cs}$  is much smaller than the symbol error rate because of additive noise,  $P_s$ . By combining the above relationships, the cycle-slip-induced symbol error may be given, as shown in Table 9.

TABLE 9. CYCLE SLIP-INDUCED SYMBOL ERROR RATE IN CASE OF FAST FADING

$R_b$ (bit/s)	CASE 1: WORST CASE		CASE 2: TYPICAL CASE	
	$B_n$	$P_{cs}$	$B_n$	$P_{cs}$
100	41	$6.6 \times 10^{-3}$	100	$1.8 \times 10^{-3}$
200	52	$1.4 \times 10^{-3}$	200	$1.9 \times 10^{-4}$
400	66	$1.0 \times 10^{-4}$	400	$4.8 \times 10^{-5}$

**Summary of tracking performance**

The results show that the expected tracking variance in the range of 4 to  $9 \times 10^{-2} \text{ rad}^2$  is accurate enough for BPSK modulation. Of more concern is the mean time between cycle slips, which can be from about 200 to several tens of thousands of bits, depending on assumed phase noise and the data rate. Cycle-slipping behavior should not be judged on the average number of bits between slips but rather on the way that it affects the DPSK symbol error rate after the deinterleaver. The results shown here indicate that the cycle-slipping rate may have a noticeable effect on overall system performance in the case of a 100-bit/s data link. Minimal degradations can be expected in 200- and 400-bit/s data links.

**Signal acquisition**

Signal acquisition is a particularly important issue for the coast earth station for two reasons: the return link is bursty, and each burst must be acquired separately.

The acquisition method assumed here is based on the use of spectral estimation to locate the signal in the large uncertainty band, followed by a phase-locked loop for tracking purposes.

Figure 9 shows the required signal processing that takes place in the earth station. First, the incoming signal is mixed down to baseband by the local oscillator. This signal is then sampled and digitized over a time interval  $\tau_s$ . After  $\tau_s$  seconds of signal samples have been accumulated, a fast Fourier transform (FFT) is performed. If a signal was present, it will show up as a peak in the spectrum thus generated. (The position of the peak is proportional to the frequency offset between the signal and the local oscillator.) Next, the estimator picks out the most likely offset frequency and adjusts the local oscillator accordingly. Finally, a phase-locked loop is activated to resolve the remaining small frequency uncertainty and to track the signal in the presence of channel disturbances.

Assuming a 10-ms, 3-dB decorrelation time with false alarm and miss probability values of  $10^{-2}$ , the required coarse frequency acquisition preamble lengths of 7, 10, and 16 bits have been computed for data rates of 100, 200, and 400 bit/s, respectively. These results indicate that if the fade decorrelation time is reduced, the miss probabilities are greatly reduced.

Assuming Ricean fading with a 10-dB Rice factor and using the results given in Reference 35, phase acquisition times have also been computed. Table 10 shows the computed results in terms of bit rate, assuming optimal tracking bandwidths.

These results show that the required preamble lengths for fine frequency acquisition are reasonably short for the two lowest data rates of 100 and

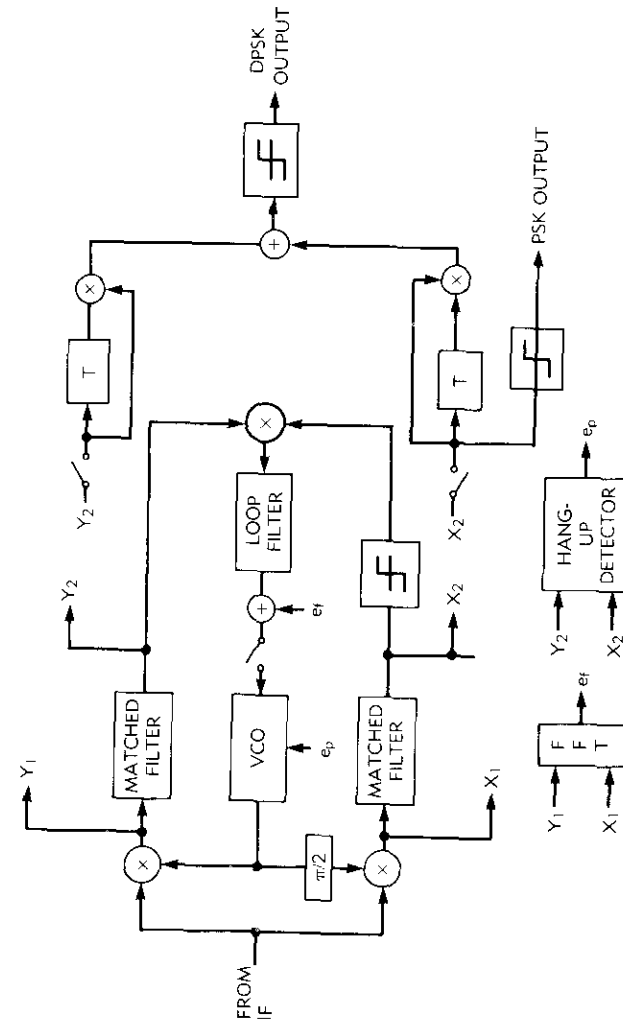


Figure 9. Signal Acquisition Processing With FFT

TABLE 10. REQUIRED PHASE ACQUISITION TIMES FOR OPTIMAL TRACKING BANDWIDTHS

$R_b$	$B_L$	NO. OF BITS FOR PHASE ACQUISITION
100	35	6
	41	5
200	52	8
	35	12
400	66	12
	35	23

200 bit/s. However, the preamble requirement is too large for the 400-bit/s link in connection with the 35-Hz bandwidth. This problem can be resolved by widening the synchronizer bandwidth during acquisition.

#### Signal acquisition in the mobile terminal

Signal acquisition in the mobile terminal is eased because the aircraft receiver must acquire a continuous TDM signal, but it is also complicated by the presence of modulation on the carrier. Three candidate acquisition methods are available for this case: synchronizer sweep acquisition, synchronizer with frequency feedback aiding, and methods based on spectral estimation techniques. After investigating these techniques during the study, it was concluded that the most preferable one is the frequency-feedback-assisted synchronization. Symbol timing, Doppler compensation, and pilot-tone-aided synchronization techniques were also investigated: one conclusion reached was that separate pilot tones would not be required for this system.

#### Network configuration and control

In the development of an aeronautical data communications system, the detailed network design and operational protocols will evolve through a cooperative effort among the various organizations participating in the design and operation of the system. However, to illustrate the way in which a network could be configured and also to analyze its performance, the sample design summarized here was assumed in this study.

The function of the aeronautical satellite data network is to provide duplex communications for ATC, company communications between aircraft in the North Atlantic region, and one or more ground earth stations. The aeronautical satellite data network is controlled by two network control centers (NCC), one on each side of the Atlantic. Together, one NCC controls the network;

the other serves as a backup. Each NCC is directly linked to an ATC center, which may be colocated with the network control center.

The object of the network is to provide a low message delay and a very low probability of undetected message error both for company communications and ATC messages. The choice of link protocol for company communications will be decided by the company and will depend on the particular sending and receiving data transmission equipment (DTE) used.

#### Characteristics of ATC messages

To satisfy the service requirements (summarized previously), each ATC message consists of an ID, which is a local network address assigned to the plane upon entry into the network, and a message code that specifies the message type. Since the number of planes in the North Atlantic peaks at between 210 and 230, a 10-bit ID is used. The message code uses 8 bits, which allows up to 256 different message types for ATC.

By using the results of Reference 3, all messages on the forward link are 37 bits or less, except for the reroute clearance message at 266 bits, and the meteorological advisory, miscellaneous advisory, emergency advisory, and emergency deviation request, all at 1,218 bits. The routine position-request messages and emergency messages have a time-to-send-and-receive delay requirement of 15 s. Other routine messages have a delay requirement of 1 min.

The most frequent return link message is a position report, which is 76 bits for a routine report, and up to 121 bits for a special report. The emergency message (from plane to ground) is 18 bits and should be received by the ground station within 15 s of the first channel access. All other messages from plane to ground are less than 76 bits, except for two message types that use 266 bits, as well as miscellaneous word messages, specified as 2,418 bits.

#### Network access

With one coast earth station on each side of the Atlantic Ocean, the network uses 1 TDM forward link and 10 distinct return links. The TDM forward-link data rate is 200 bit/s. A sketch of this link frame is shown in Figure 10. The frame consists of two fixed fields, one for company communications and one for ATC messages and address messages for company communications. The company communications portion of the frame is divided into fixed slots, with each call occupying one slot. The ATC messages and address messages are consecutively inserted into the ATC message portion of the frame.

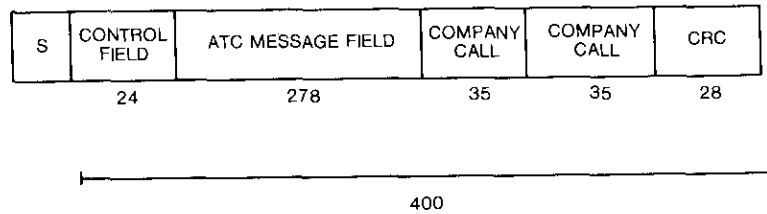


Figure 10. Sketch of TDM Frame Format

The total return-link data rate requirement for ATC messages is about 800 bit/s; therefore, conservatively, 6 separate channels of 200 bit/s each are used for return-link ATC messages. Lowering the return-link data rate from 800 to 200 bit/s lowers the required e.i.r.p. at the plane by a factor of 4, and for a given depth of bit interleaving on the return link, improves the interleaving efficiency by a factor of 4. Ten return-link carriers have been assumed for the baseline system. In addition to the six channels used for ATC messages, two are used for company communications calls, one is used for ATC emergency messages, and the remaining channel is used for aircraft requests for ATC network entry (which takes place after entering North Atlantic air space), ATC polling requests, and requests for company communications calls.

#### ATC network protocol

The ATC link between the ATC center and an individual airplane is controlled by the ATC center, which serves as the master station. To send a message to the plane, the master station first transmits the plane ID, message type, and 4 bits that specify the return transmit frequency; the message itself is then transmitted. However, when the master station simply needs a position report, the message type specifies the position report message, leaving the message field blank. To send a message to the ground, the plane sends a poll request (which includes the message type) on the access channel. On receiving the poll request, the ATC center polls the plane for the message type requested.

A link protocol is used to ensure that all transmitted messages are received without detected errors. Messages originated by either the ground station or the plane on the random access channel have a cyclic redundancy check (CRC). The receiver calculates the CRC checksum, and if an error is detected, discards the message. If the message has no detected error, the receiver transmits a message acknowledgment. If the transmitter receives no acknowledgment, the message is retransmitted until acknowledged. Using this link control technique, messages are transmitted until they are received without detected errors. In the TDM forward link, the CRC checksum is not attached

to each message; instead, one CRC checksum is used in each frame to check all messages in that frame. The ground station transmits acknowledgments with the control field portion of the TDM frame.

The NCC station establishes a polling sequence, with messages ordered by priority. When polled, the aircraft transmits the requested message or message acknowledgment at a fixed time,  $T$ , after receiving the poll;  $T$  is the same for all stations and may be about 0.2 s, which includes the signal processing required to form the return burst. Since the NCC station knows the length of the returning message, polling times can be scheduled so that time between bursts on the return channel is minimized.

#### Setup of company communications call

To initiate a company communications call, the plane or ground party sends a call request to the NCC by using the ALOHA request channel. Depending on whether there is an unused company communications channel, the NCC sends a positive or negative acknowledgment to the plane. A positive acknowledgment contains the return channel frequency for the call. Because message-type numbers 253, 254, and 255 (*i.e.*, specific combinations of 8-bit words) are used for these requests and acknowledgments, they are not used for ATC messages.

#### Forward link

The frame format of the forward TDM link is shown in Figure 10. ATC messages are inserted into the ATC field consecutively, with a portion of the control field giving the receiver information about the starting position of each message in the frame. The CRC checksum is formed on the control field, ATC message field, and company communications field. If the CRC checksum indicates an error, all ATC messages and message portions are discarded, and no message acknowledgments are transmitted.

The format of the control field is shown in Figure 11. The first bit is used for control in case of L-band interferences; the next 10 bits are used for control of the frame format; and the last 13 bits are used for control of the access channel. To avoid L-band interference, the L-band TDM carrier may be transmitted on one of several frequencies. The function of the first bit in the control channel is to inform all aircraft that the TDM frequency is being changed.

Emergency messages from ground to plane are 1,213 bits long and have delay requirements of 15 s. To help ensure that the emergency message is correctly received within the 15-s delay requirement, the entire frame is used to transmit the message, and the emergency message is transmitted continuously until an acknowledgment reply is received from the plane.

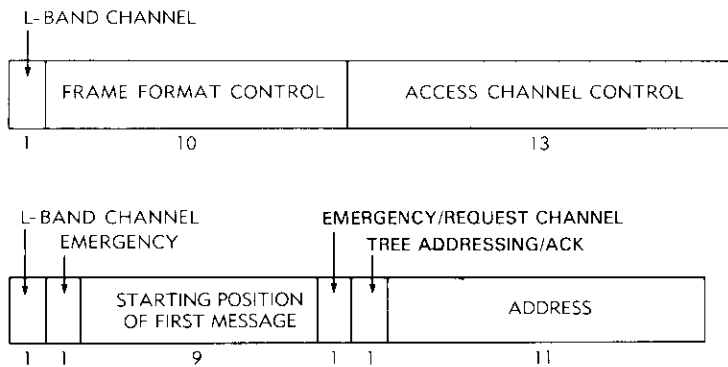


Figure 11. ATC Control Field Format

Access channels use the unslotted ALOHA protocol, which consists of the following procedure. An aircraft transmits a message and waits for an acknowledgment from the ground station; if no acknowledgment is received, it transmits again, at random, during a specified time interval. Acknowledgments are sent via the access channel control field. Without an access control mechanism, the ALOHA channel is certain to become congested and thereafter unusable. In the network considered here, the NCC monitors the request channels, and when congestion occurs, a tree-addressing scheme, similar in principle to that of Capetanakis [36], is used to clear the channel.

The error detection code used is a (512,484) Bose-Chaudhuri-Hocquenghem code, shortened to (400,372) to accommodate the 400-bit frame size. Results of error rate calculations show that for the forward link, the undetected BER is low enough so that air traffic safety is not affected, even when extremely noisy and bursty channels are assumed. Similar calculations for the return link give a comparably undetected bit error rate.

**Return link**

To communicate with the ground station, the plane transmits a burst on the appropriate return-link channel. The burst format for ATC messages is shown in Figure 12. Table 11 shows the most frequent messages assumed for the return link. The error detection code is the same as that used on the forward link.



Figure 12. Return Burst Format for ATC Message

TABLE 11. LENGTH OF FREQUENT RETURN BURSTS

MESSAGE	NUMBER OF INFORMATION BITS IN MESSAGE	NUMBER OF CHANNEL BITS IN ENCODED MESSAGE (INCLUDING CRC AND TAIL)	TRAFFIC INTENSITY
Request	18	104	~0 bit/s
Position Report	76	220	53 bit/s (5 min./poll)
Special Position Report 1	121	310	
Special Position Report 2	103	274	242 bit/s (0.5 min./poll)
Special Position Report 3	90	248	

**Network capacity**

Return-link ATC message bursts consist of an integral number of 324-bit channel blocks. Traffic projections in Reference 3 suggest that 189 return bursts per minute will use one 324-bit channel block; 1 return burst per minute will use two 324-bit channel blocks; and 0.5 return bursts per minute will use eight 324-bit channel blocks. Collectively, these require a channel information bit rate capacity of 526.5 bit/s. Since the designed capacity of the return link is 1,200 bit/s (i.e., six 200 bit/s carriers), the network has a safe margin to support the return-link traffic, even with overhead added for synchronization and guard times.

Forward-link ATC messages have a data rate of 101.6 bit/s, including overhead. Assuming 40 channel bits were used for the synchronization word at the start of each frame, the forward-link capacity available for ATC messages is 132.4 bit/s, which is sufficient to handle the forward-link ATC message traffic.

The capacity of the company communications call network is two simultaneous calls, each at 16.7 bit/s on the forward link and 200 bit/s on the return link. This capacity can be increased by adding carriers, as discussed below.

**Message delay and throughput**

Message delay and throughput are determined by the number of retransmissions required for each message. Since the maximum message length is about 1,000 bit/s, and since the channel BER is  $10^{-5}$ , about 1 percent of the messages must be retransmitted because of an error in the received message. Assuming the message loss resulting from synchronization loss is 1 percent, the average number of retransmissions required for each message has negligible

effect on message delay and throughput. Detailed calculations of message delay and throughput were performed to show that both emergency and non-emergency messages could be conveyed within the permissible delay times.

### **System growth alternatives**

One feature of the sample system configuration described here is that it can accommodate growth that results from increased capacity and from company communications calls originating from multiple earth stations. Increasing network capacity is easily accomplished by adding additional carriers instead of increasing the transmission rate of carriers already in the system. The former method is preferred because each carrier uses a very small additional bandwidth, whereas increasing the transmission rate both raises the required e.i.r.p. and lowers protection against fading for a given depth of symbol interleaving.

Additional earth stations may be added to the network to accommodate company or public calls provided that there is a signaling channel between the NCC and earth station that can relay information about call-channel assignment from aircraft to earth station.

A system with multiple carriers on the forward link would not require multiple receivers on the aircraft because the aeronautical control center (ACC) could switch ATC messages for planes engaged in company communications calls to the appropriate company communications call channel.

### **Avionics considerations**

One guideline adopted to help define the recommended system is that aircraft avionics be as inexpensive as possible in terms of procurement, installation, and operating costs. The major variables in this system that influence avionics costs are the aircraft antenna and the size of the aircraft's RF power amplifier.

As discussed above, to minimize costs, a low-gain requirement has been adopted (0 dBi above 10° elevation angle for 90 percent of azimuth) for the aircraft antenna, and a microstrip patch implementation is favored because of low installation costs and minimum drag.

Important considerations in limiting the size of the aircraft's power amplifier are as follows:

- a. amplifier expense (if overly large powers are required, special amplifiers must be developed);
- b. amplifier heat dissipation;
- c. DC power requirements; and
- d. physical size.

In the recommended system, data transmission rates and the selected modulation, coding, and interleaving scheme result in aircraft RF power requirements that are significantly lower than those required in the AEROSAT system design; for this reason, the selection of aircraft RF amplifiers for this system should be fairly straightforward. Also, with these lower power requirements, problems associated with packaging, installation, prime power requirements, and heat dissipation should be significantly less than those encountered in the AEROSAT program.

Implementation of the receiver system, which keeps losses at or below the values assumed in Table 1 [*i.e.*, 1.3-dB low-noise amplifier (LNA) noise figure], should not be difficult unless a cable run greater than the assumed 25 ft from antenna to LNA is required. For LNAs that require further effort in a detailed system design phase, other considerations are cost/noise figure tradeoffs and the selection of a location that meets the requirements for both proximity to antenna(s) and accessibility for maintenance.

The specification and design of interfaces with aircraft input/output terminal devices require further system definition as well as close cooperation with the airline industry and aircraft manufacturers. These interfaces include:

a. *A data management system.* This system would control, buffer, format, and process all I/O data. A data management system would be equipped with a microprocessor that could be operated independent of the microprocessor used for communications purposes. Possible functions and interfaces that could be provided by the data management system are as follows:

- airborne navigation systems
- aircraft performance monitoring systems
- flight display unit data
- flight data recorders
- system self-testing.

b. *Display and operator input devices.* An aeronautical data ATC and communications system must be designed to achieve maximum simplicity and ease of operation. Components of these devices will probably include a keyboard (which may be shared with other aircraft avionics systems, and which may require special-purpose keys), an alphanumeric display device and status display devices, and a hard-copy printer. The recommended system uses computer-controlled operating protocols, thus minimizing the work required of the cockpit crew for system operation.

## Conclusions

Two important variables in design alternatives for an aeronautical communications satellite data-link system are aircraft antenna performance and signal design because both can be used to combat multipath fading. The approach taken in this study is to minimize aircraft antenna complexity and to use a combination of interleaved rate  $\frac{1}{2}$  FEC to combat multipath fading. The recommended system is technically feasible, will operate reliably, and will be relatively inexpensive. Aircraft terminals will not have a large effect on the aircraft's exterior, power system, or cooling system, and they will be relatively simple to install. Acquisition and synchronization can be reliably achieved without a separate pilot-tone carrier for the satellite.

The aircraft antenna design selected here uses microstrip patch elements; it was chosen for ease of installation and its very low profile. A simple, top-mounted array consisting of three or four elements is recommended.

Microprocessor technology will permit low-cost implementation of the recommended modulation, coding, interleaving, and network control functions on the aircraft terminals. Similarly, digital processors will permit rapid acquisition of return-link TDMA burst signals at ground stations. Because system operation is automatic, additional work for the cockpit crew is minimized.

## Acknowledgments

The authors would like to thank David Lipke for his support and technical guidance during this study. Also, discussions with Leslie Klein have been very helpful.

## References

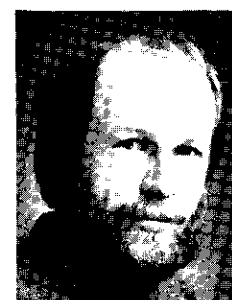
- [1] D. Lipke, "A New Possibility for Aeronautical Satellite Communications," Globecom 1982 Conference, Miami, Florida, November 1982, *Proceedings*, Vol. 3, pp. E5.2.1-E5.2.4.
- [2] D. Lipke, "Use of INMARSAT Facilities for Aeronautical Satellite Communications," Third International Conference on Satellite Systems for Mobile Communications and Navigation, London, England, June 1983, *Proceedings*, IEE Pub. 222, pp. 212-215.
- [3] SRI International, "Ocean Area System Improvement Study," Menlo Park, California, April 1981.
- [4] "Air Traffic Control Experimentation and Evaluation With NASA ATS-6 Satellite," Volumes I-VII, FAA Report No. FAD-RD-75-173, September 1976.
- [5] R. W. Sutton et al., "Satellite Aircraft Multipath and Ranging Experiment Results at L-Band," *IEEE Transactions on Communications*, Vol. COM-21, No. 5, May 1973, pp. 639-647.
- [6] P. Bello et al., "Impact on Satellite Aeronautical Channel on Modem Specifications, Phase II," Oceanic Multipath Measurements and Modem Concepts, FAA Report No. FAD-RD-74-215, January 1975.
- [7] P. Bello, "Aeronautical Channel Characterization," *IEEE Transactions on Communications*, Vol. COM-21, No. 5, May 1973, pp. 548-563.
- [8] P. D. Engels, "A Channel Simulator for L-Band Satellite Mobile Communications," *AGARD Conference Proceedings*, No. 239, pp. 23-1-23-9.
- [9] L. A. Frasco and H. D. Goldfein, "Signal Design for Aeronautical Channels," *IEEE Transactions on Communications*, Vol. COM-21, No. 5, May 1973, pp. 534-547.
- [10] I. Katz, "Radar Reflectivity of the Ocean Surface for Circular Polarization," *IEEE Transactions on Antennas and Propagation*, July 1963, pp. 451-453.
- [11] S. Durrani and H. Staras, "Multipath Problems in Communications Between Low-Altitude Spacecraft and Stationary Satellites," *RCA Review*, March 1968, pp. 77-105.
- [12] "Engineering and Development Program Plan-Aeronautical Satellites (AEROSAT)," FAA Report No. FAA-ED-17-2, September 1974.
- [13] Canadian Marconi Company, "Airborne L-Band Phased Array, Data Sheets," *Product Catalog*, Montreal, Canada, 1975.
- [14] Transco Products, Inc., "Microwave Antennas," *Product Catalog*, Catalog No. 80, Venice, California, 1981.
- [15] American Electronic Laboratories, Inc., "Antennas," *Product Catalog*, Lansdale, Pennsylvania, 1982.
- [16] E. J. Wilkinson, "A Circularly Polarized Slot Antenna," *The Microwave Journal*, March 1961, pp. 97-100.
- [17] Ball Aerospace Systems Division, "Ball Microstrip Antenna Data Sheets," *Product Catalog*, Boulder, Colorado, 1983.
- [18] I. J. Bahl and P. Bhartia, *Microstrip Antennas*, Dedham, Massachusetts: Artech House, 1980.
- [19] W. C. Lindsey, "Error Probabilities for Rician Fading Multichannel Reception of Binary and N-ary Signals," *IEEE Transactions on Information Theory*, October 1964, pp. 339-350.
- [20] W. C. Lindsey, "Error Probabilities for Coherent Receivers in Specular and Random Channels," Correspondence in *IEEE Transactions on Information Theory*, January 1965, pp. 147-150.
- [21] J. J. Jones, "Multichannel FSK and DPSK Reception With Three-Component Multipath," *IEEE Transactions on Communications Technology*, Vol. COM-16, No. 6, December 1968, pp. 808-821.
- [22] W. C. Lindsey, "Error Probabilities for Partially Coherent Diversity Reception," *IEEE Transactions on Communications Technology*, Vol. COM-14, No. 5, October 1966, pp. 620-625.

- [23] D. Chase, "Digital Signal Design Concepts for a Time-Varying Rician Channel," *IEEE Transactions on Communications*, Vol. COM-24, No. 2, February 1976, pp. 164-172.
- [24] Shu Lin, *An Introduction to Error-Correcting Codes*, Englewood Cliffs, New Jersey: Prentice Hall, 1970, pp. 101-106.
- [25] D. Chase, "A Class of Algorithms for Decoding Block Codes With Channel Measurement Information," *IEEE Transactions on Information Theory*, Vol. IT-18, No. 1, January 1972, pp. 170-181.
- [26] E. J. Weldon, "Decoding Binary Block Codes on Q-ary Output Channels," *IEEE Transactions on Information Theory*, Vol. IT-17, No. 4, pp. 713-718.
- [27] L. Lee and M. Weng, "2-Bit Soft-Decision Weighted Erasure Decoding for Binary Block Codes," *COMSAT Technical Review*, Vol. 10, No. 2, Fall 1980, pp. 397-415.
- [28] A. J. Viterbi, "Error Bounds for Convolutional Codes and an Asymptotically Optimum Decoding Algorithm," *IEEE Transactions on Information Theory*, Vol. IT-13, April 1967, pp. 260-269.
- [29] J. A. Heller and I. M. Jacobs, "Viterbi Decoding for Satellite and Space Communications," *IEEE Transactions on Communications Technology*, Vol. COM-19, No. 5, Part II of Two Parts, October 1971, pp. 835-848.
- [30] G. C. Clark, Jr. and J. B. Cain, *Error-Correction Coding for Digital Communications*, New York: Plenum Press, 1981, pp. 227-266.
- [31] D. W. Lipke et al., "MARISAT—A Maritime Satellite Communications System," *COMSAT Technical Review*, Vol. 7, No. 2, Fall 1977, pp. 351-391.
- [32] F. Gardner, "Phase-Lock Techniques," 2nd Edition, New York: John Wiley, 1979.
- [33] J. K. Holmes, *Coherent Spread Spectrum Systems*, New York: John Wiley, 1982.
- [34] G. Ascheid and H. Meyr, "Cycle Slips in Phase-Locked Loops: A Tutorial Survey," *IEEE Transactions on Communications*, Vol. COM-30, No. 10, October 82, pp. 2228-2241.
- [35] H. Meyr and L. Popken, "Phase Acquisition Statistics for Phase Locked Loops," *IEEE Transactions on Communications*, Vol. COM-28, No. 8, August 1980, pp. 1365-1372.
- [36] J. Capetanakis, "Tree Algorithms for Packet Broadcast Channels," *IEEE Transactions on Information Theory*, Vol. IT-25, No. 5, September 1979, pp. 505-515.



*William A. Sandrin received a B.S.E.E. degree from the University of Vermont in 1963 and an M.E.E. degree from Rensselaer Polytechnic Institute in 1966. From 1966 to 1971, he worked for the Boeing Company, Aerospace Group, where he was involved in space communications system design and in the development of phased array antennas. In 1971, he joined COMSAT Laboratories, where he has been engaged in multibeam antenna studies; transponder linearizer development; transmission impairments analysis; studies of domestic, maritime, and aeronautical satellite systems; a study of adaptive phased array antennas for small-terminal applications; and frequency planning studies. He is presently a Research Scientist in the Communications Systems Studies Department of the Communications Techniques Division. Mr. Sandrin is a member of IEEE, Tau Beta Pi, and Eta Kappa Nu.*

*C. Harry Chen received a B.S.E.E. from National Taiwan University, Taiwan, China, in 1976, and an M.E. and Ph.D. from the University of Utah in 1978 and 1981, respectively. He joined COMSAT Laboratories in 1980 as Member of the Technical Staff in the Antenna and Propagation Laboratory, where he was involved in the design and development of microstrip antennas and slotted waveguide arrays for satellite communications applications. He was also involved in studying satellite antennas for the second-generation INMARSAT spacecraft, and microwave propagation through the precipitation medium. Dr. Chen left COMSAT Laboratories in April 1984 and is now with the Antenna Systems Laboratory at TRW, Redondo Beach, California.*



*Walter Hagmann received his Diploma in Electrical Engineering from the Swiss Federal Institute of Technology, Zurich, in 1976, and his Ph.D. from the University of Southern California in 1981. Since joining COMSAT Laboratories in 1981, he has worked on various problems related to satellite communications, with particular interest in the areas of small-user and mobile communications systems. In 1984, he joined the Brown Boveri Research Center in Switzerland.*



*Kenneth M. Mackenthun received a B.S.E.E. from George Washington University in 1974, and an M.S.E.E. and Ph.D. from the University of Illinois in 1976 and 1977, respectively. Since 1980, he has been in the Communications Systems Studies Department at COMSAT Laboratories. He is interested in signal design for the INTELSAT channel and the mobile-terminal-to-satellite transmission link.*

*Smith A. Rhodes received a B.S.E.E. from Virginia Polytechnic Institute in 1959 and an M.S.E.E. from North Carolina State University in 1962. From 1959 to 1965, he was a Member of the Technical Staff at Bell Laboratories, where he was engaged in various communications system studies. From 1965 to 1968, he was involved in digital communications studies for the R&D directorate of Page Communications. At Computer Services Corporation, he participated in digital satellite communications studies for military applications from 1968 to 1974. Since joining COMSAT in 1974, Mr. Rhodes has been engaged in system studies for satellite communications. He is currently a Research Scientist in the Communications Studies Department of the Transmission Systems Laboratory. His primary interests are in the digital communications area of modulation, synchronization, and error control. Mr. Rhodes is a member of the IEEE groups on Communications and Information Theory.*



Index: amplifiers, antennas, INTELSAT, MARISAT, transmission systems

## **An L-band active array system for global coverage\***

S. SIDDIQI, A. I. ZAGHLOUL, S. M. CHOU, AND R. E. EAVES†

(Manuscript received June 6, 1984)

### **Abstract**

A conceptual design and analysis of an L-band distributed-amplifier satellite antenna array system for global coverage are discussed. Several configurations, ranging from an element-fed to a subarray-fed active array, are analyzed. Aspects examined include antenna e.i.r.p. sensitivity to amplifier output variation, maximum amplifier output power, carrier-to-intermodulation ratio (C/IM), efficiency, beam-forming network (BFN) loss, layout complexity, weight of the subsystem, the graceful degradation property of such distributed systems, and overall reliability. The most favorable configuration is selected based on a detailed tradeoff analysis. It is shown that an active array offers high mass-power efficiency which can be readily implemented.

The statistical problem of antenna pattern degradation caused by variation in amplifier output is evaluated by three methods: a deterministic upper bound, a Monte Carlo method, and an analytic approach.

Three solid-state power amplifiers were designed and built, each providing 25-dB gain at 25-W output power. The changes in amplifier gain, phase, and noise-power ratio (NPR) over a 0° to 50°C temperature range were determined, and the performance of the three amplifiers was compared.

The performance of the active antenna system cannot be separated into antenna and power amplifier contributions, as in conventional designs. Measured solid-state power amplifier (SSPA) characteristics and computed array characteristics are combined

\* This paper is based on work performed at COMSAT Laboratories under the sponsorship of the International Telecommunications Satellite Organization (INTELSAT). Views expressed are not necessarily those of INTELSAT.

† With MITRE Corporation, Bedford, Massachusetts.

to treat the active antenna as a unified system. The results of this analysis verify that the design will meet demanding specifications of e.i.r.p., coverage, and c/I<sub>M</sub>, subject to the losses and variations that may be encountered in orbit.

## Introduction

On a geosynchronous satellite, an earth coverage antenna having a conventional beam shape such as that achieved with a single horn has an e.i.r.p. pattern which does not provide equal signal strength over the field of view (FOV). The edge of coverage (EOC), where the largest e.i.r.p. is required because of the added path loss and atmospheric attenuation, has the lowest gain. The subsatellite point, closest to the satellite, has the highest gain. In practical applications, the peak gain is usually forced high enough to satisfy the EOC requirement. This approach has been employed in INTELSAT programs primarily because of its simplicity.

The feasibility of achieving more efficient performance over the FOV has been demonstrated [1]–[3]. Ajioka and Harry [1] used a multibeam antenna to achieve a higher EOC gain than is possible with single-horn earth coverage. Carpenter [2] and Aasted and Roederer [3] designed an aperture distribution to produce a shaped beam which compensates for the additional losses occurring along paths to different points on the earth. In both instances, an array comprising a large central horn surrounded by a ring of smaller horns fed 180° out of phase with the central horn is employed. This approach is not practical at L-band, since the central horn becomes prohibitively bulky. An alternative is to approximate the aperture distribution with several smaller elements arranged in concentric rings, with equal excitation coefficients in each ring to maintain rotational symmetry.

The number of elements in the array determines the size, and hence the RF loss, of the BFN feeding the array. In a conventional system where a single high-power amplifier (HPA) feeds the antenna, the e.i.r.p. is reduced by the BFN loss. Consequently, it is desirable to have fewer elements in order to improve the overall efficiency of the system. A reasonable compromise is to use a sufficient number of elements and to divide the array into several subarrays, each fed by a lower power amplifier. This approach reduces the size of the BFN, and hence the loss, while improving the overall reliability of the system by graceful degradation and the use of low-power amplifiers. Also, any multipacting problems associated with HPAs are alleviated.

In the section that follows, the aperture synthesis procedure is described, followed by an analysis of several configurations ranging from an element-fed active array to a subarray-fed active array. BFN loss estimates based on measured data are presented. The most favorable configuration is then

selected, based on tradeoffs of mass, power, c/I<sub>M</sub>, and overall efficiency, and this configuration is analyzed in greater detail.

The statistical problem of an active array (i.e., the antenna performance degradations caused by random variations at amplifier outputs) is analyzed using three independent approaches. First, a deterministic approach is used to estimate an upper bound on the deviation from the optimum e.i.r.p. Next, a uniform distribution is assumed for both amplitude and phase, and a Monte Carlo technique is used to determine various statistical quantities. In the third approach, analytic expressions are derived for e.i.r.p. degradation at any point in the FOV, based on Gaussian and uniform amplitude/phase perturbations.

The design and performance of three SSPAs, each providing 25 W of output power, are described. Changes observed in amplifier gain, phase, and NPR over a 0° to 50°C temperature range are discussed. Other performance characteristics addressed are efficiency, linearity, variations due to drive levels, radiation effects, and reliability. Finally, overall system performance is evaluated.

## System considerations

In a conventional passive array system design (Figure 1), the power amplifier and the antenna are separate, sequential subsystems. For purposes of analysis, each subsystem can be individually characterized and the results combined to describe overall performance. In many potential applications, the total RF power required to meet e.i.r.p. specifications exceeds the capabilities of SSPAs, either individually or combined in small numbers. The alternatives are either extensive circuit-combining of SSPAs, which can be inefficient or impractical, or the use of TWTAs.

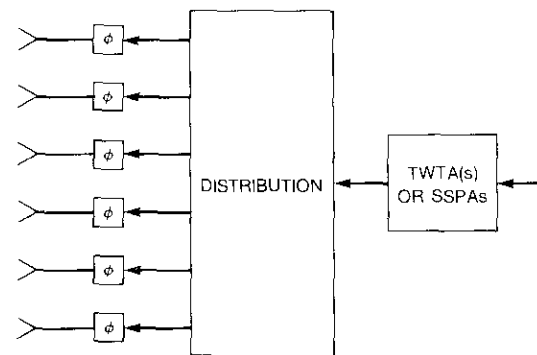


Figure 1. Conventional Phased-Array Configuration

For an active array system design (Figure 2), lower powered amplifiers (which can be SSPAs) are assigned to individual radiating elements or more generally to subarrays of the array. Because SSPAs are placed within the distribution network or between the distribution network and the radiating elements, the active antenna, including SSPAs, must be analyzed as a unified system.

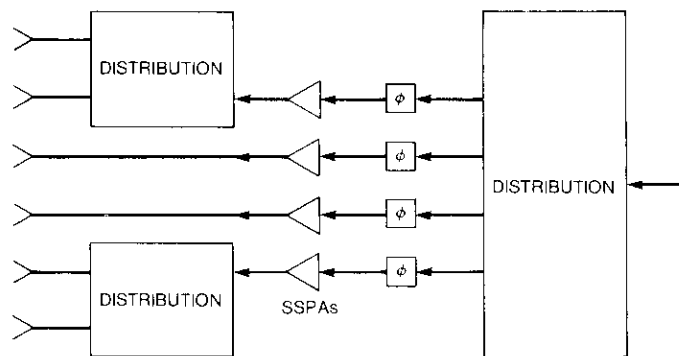


Figure 2. Active Antenna Configuration

One of the most significant advantages of an active array configuration is that amplitude/phase control, along with much of the distribution network, can be placed on the input side of the SSPAs, thereby overcoming the associated loss and avoiding reduction in e.i.r.p. In contrast, a conventional antenna design necessarily experiences loss only between the control RF source and the radiating elements.

When the active antenna is deployed in the space environment for a 10-year mission, the SSPA transfer characteristics can be expected to deviate slightly from the nominal amplitude and phase values. If the amplitudes of all SSPAs increase or decrease by the same amount, the antenna pattern will maintain the same shape, but down-link e.i.r.p. will experience a corresponding increase or decrease. If the phases of all SSPAs change by the same amount, no effective change will occur in the antenna pattern or in e.i.r.p. However, differential changes among SSPAs, either in amplitude or phase, can change both the pattern and the e.i.r.p.

Possible causes of deviation in SSPA amplitude and phase are as follows:

a. Differences among individual SSPAs in transfer phase characteristics vs input drive level. The SSPAs can be perfectly balanced in amplitude and phase at any given input level and ambient temperature (assumed

to be constant among all SSPAs), but unless the SSPAs track in exactly the same way, small imbalances can occur as ambient temperature and input drive change.

b. Small temperature differentials (<5°C) among individual SSPAs. The thermal subsystem is expected to minimize temperature spread among SSPAs as the ambient temperature swings between 0° and 50°C.

c. Radiation effects experienced over a period of 7 to 10 years in a space environment. A decrease in SSPA output power, even if uniform among all SSPAs, will reduce down-link e.i.r.p. Differential radiation effects among the SSPAs can alter the antenna pattern.

Another potential effect, separate from e.i.r.p. degradation, is the possibility that the antenna radiation pattern for the intermodulation products could differ from that for the wanted signal. This will occur if the amplitude and phase of the intermodulation products relative to those of the carrier vary among SSPAs. The resulting C/IM measured at some points on the earth could be worse (or better) than that measured at the output of individual SSPAs.

### Antenna configuration studies

The optimum beam shape for global coverage is shown in Figure 3. This beam shape compensates for the differential path lengths encountered between the satellite and various points on the earth.

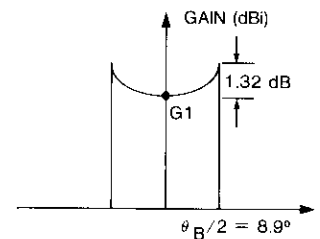


Figure 3. Global Coverage Pattern Compensating for Differential Path Length

To shape the far-field pattern of an antenna, the aperture distribution is synthesized by using the well-known Fourier series technique [4]. The circular aperture distribution,  $f(r)$ , must be represented in terms of a Fourier-Bessel series [5], as

$$f(r) = \sum_j b_j J_0(\beta_j r) \quad (1a)$$

$$b_j = \frac{g(\beta_j)}{\pi a^2 J_0^2(\beta_j)} \quad (1b)$$

where  $\beta_j = j$ -th zero of  $J_1(u)$   
 $u = (2\pi a/\lambda) \sin \theta$   
 $b_j =$  coefficients dependent on the desired antenna pattern  
 $g(\beta_j) =$  radiation pattern calculated at  $\beta_j$   
 $a =$  aperture radius  
 $\theta =$  radiation angle  
 $r =$  normalized aperture radius.

The number of terms to be used in the summation depends on the value of  $a$ . With the aperture radius limited to about 1 m by spacecraft constraints (about  $5\lambda$  at 1.5 GHz), and the maximum angle over which the radiation pattern is nonzero limited to  $8.9^\circ$  (includes a  $0.2^\circ$  pointing error), only two terms can be included in the series. Hence, the aperture distribution after normalization is given by

$$f(r) = 0.1188 J_0(\beta_1 r) + 0.8812 J_0(\beta_2 r) \quad (2)$$

Circular symmetry is implemented by arranging the elements in concentric circles around a central horn, where all the elements in a ring are excited with the same coefficient, given by equation (2). Several arrangements are possible where a central horn is surrounded by one ring ( $3.34\lambda - 7$  elements), by two rings ( $2\lambda - 19$  elements), by three rings ( $1.4\lambda - 37$  elements), or by four rings ( $1.1\lambda - 61$  elements). An array of more than four rings is not desirable since it would require an element of diameter less than  $1\lambda$ , and mutual coupling effects increase as element size decreases.

Candidate array elements must be capable of meeting stringent space requirements. Horns are a traditional choice, but the length required at L-band makes them unsuitable. Printed-circuit antennas have a narrow form factor and are lightweight; however, physically large printed-circuit arrays are not currently viewed as suitable for space applications because of the unavailability of materials that can withstand deformation caused by thermal gradients across the antenna aperture. An antenna feed element (dipole, spiral, etc.) which is smaller than  $1\lambda$  in diameter, placed precisely in a  $1\lambda$ -diameter,  $\lambda/2$ -deep cylindrical cup, has proved to be a very efficient radiator (almost 100 percent) [6],[7], and thus was chosen for the present application.

Figure 4 shows an array of 61 circularly polarized (CP) cup dipole elements arranged in four concentric circles around a central horn. The excitation coefficients, calculated from equation (2) by substituting for the normalized

radius,  $r$ , at points which correspond to the centers of these elements, are as follows:

$$\begin{aligned} f(0) &= 1 \\ f(0.22) &= 0.86 \\ f(0.44) &= 0.47 \\ f(0.66) &= -0.077 \\ f(0.88) &= -0.188 \end{aligned}$$

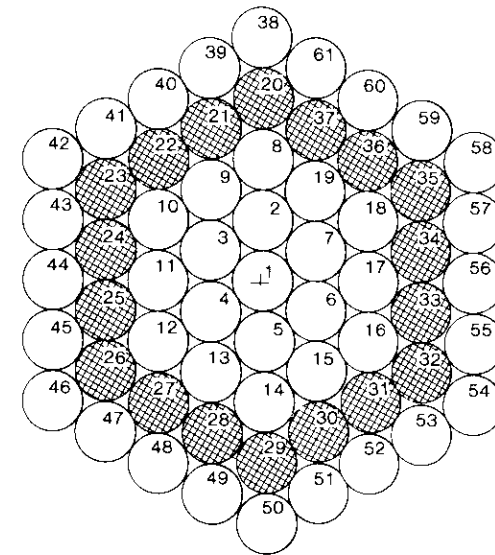


Figure 4. Antenna Array

The far field of the array was calculated by using a measured isolated single-element pattern. Subsequent numerical optimization improved the pattern fit. The final far-field patterns are shown in Figure 5. The 18 elements of the third ring (cross-hatched in Figure 4) have been assigned zero excitation coefficients with negligible effect on the far-field pattern. This reduces the complexity of the BFN, since the number of excited elements in the array is now only 43.

In a conventional passive antenna system, a 1-input/43-output BFN is needed to provide the appropriate feed excitations. As noted above, such a system is inefficient because the e.i.r.p. is directly reduced by the loss in

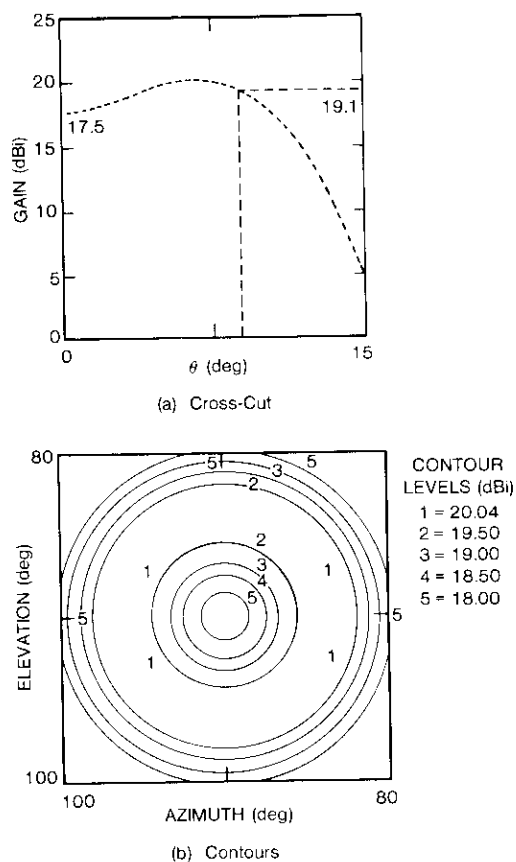


Figure 5. Final Far-Field Patterns

the network, and the alternative is to equip each element with its own power amplifier. Such an element-fed active array, however, requires a large number of unequal power amplifiers, which presents significant design and implementation problems.

An alternate approach is to divide the array into subarrays, each of which requires the same power and is fed by identical amplifiers (Figure 2). In this case, the subarrays may not necessarily contain the same number of elements, and consequently their corresponding feed networks may have different losses.

Figure 6 shows four configurations for partitioning the 43-element array into 4, 7, 8, or 10 subarrays requiring equal power and possessing near-

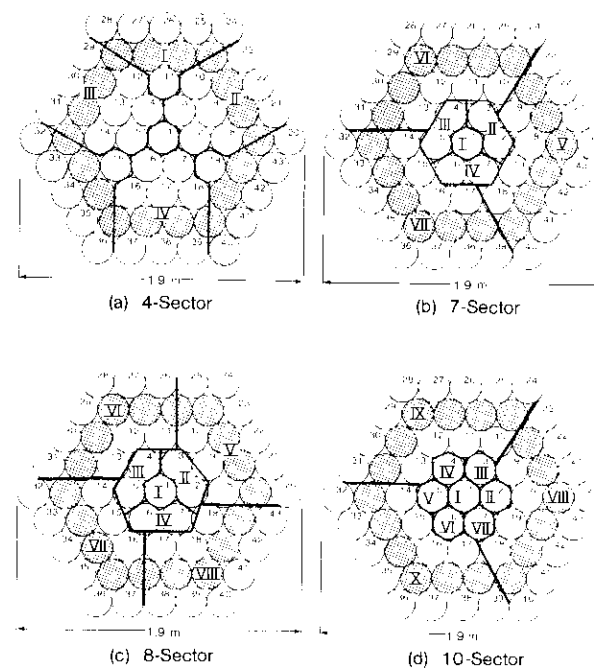


Figure 6. Partitioning of the 43-Element Array

optimum excitation. Forcing the subarrays to have equal power perturbs the excitation coefficients of the elements from the optimum case. Far-field patterns of the four configurations are shown on the same scale in Figure 7. The EOC gain varies by, at most, 0.1 dB from the optimum for all four cases. The shape of the pattern remains essentially the same, and circular symmetry is maintained.

The four configurations were compared, assuming an e.i.r.p. requirement of 39.3 dBW for each case. This comparison included BFN loss, sensitivity to amplifier output variation, amplifier output power, linearity and efficiency, and overall weight. It was observed that the larger the number of amplifiers, the less effect a change in their outputs has on the antenna pattern.

Two transmission line media were investigated for BFN realization: air stripline (also known as barline) and squareax. A stripline loss of 0.005 dB/cm was measured, with an estimated dielectric loss contribution of 0.003 dB/cm. This value can be reduced by using lower loss dielectric materials. The measured losses of stripline 3- and 6-dB couplers were 0.09 and 0.04 dB, respectively. On the other hand, the squareax losses incurred

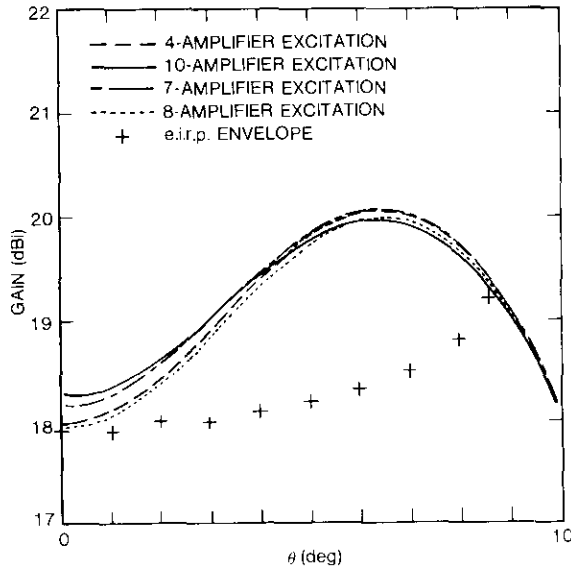


Figure 7. Summary of the Beam-Shaping Capability of all Configurations

are estimated to be 0.001 dB/cm, and 0.05 dB/coupler. The loss in the BFN for the various configurations was calculated based on the above loss values. Table 1 shows the estimated loss values of each sector for each configuration in both stripline and squareax networks.

TABLE 1. BFN LOSS FOR EACH ARRAY CONFIGURATION

CONFIGURATION	NO. OF ELEMENTS PER AMPLIFIER UNIT		LOSS FOR STRIPLINE (dB)	LOSS FOR SQUAREAX (dB)
		SECTION		
4 SSPA	19	I	1.2	0.4
	8	II-IV	0.5	0.26
7 SSPA	12	V-VII	0.65	0.314
	2	II-IV	0.1	0.05
	1	I	<0.1	<0.05
8 SSPA	1	I	<0.1	<0.05
	2	II-IV	0.1	0.05
	9	V-VIII	0.75	0.28
10 SSPA	1	I	<0.1	<0.05
	1	II-VII	<0.1	<0.05
	12	VIII-X	0.6	0.31

TABLE 2. COMPARISON OF THE VARIOUS CONFIGURATIONS STUDIED FOR THE DISTRIBUTED AMPLIFIER APPROACH

NO. OF SSPAs	DIRECTIVITY (dBi)	BFN LOSS <sup>b</sup> (dB)	LINEAR RF POWER REQUIRED <sup>b</sup> (W)		OUTPUT BACKOFF (dB)	OVERALL AMPLIFIER EFFICIENCY (%)	TOTAL DC POWER (W)	OVERALL TRANSDUCER EFFICIENCY <sup>d</sup> (%)	WEIGHT OF POWER AMPLIFIERS <sup>e</sup> (kg)
			TOTAL	PER SSPA					
4	19.2	1.3	144.4	36.1	1.12	34	424	24.1	21
7	19.15	0.65	126	18	1.91	30.6	412	25.1	24
8	19.15	0.75	128.8	16.1	2.39	27.5	470	22.0	27
10	19.10	0.6	126	12.6	2.1	29.7	424	24.7	31

<sup>a</sup> Estimated—stripline medium.  
<sup>b</sup> Required linear output power with the appropriate output backoff, calculated as  $P \text{ (dBW)} = 39.3 - \text{gain (dBi)} + 0.2 + \text{BFN loss (dB)}$ . Includes 0.2-dB switch/cable loss.  
<sup>c</sup> Includes power supply efficiency of 85 percent.  
<sup>d</sup> Given by total radiated power (linear power - BFN loss)/total DC power.  
<sup>e</sup> Estimated weight of the power amplifiers and their power supplies. A 2-for-1 redundancy is assumed for the SSPAs.

Table 2 summarizes the comparison of each of the four configurations. The 10-sector configuration is selected for three reasons: lower SSPA power (more reliable), increased output backoff on the SSPAs (better C/IM performance), and less sensitivity to changes in amplifier outputs (more reliable). Overall efficiency is calculated assuming the highest BFN loss for all sectors. If the differential losses were included in the sectors, higher efficiency would result. A weighted average RF loss is about 0.25 dB.

The three largest power distribution networks (1 input/12 outputs) have an estimated 0.6-dB RF loss in stripline medium. The other seven SSPAs are directly connected to the feed elements, incurring a loss of 0.1 dB. Figure 8 shows the effect of differential loss on the far-field pattern. Less than 0.1-dB variation from the optimum case at EOC was observed.

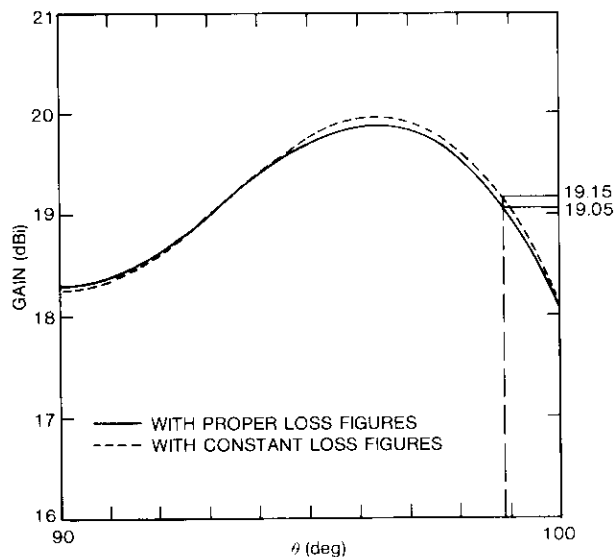


Figure 8. Patterns Showing the e.i.r.p. Variation due to Unequal Loss Numbers in Different Sections of the BFN

**Active antenna sensitivity**

This section presents a parametric assessment of the effects of SSPA output amplitude and phase deviations on e.i.r.p., without making *a priori* estimates of the causes. Three separate but complementary approaches have been taken: deterministic upper bound on e.i.r.p. degradation, Monte Carlo analysis of

e.i.r.p. variation in FOV, and statistical analysis of worst-case e.i.r.p. degradation.

For an array of identical coplanar elements fed by  $N$  amplifiers such that each amplifier  $i$  ( $i = 1, \dots, N$ ) feeds  $M_i$  elements, the far-field  $E(\theta, \phi)$  is given, except for a proportionality factor, by

$$E(\theta, \phi) = E_{ec}(\theta, \phi) \sum_{i=1}^N A_i e^{j\beta_i} F_i \tag{3}$$

where 
$$F_i = \sum_{m=1}^{M_i} a_{m,i} e^{j(u x_{m,i} + v y_{m,i})}$$

- $E_{ec}(\theta, \phi)$  = element pattern in direction  $(\theta, \phi)$
- $a_{m,i} = |a_{m,i}| e^{j\psi_{m,i}}$  complex excitation coefficient of the  $m$ -th element fed by the  $i$ -th amplifier
- $x_{m,i}, y_{m,i}$  = coordinates of the  $m$ -th element fed by the  $i$ -th amplifier
- $u = k \sin \theta \cos \phi$
- $v = k \sin \theta \sin \phi$
- $k = 2\pi/\lambda$
- $A_i = 1 + \alpha_i$ ,  $\alpha_i$  = the random perturbation of the amplitude of the  $i$ -th amplifier relative to a nominal value of unity
- $\beta_i$  = the random perturbation of the phase of the  $i$ -th amplifier.

The e.i.r.p. in direction  $(\theta, \phi)$  is proportional to the power  $P(\theta, \phi)$  radiated in that direction. The power pattern normalized to the element pattern is given by

$$P = \sum_{i=1}^N A_i |F_i|^2 + \sum_{i=1}^N \sum_{\substack{j=1 \\ i \neq j}}^N A_i A_j e^{j(\beta_i - \beta_j)} F_i F_j^* \tag{4}$$

where \* denotes the complex conjugate.

**Deterministic upper bound**

Using the field and power expressions of equations (3) and (4), the ratio of perturbed e.i.r.p. to unperturbed e.i.r.p. can be bounded through the Schwartz inequality.

For the 10-SSPA active array described previously, the bound on the e.i.r.p. variation can be shown to be

$$\frac{P_o + \delta P}{P_o} \leq (1 + 1.24 \Delta_{\max})^2 \tag{5}$$

where  $\Delta_{\max} = \max \{|\Delta_i|\} = (\alpha_{\max}^2 + \beta_{\max}^2)^{1/2}$ . Figure 9 shows this bound for different values of  $\alpha_{\max}$  and  $\beta_{\max}$ .

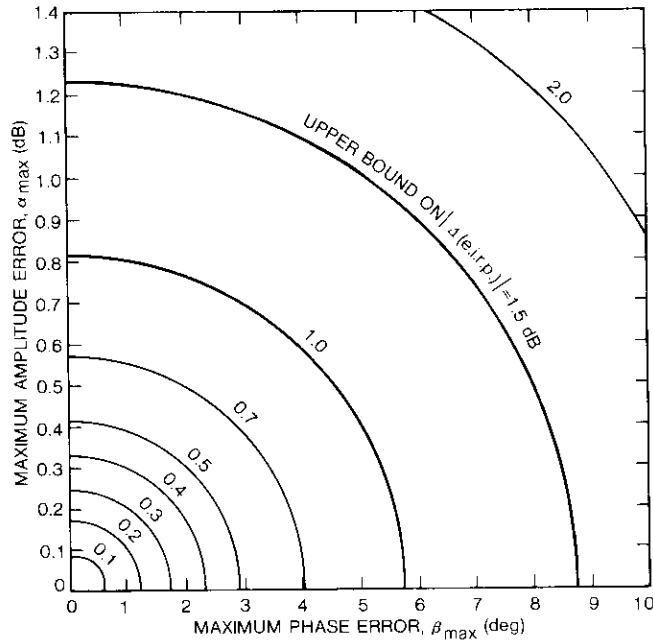


Figure 9. Deterministic Upper Bound on e.i.r.p. Degradation

The upper bound is known exactly for the case when there is no phase error ( $\beta_i = 0$  for all  $i$ ) and all amplitude errors are the same ( $\alpha_i = \alpha_{\max}$  for all  $i$ ). Beam shape is preserved and e.i.r.p. changes exactly by

$$\frac{P_o + \delta P}{P_o} = (1 + \alpha_{\max})^2 \tag{6}$$

so that the bound given by equation (5) is larger by about 24 percent in dB for small errors.

For cases involving phase error, computer trials were run to find the worst-case assignment of errors among the subarrays. These results are not exhaustive, but the worst cases among them are approximately 40 percent less severe in dB than the bound given by equation (5).

These observations suggest that

$$\frac{P_o + \delta P}{P_o} \leq \left[ 1 + \left( \alpha_{\max}^2 + \beta_{\max}^2 \right)^{1/2} \right]^2 \tag{7}$$

could be adopted as a practical guide for active antenna design. Equation (7) describes e.i.r.p. degradation approximately 24 percent less severe in dB than that shown in Figure 9.

**Monte Carlo analysis**

An empirical technique used to estimate the performance degradation of the antenna due to random amplitude and phase variations is the Monte Carlo technique. A set of random amplitude and phase distributions can be generated within prescribed limits, assuming uniform probability distributions. The perturbed far field is then calculated, and the difference between this pattern and the unperturbed pattern is plotted. The point of greatest reduction in directivity is located, and the change is noted. The procedure is repeated a number of times for each prescribed maximum deviation, and various statistical quantities are then calculated.

Table 3 summarizes the results obtained by using the Monte Carlo procedure for the active antenna under consideration. The e.i.r.p. change at edge of the global coverage is shown. For each combination of maximum amplitude and phase variations, the table gives the mean, the standard deviation, and the  $3\sigma$  value indicating the results (performance) that can be expected in 99.7 percent of the cases. The worst-case e.i.r.p. change among the 30 attempts for each case is also given.

TABLE 3. MONTE CARLO RESULTS FOR UNIFORM AMPLITUDE AND PHASE VARIATIONS

DEVIATE AMPLITUDE AND/OR PHASE	EOC e.i.r.p. CHANGE					NUMBER OF ATTEMPTS
	MEAN	STANDARD DEVIATION	WORST CASE	VARIANCE	3 $\sigma$ VALUE	
$\pm 0.5$ dB	-0.02	0.026	-0.13	0.0006	-0.098	30
$\pm 1$ dB	-0.056	0.045	-0.17	0.002	-0.191	30
$\pm 3^\circ$	-0.072	0.069	-0.3	0.005	-0.279	30
$\pm 5^\circ$	-0.076	0.097	-0.4	0.009	-0.367	30
$\pm 7.5^\circ$	-0.236	0.160	-0.75	0.026	-0.716	30
$\pm 0.5$ dB and $5^\circ$	-0.124	0.126	-0.4	0.016	-0.504	30
$\pm 1$ dB and $\pm 5^\circ$	-0.192	0.118	-0.45	0.014	-0.546	30

Examination of Table 3 reveals that phase variation is more critical than amplitude variation. For example, a maximum of  $\pm 1$ -dB amplitude variation

alone can cause an EOC e.i.r.p. degradation of a maximum of 0.191 dB for 99.7 percent of the time, whereas a  $\pm 5^\circ$  phase variation alone causes an EOC directivity degradation of 0.367 dB for the same percent of the time. A combination of the two ( $\pm 1$  dB for amplitude and  $\pm 5^\circ$  for phase) degrades EOC performance by 0.546 dB, which is almost a linear sum of the individual components.

**Statistical analysis**

A rigorous statistical analysis can be performed on the power expression of equation (4) to estimate the worst-case degradation of the active antenna e.i.r.p. In this analysis, the independent amplitude and phase variables  $\alpha_i$  and  $\beta_i$  may assume different probability distributions. For amplitude variations, the probability density function of  $\alpha_i$  can be of uniform distribution between  $\pm \Delta_a$  or Gaussian distribution with zero mean and variance of  $\sigma_a^2$ . For phase variations, the probability density function of  $\beta_i$  can be of uniform distribution between  $\pm \Delta_b$  or Gaussian distribution with zero mean and variance of  $\sigma_b^2$ . The expected value,  $\bar{P}$ , and the variance,  $\text{var}(P)$ , can be expressed in closed forms by performing the integrations to estimate the first and second moments of the array power [8]. The standard deviation,  $\sigma(P)$ , or the square root of the variance, indicates the extent of array e.i.r.p. degradation.

Using the central limit theory, the probability density distribution of the e.i.r.p. will approach a Gaussian distribution with mean  $\bar{P}$  and standard deviation  $\sigma(P)$ . Normalizing  $\bar{P}$  and  $\sigma(P)$  with respect to the unperturbed power  $\bar{P}_0$  gives the degradation in the array e.i.r.p. The quantity  $[\bar{P} - 3\sigma(P)]/\bar{P}_0$  corresponds to a  $3\sigma$  degradation in e.i.r.p. and represents the worst case for 99.7 percent of all possible cases for the given amplitude and phase random distributions.

Applying this analysis to the antenna configuration described previously leads to a set of parametric curves representing the e.i.r.p. degradations for different values of amplitude and phase perturbations. These curves can be used as design curves for the allowable levels of amplitude and phase perturbations, such that the worst-case degradation at any point in the coverage area does not fall below a certain level. Figure 10 shows the case with uniform amplitude and uniform phase distributions, Figure 11 represents the combination of uniform amplitude and Gaussian phase distributions, Figure 12 illustrates the combination of Gaussian amplitude and uniform phase distributions, and Figure 13 shows the Gaussian amplitude and Gaussian phase distribution situation.

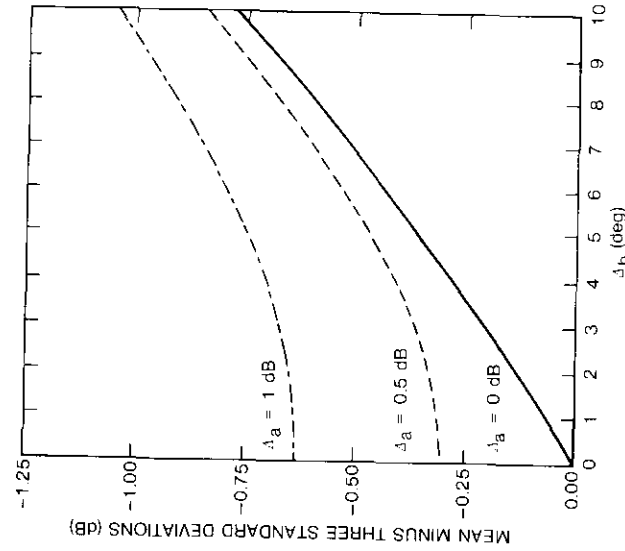


Figure 10. Worst-Case e.i.r.p. Degradation in Coverage Area for Random Perturbations of Uniform Amplitude and Uniform Phase Distributions

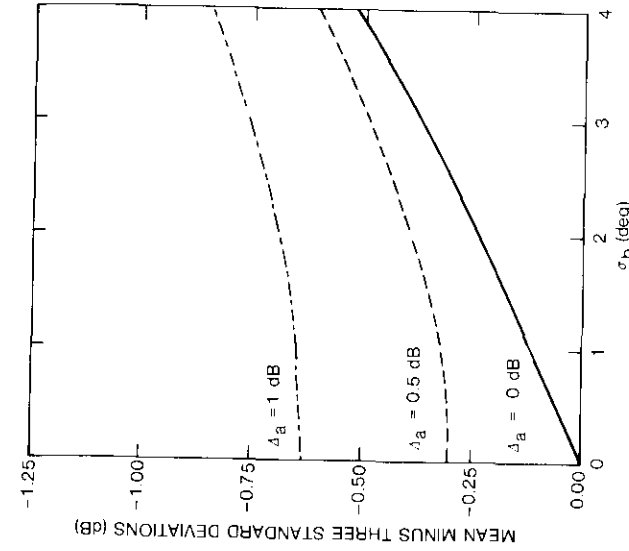


Figure 11. Worst-Case e.i.r.p. Degradation in Coverage Area for Random Perturbations of Uniform Amplitude and Gaussian Phase Distributions

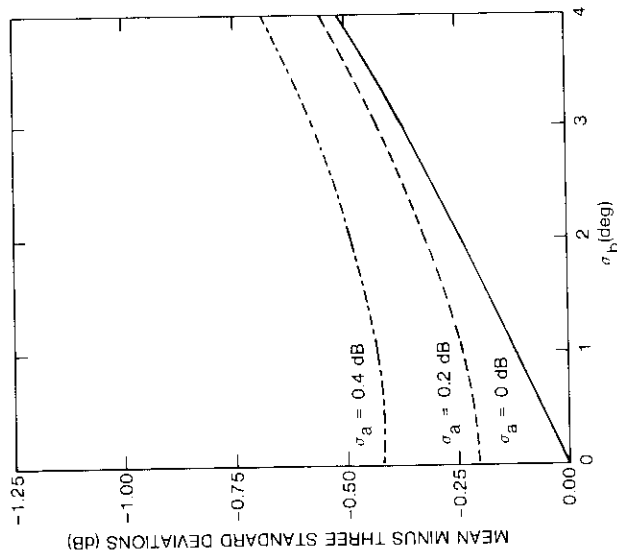


Figure 13. Worst-Case e.i.r.p. Degradation in Coverage Area for Random Perturbations of Gaussian Amplitude and Gaussian Phase Distributions

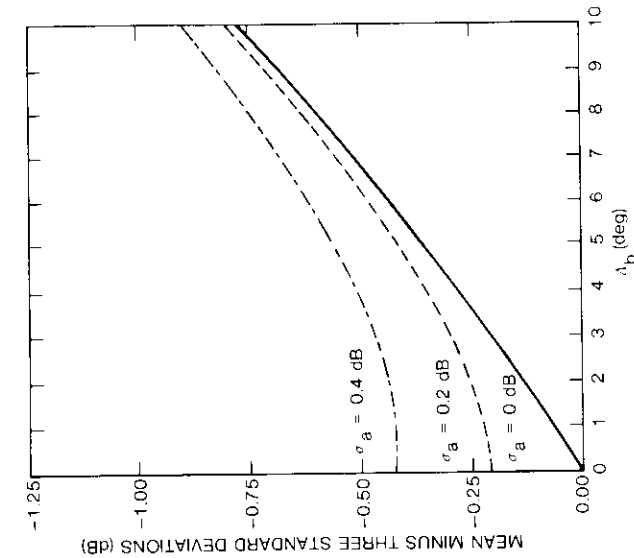


Figure 12. Worst-Case e.i.r.p. Degradation in Coverage Area for Random Perturbations of Gaussian Amplitude and Uniform Phase Distributions

### L-band solid-state power amplifiers

The use of SSPAs in an active antenna array design provides advantages over conventional TWTAs in low-voltage power supply, lighter weight, distributed thermal load, and potentially higher reliability. Equal-powered SSPAs are used to feed each of the several sectors of the array. The sensitivity analyses described in the previous section show that the array e.i.r.p. is sensitive to changes in both the relative phases and the output powers of the SSPAs.

The objective of the work described in this section was to investigate the suitability of L-band SSPAs for use in active antenna array design. Specifically, hardware design, fabrication, assembly, and testing of a number of amplifiers were performed to determine, verify, and demonstrate SSPA performance under space environmental conditions.

#### SSPA description

Three 2-stage SSPAs with space-qualified output stage devices were designed, fabricated, and tested. The SSPAs are identical in all aspects. The results are presented following a description of the SSPA.

Figure 14 is a block diagram of the 2-stage L-band SSPA, with its power and gain level, and Figure 15 is a photograph of the assembled 2-stage SSPA. A power-combined stage using two 90° Lange couplers is driven by a single

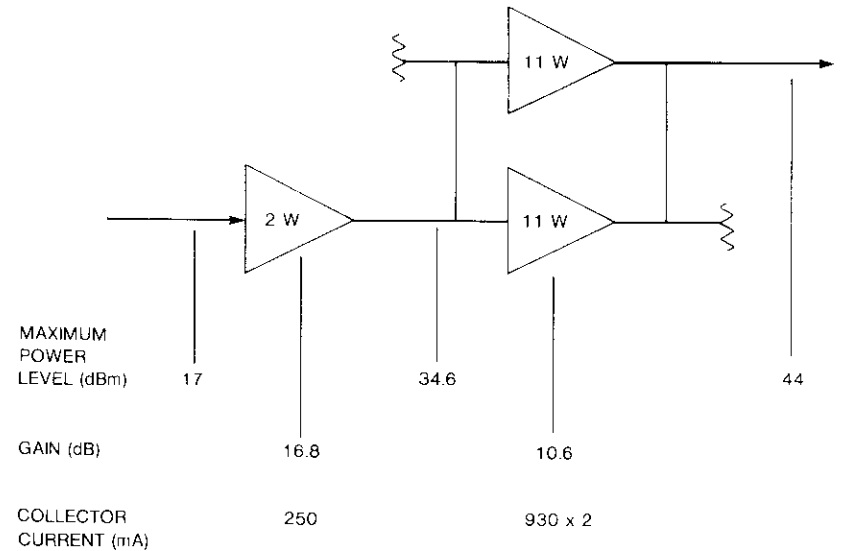


Figure 14. Block Diagram of L-Band SSPA

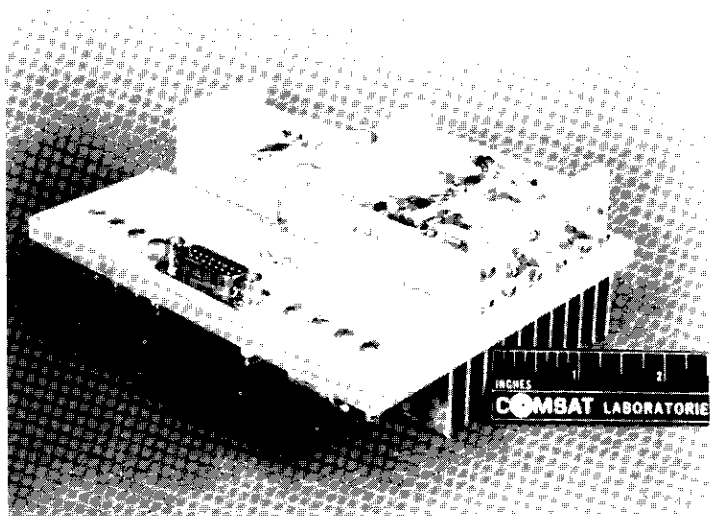


Figure 15. 2-Stage L-Band SSPA

mid-power stage. At 1.54 GHz, the amplifier provides a 27-dB nominal gain with 17-dBm input RF power. The input and output matching circuits are realized in a microstrip transmission line on 25-mil-thick alumina substrate, and the Lange coupler hybrids are fabricated on 50-mil-thick alumina substrates. The circuit loss in the hybrid is 0.15 dB per path (typical). The substrates are soldered on a Kovar carrier. The devices are mounted on a ridge of aluminum housing between the input and output matching circuits to provide a good heat sink. Regulated DC power to the transistors is provided by a DC current-limited voltage regulator which permits individual adjustment of the bias to each transistor. The amplifier measures 16 × 6.5 × 2.5 cm and weighs 300 g.

**Test results**

OUTPUT POWER, GAIN, AND PHASE SHIFT

Figure 16 shows the typical measured transfer characteristics of an SSPA under three temperature conditions (0°, 25°, and 50°C) at 1.54 GHz. The small-signal gain and output power dependence on frequency and temperature are listed in Table 4. The variation of small-signal gain for each frequency is within 0.2 dB over the 0° to 50°C range. Frequency-dependent variations in small gain and output power at 13-dBm input drive are all within 0.5 dB.

The input/output transfer characteristics of the three SSPAs at 1.54 GHz

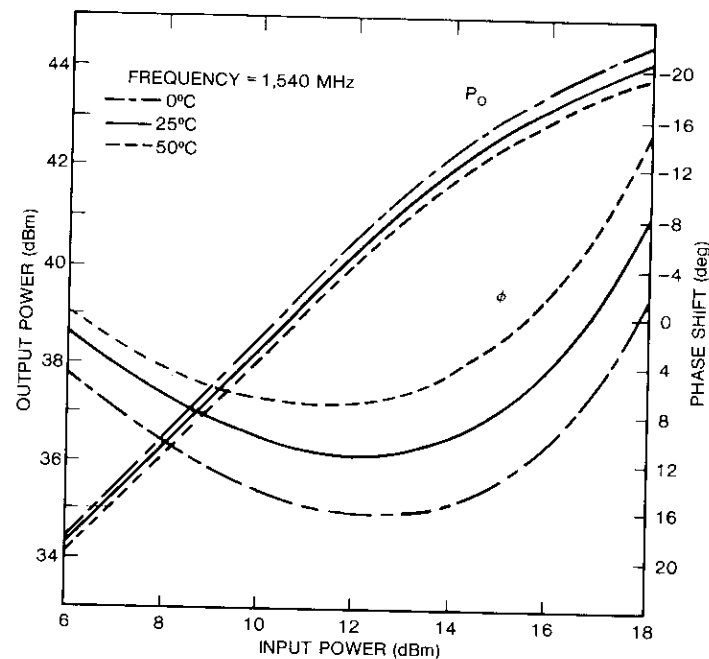


Figure 16. Typical Transfer Characteristics and Phase Shift

TABLE 4. SMALL-SIGNAL GAIN AND OUTPUT POWER CHARACTERISTICS OF SSPA 1

FREQUENCY (MHz)	SMALL-SIGNAL GAIN (dB)			OUTPUT POWER (dBm) AT 13-dBm INPUT		
	0°C	25°C	50°C	0°C	25°C	50°C
1,530	27.8	27.8	27.7	40.84	40.8	40.5
1,540	28.4	28.35	28.2	41.5	41.25	41.0
1,546	28.4	28.3	28.2	41.5	41.3	41.0

were measured at a nominal operating output power level of 41 dBm (10-carrier C/I requirement of 13.5 dB). The results show an output power variation of ±0.2 dB and phase tracking within -1.4° to 2.4° among the three SSPAs over the 50° temperature range. Since the devices were selected randomly, these results provide sufficient information to estimate that ±0.2 dB and ±3° are realistic bounds on the SSPA amplitude and phase tracking characteristics, respectively.

## INTERMODULATION AND NOISE POWER RATIO

The carrier-to-third- and fifth-order intermodulation product ratios ( $C/3IM$  and  $C/5IM$ ) of the three SSPAs were measured with two equal amplitude carrier signals spaced 2 MHz apart. Figure 17 plots the results for an SSPA at room temperature. Similarity in the  $C/IM$  characteristics of the SSPAs was observed in all the amplifiers. The variation at a constant 41-dBm output level is typically  $\pm 0.9$  dB for the three SSPAs.

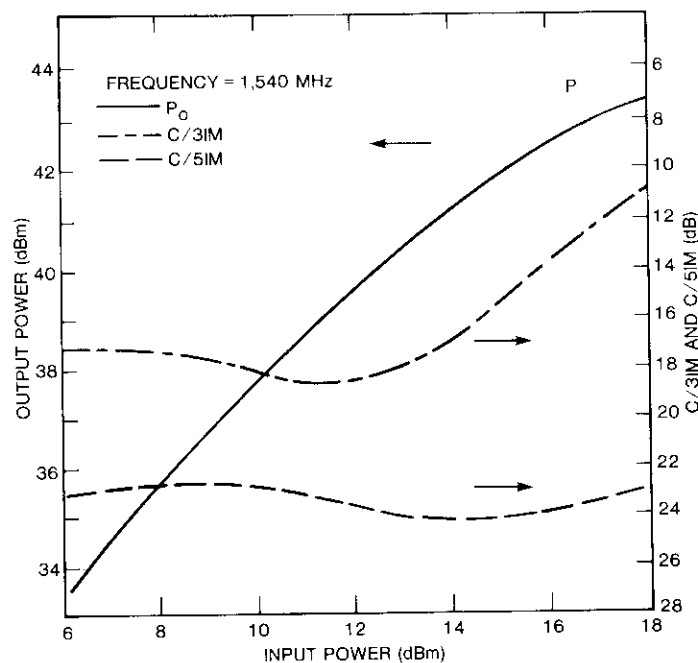


Figure 17. Third- and Fifth-Order Intermodulation

Figure 18 shows the typical output power and NPR vs input drive level at three temperatures in the  $0^\circ$  to  $50^\circ$  range for a multicarrier input. The SSPAs are tuned to achieve maximum output power at mid-frequency. At the minimum useful output power of 41.0 dBm, NPR varies no more than  $\pm 0.2$  dB (from the room temperature value of 13 dB) over the  $50^\circ\text{C}$  range. The observed change in NPR due to temperature variation is directly related to the output power level.

The intermodulation characteristics of this amplifier design are predicted by the size of the driver stage. To assess the improvement in overall NPR,

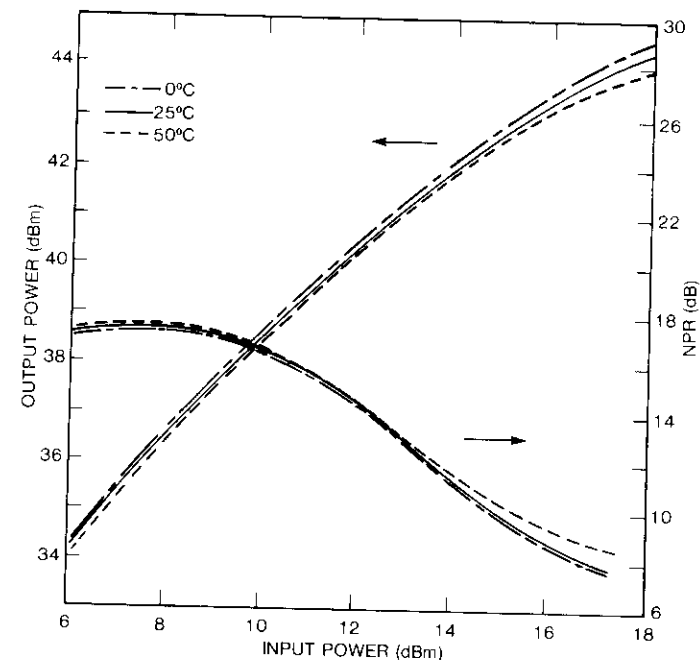


Figure 18. Typical NPR Change Over  $50^\circ\text{C}$  Temperature Range

an 11-W driver stage was used in place of the 2-W driver stage. At 41-dBm output, a 2-dB improvement in NPR is observed, with overall efficiency lowered by about 2 percent. Further improvements in design configurations are conceivable to optimize the RF output power, NPR, and efficiency. For example, a 5-W device could be used for the driver stage or an 11-W driver could be shared by two amplifiers. The most favorable driver amplifier configuration to improve the linearity margin without significantly reducing overall efficiency can be selected at the implementation stage.

## EFFICIENCY, OUT-OF-BAND RESPONSE, AND HARMONICS

Figure 19 plots the output power and collector efficiency of the 2-stage SSPA vs input drive level. The minimum collector efficiency of the 2-stage amplifier is 36.5 percent at a useful output power level of 41 dBm.

The measured frequency response of the amplifiers shows an output power variation of less than  $\pm 0.1$  dB at room temperature over the required 15 MHz transmit frequency band. Figure 20 shows the measured out-of-band frequency response of the SSPA up to 1.7 GHz.

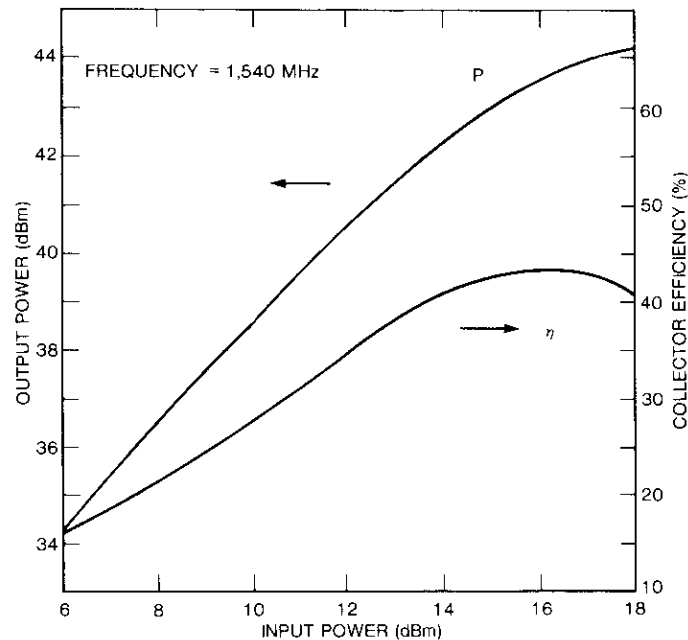


Figure 19. Collector Efficiency of the 2-Stage SSPA

The measured harmonic frequency output characteristics of the 2-stage SSPA are shown in Figure 21. It should be noted that the SSPA output circuit design did not include a harmonic output rejection filter. The fourth harmonic (around 6 GHz) is at least 60 dB below the fundamental.

#### RADIATION EFFECTS

It has been previously reported that small-signal microwave bipolar transistors are sensitive to radiation doses encountered in a 10-yr space mission in geosynchronous orbit [9],[10]. The largest radiation effect reported was a reduction of the DC current gain, which could result in significant loss in power gain.

Radiation tests were conducted on the SSPAs using the cobalt-60 gamma cell calibrated in mid-1980 by the National Bureau of Standards. The driver stage amplifier was subjected to a dose rate of 4.32 krad/min. for a total of 3.85 hr, equivalent to a dose of  $10^6$  R during the test. The collector current and output power showed no effects from gamma irradiation at high or low power levels. The expected damage mechanism is that of a trapped charge (in the dielectric surface passivation layers) altering the leakage current and,

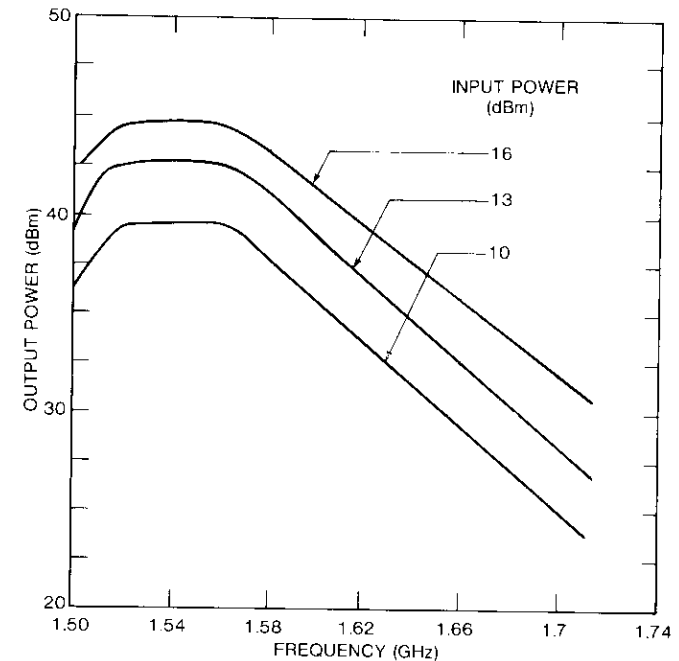


Figure 20. Frequency Response of SSPA in 1.5- to 1.7-GHz Band

therefore, the gain of the device. Since the passivated areas (oxide coated) are small compared to the contact areas of a high-power device, any change in the oxide charge would produce only a small change in the overall device characteristics.

There are two possible explanations for the fact that no change was observed, even at the low-power levels where changes were reported in similar devices. First, the devices reporting sensitivity to radiation were fabricated using mid-1970s technology. A new radiation-hardened-oxide technology could be employed, in which case no changes in the oxide would be expected.

Another possibility involves the metal contacts themselves. When extremely high gain is not required from a device, there is no need to reduce the surface recombination at the contacts. If no special contact treatment (such as poly silicon) is employed, then the device-saturated reverse dark currents will be so high (as fabricated) that any changes in the passivation oxides will have no noticeable effect on the devices. Since the devices tested are power transistors and do not require high gain, this explanation appears to be the most probable.

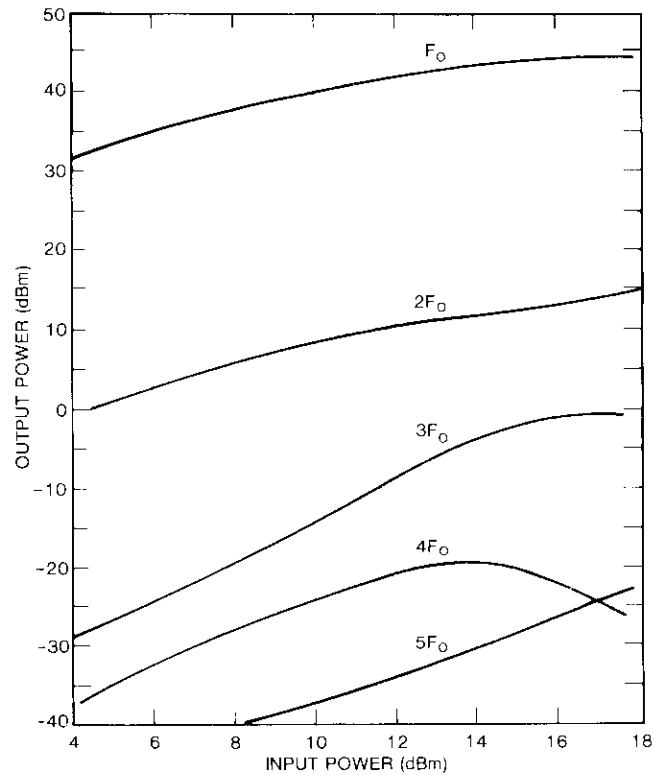


Figure 21. Measured Power Level of All Harmonics of the 2-Stage SSPA

### Applications and conclusions

The variations in SSPA amplitude and phase characteristics discussed herein provide the required inputs for antenna sensitivity analysis. The SSPA measurements show that the worst-case output occurs at 50°C, and that the unit-to-unit mean output level will be approximately 0.3 dB higher at 25°C and 0.5 dB higher at 0°C. If the 10 SSPAs in the active antenna configuration are initially adjusted in amplitude and phase to balance at a uniform temperature of 25°C, the contributions to imbalance under operating conditions are estimated to be those presented in Table 5. The three operating temperatures are identified as nominal to indicate that the temperatures of individual SSPAs in the configuration can deviate by as much as 5°C.

Although the nominal temperature of 0°C results in the largest deviation in amplitude and phase, it also is the temperature at which the mean SSPA

TABLE 5. CONTRIBUTIONS TO AMPLITUDE AND PHASE VARIATIONS ABOUT THE MEAN AT DIFFERENT TEMPERATURES

PARAMETER	AMPLITUDE (dB)			PHASE (deg)		
	0°C	25°C	50°C	0°C	25°C	50°C
Unit-to-Unit Variation	±0.15	0	±0.15	±2.0	0	±1.2
Temperature Differential	±0.02	±0.02	±0.02	±0.3	±0.3	±0.3
Radiation Effects	Neg.	Neg.	Neg.	Neg.	Neg.	Neg.
Additional Margin	±0.03	±0.03	±0.03	±0.7	±0.7	±0.7
Total Allowance	±0.2	±0.05	±0.2	±3	±0.1	±2.2

output is greatest. This more than offsets the effects of imbalance on e.i.r.p. The worst-case e.i.r.p. that can be encountered occurs at 50°C and dictates SSPA design requirements.

The results on a deterministic upper bound to e.i.r.p. degradation shown in Figure 10 indicate that the degradation corresponding to ±0.2 dB amplitude and ±2.2° phase deviations will be less than 0.43 dB with absolute certainty. It was observed, however, that this bound does not appear to be tight, and that equation (5) can be adopted as a practical upper bound. The corresponding e.i.r.p. degradation is ≤0.3 dB.

If amplitude and phase variations are assumed to be uniformly distributed between ±0.2 dB and between ±2.2°, the Monte Carlo simulation results given in Table 3 can be used to estimate e.i.r.p. degradation through interpolation. This indicates that, with probability 0.997, the largest degradation within the FOV will be less than 0.25 dB.

The same uniform distribution of amplitude and phase can be assumed for the analytical results shown in Figures 11 through 14. It was determined that for any one specified point within the FOV (taken to be a point at  $\theta = 8.9^\circ$  as a worst case), the largest e.i.r.p. degradation will be less than 0.20 dB, with probability 0.997. Alternately, it could be assumed that amplitude and phase are Gaussian in distribution and that 95 percent of the SSPAs employed conform to the ±0.2 dB, ±2.2° limits. In this case, with probability 0.997, the e.i.r.p. degradation for any one specified point will be less than 0.15 dB.

Based on these results, the system design tolerance for e.i.r.p. degradation has been chosen to be 0.3 dB. The corresponding active antenna budget for e.i.r.p. and losses is given in Table 6. The SSPA measurements indicate that the intermodulation phase tracks the carrier phase to within the measurement error, ±1°. Consequently, C/IM in the FOV is the same as C/IM at the output of individual SSPAs.

TABLE 6. e.i.r.p. MARGIN FOR SSPA—ACTIVE ANTENNA CONFIGURATION

SSPA Output Power	11 dBW (12.6 W)
Contribution of 10 SSPAs	10 dB
Output Circuit Loss	
Coaxial Cable	0.1 dB
Redundancy Switch	0.1 dB
BFN (squareax)	0.3 dB
Total	0.5 dB
Antenna Gain (EOC)	19.1 dBi
Tolerance (due to amplitude/phase variations)	0.3 dB
e.i.r.p. Achievable	39.3 dBW
e.i.r.p. Specification	39.0 dBW
Margin	0.3 dB

The results developed here indicate that the selected bound on phase difference could result in an e.i.r.p. difference of 0.15 dB at most. Thus, an additional 0.2-dB margin for C/M at the SSPA output would be adequate to protect against this speculative possibility.

### Acknowledgments

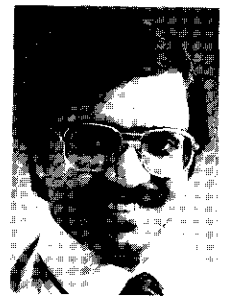
The authors would like to acknowledge the continued support of R. M. Sorbello of COMSAT Laboratories, A. Atia of INTELSAT Technical Services, and G. J. P. Lo of INTELSAT throughout the course of this study. Thanks are also due to L. MacGinitie, A. Meulenber, Jr., P. Ross, and M. Urcuyo for their contributions.

### References

- [1] J. S. Ajioka and H. E. Harry, "Shaped Beam Antenna for Earth Coverage From a Stabilized Satellite," *IEEE Transactions on Antennas and Propagation*, Vol. AP-18, May 1970, pp. 323-327.
- [2] E. Carpenter, "An Optimized Dual Polarization Global Beam Antenna," AIAA 9th Communications Satellite Systems Conference, San Diego, March 7-11, 1982, A Collection of Technical Papers, pp. 736-740.
- [3] J. Aasted and R. Roderer, "A Multibeam Array for Communication With Mobiles," AIAA 7th Communications Satellite Systems Conference, San Diego, April 24-27, 1978, AIAA Paper 587, A Collection of Technical Papers, pp. 400-406.

- [4] P. M. Woodward, "A Method of Calculating the Field Over a Plane Aperture Required to Produce a Given Polar Diagram," *Journal of the IEE*, Vol. 93, pt. IIIA, 1947, pp. 1554-1558.
- [5] J. Ruze, "Circular Aperture Synthesis," *IEEE Transactions on Antennas and Propagation*, Vol. AP-12, November 1964, pp. 691-694.
- [6] H. W. Ehrenspeck, "The Short Backfire Antenna," *Proceedings of the IEEE*, Vol. 53, August 1965, pp. 1138-1140.
- [7] H. W. Ehrenspeck, "A New Class of Medium-Size High-Efficiency Reflector Antennas," *IEEE Transactions on Antennas and Propagation*, Vol. AP-22, March 1974, pp. 329-332.
- [8] W. B. Davenport, Jr., and W. L. Root, *An Introduction to the Theory of Random Signals and Noise*, New York: McGraw-Hill, 1958, pp. 45-75.
- [9] M. H. Gibson and I. Thomson, "Radiation Considerations in the Design of Linear Microwave Transistor Amplifiers for Space Applications," *IEEE Transactions on Microwave Theory and Techniques*, Vol. MTT-26, No. 10, October 1978, pp. 779-788.
- [10] I. Thomson, "Effects of Ionizing Radiation on Small-Signal Microwave Bipolar Transistors," *IEEE Transactions on Electron Devices*, Vol. ED-25, No. 6, June 1978, pp. 736-741.

Shakeel Siddiqi received a B. Tech. from the Indian Institute of Technology, Kanpur, an M.S.E.E. from the Polytechnic Institute of New York, and has completed his Ph.D. course requirements. He is a Member of the Technical Staff in the Satellite Antenna Department at COMSAT Laboratories, where his principal activities involve the analysis, design, and implementation of satellite antennas and related components. He has been involved in such satellite programs as DBS and INTELSAT VI. He was also involved in the NASA 20/30-GHz antenna study. Presently, he is developing an MMC phase shifter for an active phased-array antenna. Prior to joining COMSAT in 1981, Mr. Siddiqi was with the Government Systems Division of General Instrument Corporation, where his work on ESM and ECM systems culminated in the invention of a reduced-size spiral and an extremely low-backlobe spiral antenna. He is a member of the IEEE.





*Amir I. Zaghloul received a B.Sc. from Cairo University, Egypt, in 1965, and an M.A.Sc. and Ph.D. from the University of Waterloo, Canada, in 1970 and 1973, respectively, all in electrical engineering. Prior to joining COMSAT Laboratories in 1978, he held faculty positions at the Universities of Waterloo and Toronto, in Canada; and at Aalborg University in Denmark. At COMSAT Laboratories, he has been a member of the Microwave Systems Department and the Satellite Antennas Department, where he is presently a Staff Scientist.*

*His responsibilities have included design and development of microwave integrated circuits, microwave switch matrix for SS-TDMA systems, multibeam antennas, phased-array systems, microstrip antennas, and reflector antenna systems. He has also been involved in study and support efforts for several satellite programs, including INTELSAT, INMARSAT, ARABSAT, PALAPA, and SATCOL. Dr. Zaghloul is a Senior Member of the IEEE, and is Chairman of the Washington, D.C. Chapter of the Antennas and Propagation Society for 1985-1986.*

*Su Min Chou received a B.S.E.E. from Chinese Naval College of Technology in 1954, an M.S. from Chiao Tung University in 1961, and a Ph.D. from University of Utah in 1967. He joined COMSAT Laboratories in 1968 and is presently a Senior Staff Scientist in the Microwave Technology Division. He has been involved in the design of a low-noise parametric amplifier, a high-power IMPATT amplifier, a high-power bipolar transistor amplifier, and a high-power VET amplifier at various frequency bands for both earth station and satellite applications.*



*Reuben E. Eaves received a B.E.S. from the Johns Hopkins University in 1964, and an Sc.M. and Ph.D. from Brown University in 1966 and 1969, all in electrical engineering. He was Manager of Satellite Design for INTELSAT Technical Services at COMSAT from 1981 to 1984, with responsibility for system analysis and design studies. Prior to joining COMSAT, from 1976 to 1981, Dr. Eaves was at Lincoln Laboratory, Massachusetts Institute of Technology, where he was involved in the development of advanced satellite systems and concepts.*



*From 1968 to 1976, he was at the NASA Electronics Research Center and the Transportation Systems Center, and concurrently held a visiting appointment at Brown University. He is presently with the MITRE Corporation, Bedford, MA, where he is on the Division Staff of the Strategic Communications Division.*

*Dr. Eaves is a member of Sigma Xi, Tau Beta Pi, and Eta Kappa Nu. He is an Associate Fellow of AIAA and a Senior Member of IEEE.*

# ***Fade duration statistics from Comstar 20/30-GHz beacon measurement program\****

P. N. KUMAR†

(Manuscript received April 30, 1984)

## ***Abstract***

Data on rain attenuation duration and the distribution of time intervals between rain fades for a given fade depth are important in specifying the performance of satellite communications systems. These data are especially useful for applications involving power control, diversity switching, and adaptive forward error correction in digital systems. This paper discusses the measured fade duration statistics and interval-between-fade statistics derived from 4 years of 19- and 29-GHz beacon signal measurements taken with the COMSTAR (D-1, D-2, and D-3) satellites. For fade depths between 3 and 25 dB, the mean fade duration ranged from 10 to 3.5 min. at 19 GHz and from 11 to 7 min. at 29 GHz. Seasonal and diurnal variations of these fades and their dependence on frequency and elevation angle are also reported.

## ***Introduction***

Rain attenuation can significantly affect the design of communications systems, especially at frequencies greater than 10 GHz. Annual cumulative

---

\* This paper is based on work performed at COMSAT Laboratories under the sponsorship of the Communications Satellite Corporation. Portions of this paper were presented at the International IEEE APS/URSI Symposium in Houston, Texas, May 23–26, 1983.

† P. N. Kumar is currently with the Voice of America, USIA.

distributions of rain attenuation allow a system designer to estimate fade margins based on system reliability requirements. For communications systems that are intended to compensate for rain fades through up-link/down-link power control or site diversity operation, statistics on fade duration and intervals between fades of a specified attenuation level are important. Several studies [1]–[9] have been published on the measurement results of fade duration statistics. However, questions concerning the frequency and elevation-angle dependence of these effects remain unanswered.

In this paper, these questions are addressed in two formulations—the frequency of occurrence of fades and the duration of fades. The approximate frequency and elevation angle dependence of the fades are also presented. These results are based entirely on data from the COMSTAR D-1, D-2, and D-3 beacon measurement programs at Clarksburg, Maryland [7]. Although these results may not pertain to all cases, they do bring out some important similarities between the ratios of attenuations at two frequencies and the ratios of the number of fades at a given attenuation level. The dependence of the number of fades on elevation angle is similar to that for the ratio of attenuations. Data on the distribution of intervals between fades are also provided. Statistics on both short fade intervals, which occur during an event, and long fade intervals, which occur between two isolated rain events, are presented separately; applications of these statistics are also briefly discussed.

### Data collection

The measured data consist of attenuation statistics at 19.04 GHz for nominally vertical and horizontal polarization, as well as attenuation statistics for nominally vertical polarization at 28.56 GHz. The transmitting sources were beacons on the COMSTAR D-1 (128°W), D-2 (95°W), and D-3 (87°W) satellites. Elevation angles from the receiving antenna to these three satellites were 21°, 41°, and 43.5°, respectively. (A detailed description of the measurement equipment and the COMSTAR satellite parameters is given in Reference 7.)

### Data reduction and analysis

Signal level data collected on paper charts were digitized at approximate inflection points by an operator and stored on magnetic tape for data analysis. These data were computer-interpolated to obtain 1-min. samples of attenuation. Signal attenuations were always referenced to the clear-sky level (see the unperturbed trace in Figure 1). This process at least partially eliminates some extraneous receiver contributions resulting from nonprecipitation effects

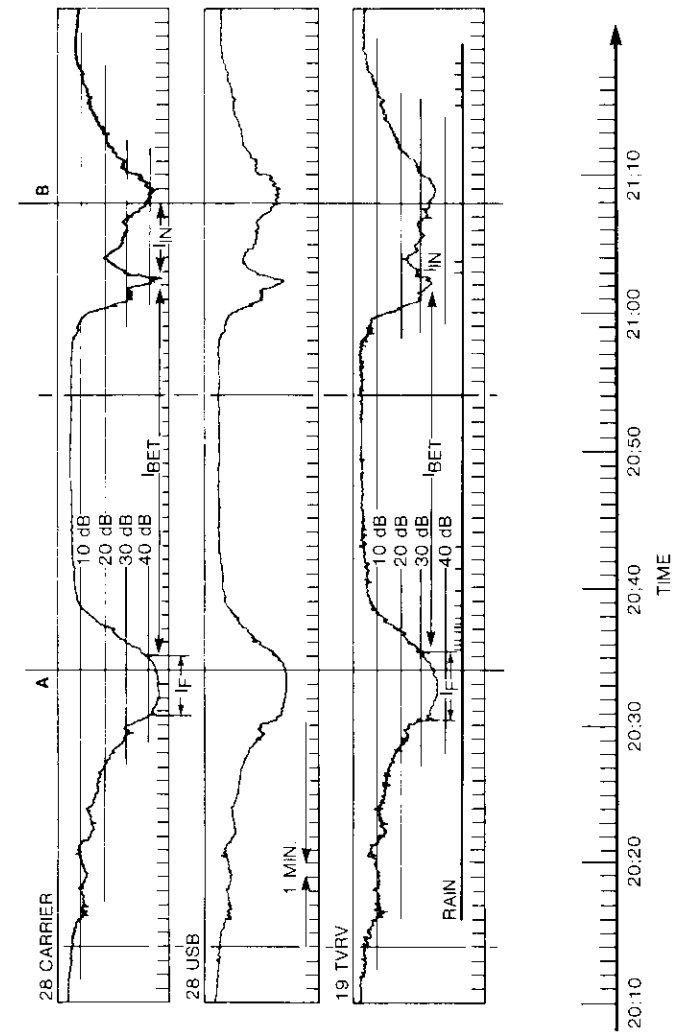


Figure 1. Rain Events A and B for June 28, 1977

such as clear-sky absorption and those resulting from antenna sidelobes.

Figure 1 represents a sample recording of 19- and 29-GHz signal attenuations measured during a summer rainstorm that occurred on June 28, 1977. Attenuation exceeding 35 dB was observed. Levels of 10, 20, 30, and 40 dB are shown in Figure 1. An attenuation "event" is defined as any time interval for which the signal level is less than the nominal clear-sky value. Figure 1 gives examples of two isolated events, A and B. A "fade" duration ( $I_f$ ) is the time interval over which the attenuation continuously exceeds a specified attenuation threshold, which may occur several times within a particular event. An "intra-event interval" ( $I_{IN}$ ) is the time interval during an event (such as event B in Figure 1) when the attenuation is less than a given attenuation threshold.  $I_{IN}$  is an example of an interval within an event. An "inter-event interval" is the time interval between two events for which the attenuation is less than a given threshold. The designation  $I_{BET}$  indicates an interval *between* events. These are long time intervals on the order of hours (or days), depending on the fade depth of interest. Intervals within an event are short compared to intervals between events, and are typically minutes, not hours, long.

It is interesting to note in Figure 1 that intra-event intervals can be clearly identified in event B, but not so clearly in event A. The observed point rain rate was more intense (note the closely-spaced rain ticks) during event A than during event B. By analyzing such events, it can be shown that intra-event intervals may be related to the nature and intensity of the rain. All attenuation events were included in the data analyses: data were computer-processed to obtain cumulative annual fade statistics for a given fade threshold.

## Results

Figure 2 shows the fade duration histograms for 19-GHz horizontal polarization at a  $21^\circ$  elevation angle for 3, 6, 10, 14, 20, and 25 dB attenuation levels. Previous results [7] have shown that the measured attenuation in general was about 1 to 2 dB higher for the horizontally polarized 19-GHz signal than for the vertically polarized signal. Figure 3 shows similar distributions for the 29-GHz vertical polarization.

These curves show the number of events per year with fade duration equal to or greater than that specified on the abscissa. The intersection of these curves with the ordinate yields an annual total of the number of fades (with a time resolution of 1 min.) at that fade depth. A comparison of Figures 2 and 3 reveals that the number of fades at 29 GHz exceeds the number at 19 GHz by a factor of about 2. Figure 4 shows the distribution of 19-GHz fades for an elevation angle of  $41^\circ$ . Figures 2 and 4 indicate that at the lower

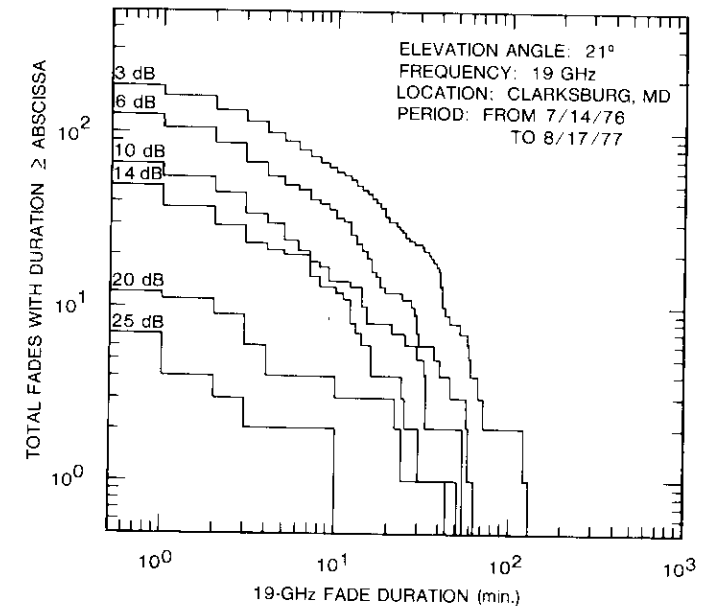


Figure 2. 19-GHz Fade Duration Distributions

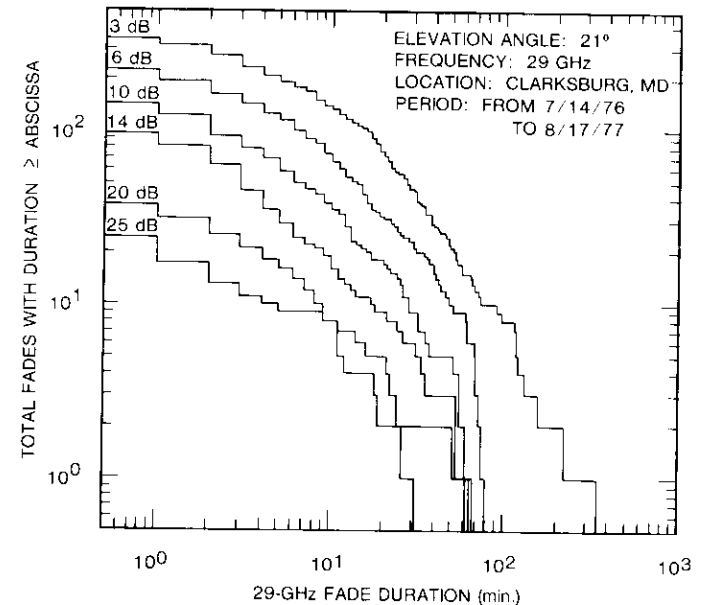


Figure 3. 29-GHz Fade Duration Distributions

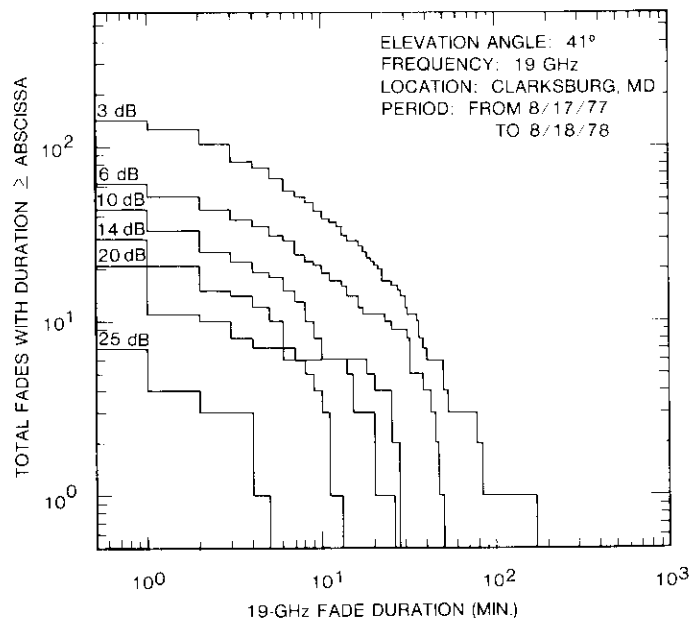


Figure 4. 19-GHz Fade Duration Distributions

elevation angle (21°), the number of observed fades was about twice the number observed at the higher elevation angle (41°).

Tables 1, 2, and 3 present fade duration data with a fraction of total fading

TABLE 1. ANNUAL ATTENUATION DURATION STATISTICS\*

FADE DURATION (min.)	FRACTION OF TOTAL FADING TIME (%) ACROSS FADE LEVELS					
	3 dB	6 dB	10 dB	15 dB	20 dB	25 dB
>3	95.7	91.9	91.1	93.6	91.2	89.7
>10	81.6	72.4	69.7	71.4	85.6	78.4
>30	53.8	29.0	39.6	17.0	38.1	—
>60	17.5	6.1	—	—	—	—
Total Fading Time (min.)	2,196	1,024	514	297	114	24
Total Number of Fades	183	125	66	43	12	7

\* Frequency: 19.04 GHz (horizontal polarization)  
Elevation Angle: 21°  
Time Period: July 1976 to August 1977  
Location: Clarksburg, Maryland

TABLE 2. ANNUAL ATTENUATION DURATION STATISTICS\*

FADE DURATION (min.)	FRACTION OF TOTAL FADING TIME (%) ACROSS FADE LEVELS					
	3 dB	6 dB	10 dB	15 dB	20 dB	25 dB
>3	96.9	95.6	92.6	89.3	93.1	91.1
>10	86.1	76.2	71.6	68.9	69.6	81.2
>30	68.7	56.0	35.4	40.2	35.4	18.3
>60	57.1	45.5	5.6	11.0	19.6	—
Total Fading Time (min.)	5,366	2,391	1,188	511	310	167
Total Number of Fades	333	220	141	79	37	24

\* Frequency: 28.56 GHz (vertical polarization)  
Elevation Angle: 21°  
Time Period: July 1976 to August 1977  
Location: Clarksburg, Maryland

TABLE 3. ANNUAL ATTENUATION DURATION STATISTICS\*

FADE DURATION (min.)	FRACTION OF TOTAL FADING TIME (%) ACROSS FADE LEVELS					
	3 dB	6 dB	10 dB	15 dB	20 dB	25 dB
>3	93.7	95.1	90.2	88.0	88.5	83.3
>10	76.9	77.2	52.3	69.7	42.8	—
>30	45.5	53.3	—	—	—	—
>60	21.7	—	—	—	—	—
Total Fading Time (min.)	1,530	645	272	143	77	13
Total Number of Fades	141	62	44	26	21	7

\* Frequency: 19.04 GHz (horizontal polarization)  
Elevation Angle: 41°  
Time Period: August 1977 to August 1978  
Location: Clarksburg, Maryland

time at a given fade level for the 19- and 29-GHz data presented in Figures 2, 3, and 4, respectively. These data are most useful to system designers in determining over what percentage of time a particular fade depth occurs and its corresponding duration probability.

**Frequency and elevation angle dependence**

Based on the measured results, four simple ratios are computed for each attenuation threshold (or fade depth) to study the frequency and elevation angle dependence. One general assumption in this study is that the attenuation data obtained at the 21° elevation angle (D-1 measurement, July 1976 through

August 1977) are comparable to those collected at a 41° elevation angle (D-2 measurement, August 1977 through August 1978). This assumption gains support from the annual rainfall data, which compare favorably [7]. However, since some year-to-year variability in rain effects can be expected, several years of measured data for both elevation angles would be required to accurately characterize year-to-year variability. The elevation angle for the D-3 measurement (43.5°) was close to that of the D-2 measurement (41°), and the annual attenuation statistics (for purposes of this paper) were comparable. Therefore, data from D-1 (21°) and D-2 (41°) are presented here, with occasional references to D-3 data.

#### Frequency dependence

Let  $R_{1f}$  and  $R_{2f}$  be defined as

$$R_{1f} = \frac{\text{Total no. of fades with } A > x \text{ dB at } f_2}{\text{Total no. of fades with } A > x \text{ dB at } f_1} \quad (1)$$

$$R_{2f} = \frac{\text{Total fading time for } A > x \text{ dB at } f_2}{\text{Total fading time for } A > x \text{ dB at } f_1} \quad (2)$$

for a fixed elevation angle. Figure 5 plots these ratios for  $f_2 = 29$  GHz and  $f_1 = 19$  GHz as a function of fade depth. These curves show that for a given elevation angle, the total number of fades and the total fading time increased by a factor of about two as the frequency increased from 19 to 29 GHz. For these data, it appears that

$$R_{1f} \approx \frac{f_2^2}{f_1^2} \quad (3)$$

$$R_{2f} \approx \frac{f_2^2}{f_1^2} \quad (4)$$

which is similar to the behavior of ratios of rain attenuations observed at these frequencies [6], [10].

#### Elevation angle dependence

Similarly,  $R_{1E}$  and  $R_{2E}$  are defined as

$$R_{1E} = \frac{\text{Total no. of fades with } A > x \text{ dB at } \theta_1}{\text{Total no. of fades with } A > x \text{ dB at } \theta_2} \quad (5)$$

$$R_{2E} = \frac{\text{Total fading time for } A > x \text{ dB at } \theta_1}{\text{Total fading time for } A > x \text{ dB at } \theta_2} \quad (6)$$

for a fixed frequency. Figure 6 plots these ratios as a function of fade depth for 19 and 29 GHz. These curves show that for a given frequency, as the path elevation angle decreased from 41° to 21°, the total number of fades and the total fading time increased by a factor of roughly 1.8.

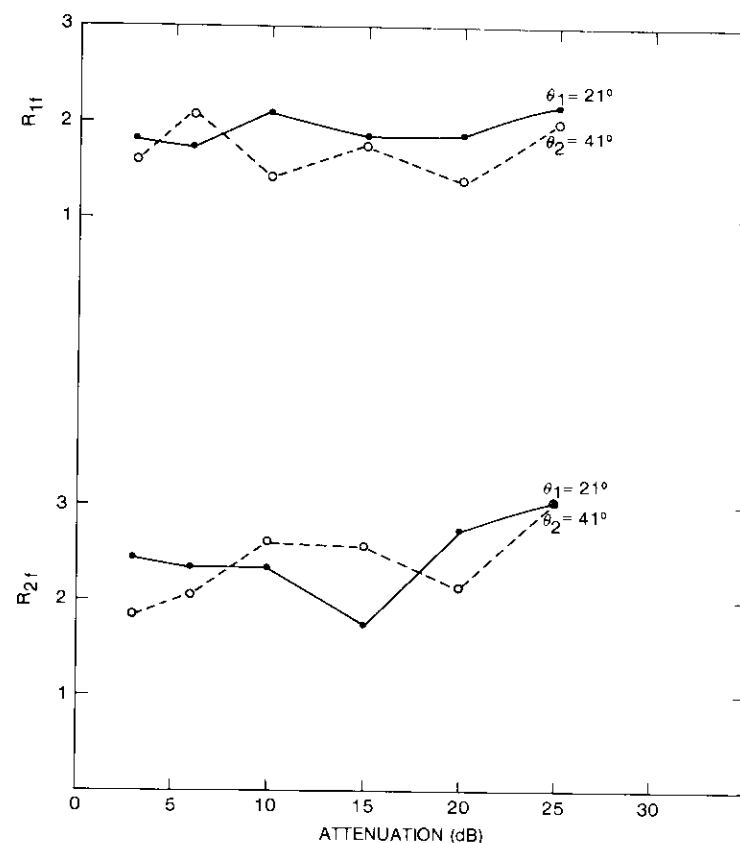


Figure 5. Ratios  $R_{1f}$ ,  $R_{2f}$  as a Function of Fade Depth

These results are at least approximately consistent with the cosecant law [10] for the scaling of attenuation statistics as a function of elevation angle:

$$R_{1E} \approx \frac{\sin \theta_2}{\sin \theta_1} \tag{7}$$

$$R_{2E} \approx \frac{\sin \theta_2}{\sin \theta_1} \tag{8}$$

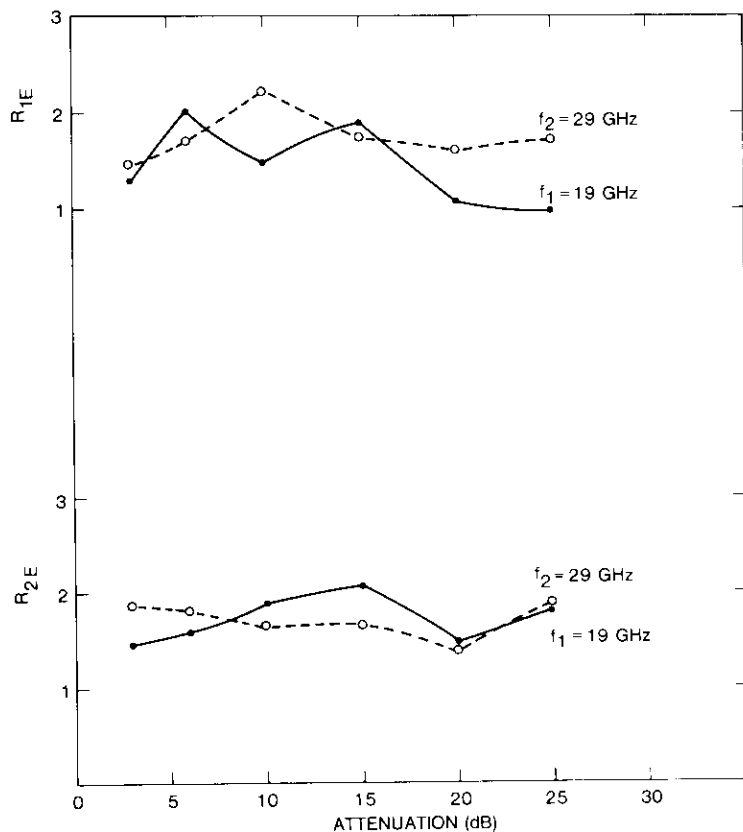


Figure 6. Ratios  $R_{1E}$ ,  $R_{2E}$  as a Function of Fade Depth

Figure 7 shows the variation of mean fade duration as a function of fade depth for 19- and 29-GHz signals at 21° and 43.5° elevation angles. A general trend of decreasing mean fade duration with increasing elevation angle can be observed in the figure. Some variation in the data for 21° may be the result of a few heavy rain events that occurred during the measurement period.

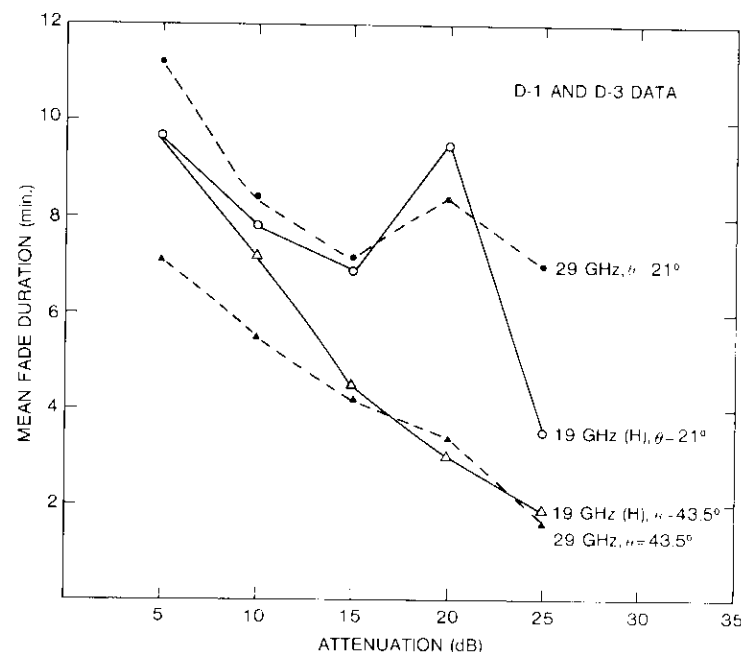


Figure 7. Mean Fade Duration as a Function of Fade Depth and Elevation Angle

**Seasonal and diurnal variations**

Figure 8 shows a plot of the total number of fades per year as a function of fade depth. Each data point represents the total number of fades that exceeded a given attenuation threshold, divided by the corresponding cumulative fading time expressed as a fraction of a year. The number of fades observed for each season is normalized to an annual basis. Over a full year, the number of fades ranged from 270 at the 5-dB level to 16 at the 30-dB level. During winter, fall, and spring, the rate of occurrence of higher attenuation fades was less than that for a full year. The rate of occurrence of fades at all levels was higher in the summer than for the entire year (see Figure 8). Fades exceeding the 20-dB level occurred two to three times more frequently over the summer than during the other three seasons. (A similar observation was made for the other two years of data not shown in Figure 8.)

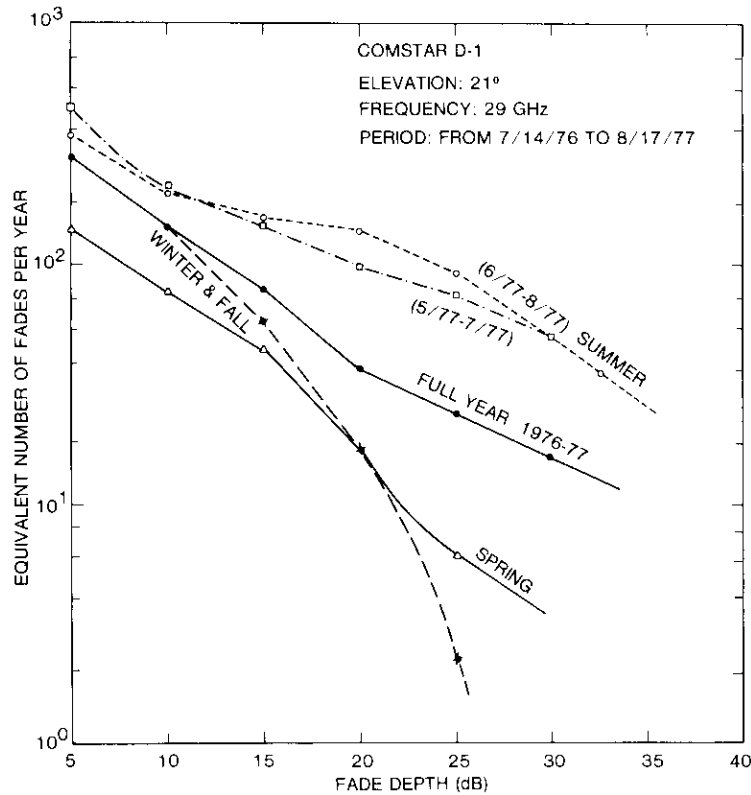


Figure 8. Seasonal Variation in the Frequency of Occurrence of Fades

Diurnal distributions of fading reveal the time of day during which fades of a given threshold were observed. For example, Figure 9 shows the 29-GHz diurnal distributions for 10-, 14-, and 20-dB attenuation levels from the COMSTAR D-1 data. Most attenuations greater than 20 dB (see legend in Figure 9) occurred during the interval from 1200 to 2000 hr local time. The ordinate represents the cumulative fading time (in minutes) over the year that the attenuation exceeded a specified level. Figure 10 shows a similar distribution for data collected during June, July, and August. A careful comparison of Figures 9 and 10 reveals that about 95 percent of the cumulative fading time during that year for attenuations exceeding 20 dB occurred during the summer months.

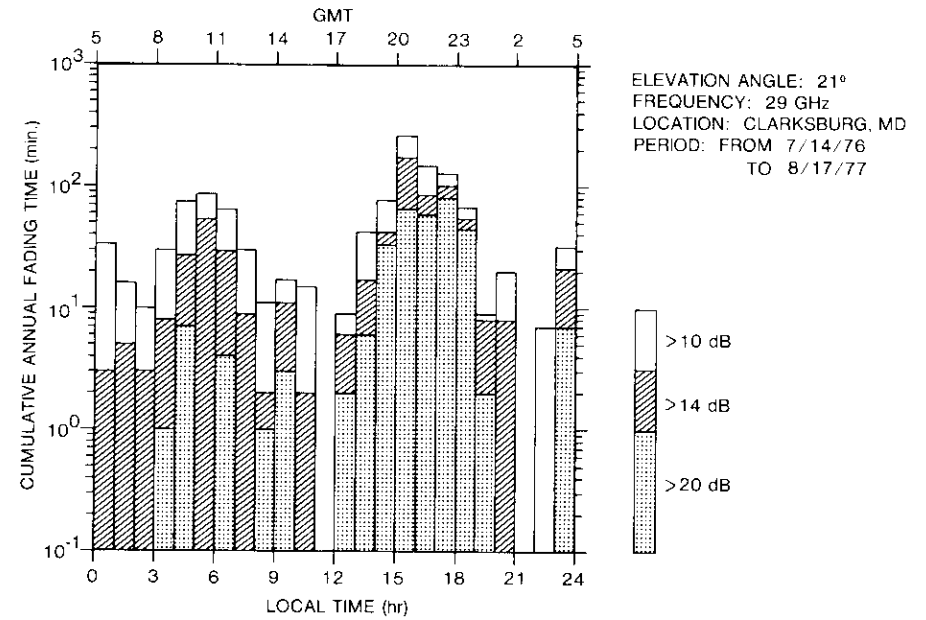


Figure 9. Diurnal Distribution of 29-GHz Fades for the Full Year

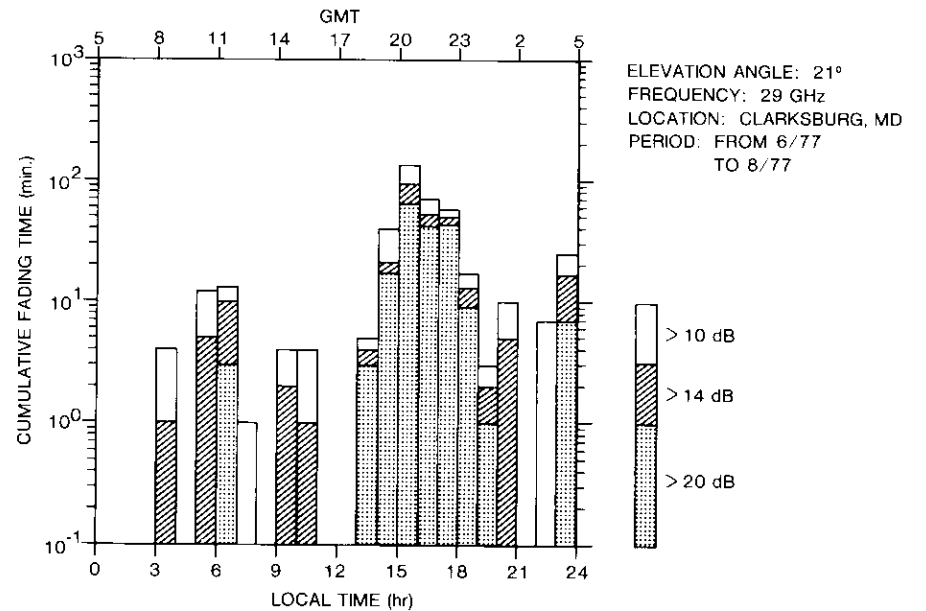


Figure 10. Diurnal Distribution of 29-GHz Fades for the Summer Months

**Inter-event and intra-event interval statistics**

Figure 11 gives the distributions of inter-event intervals for fades exceeding 5, 10, and 20 dB, as observed during the 1976 to 1977 measurement period. Higher attenuation fades are separated by several hours. For example, 17 out of the 19 10-dB fades observed were separated by more than 2 hr. All of the 20-dB fades were separated by more than 2 hr. It is likely that such distributions may change significantly from year to year, depending on the time of occurrence of thunderstorms. Figure 12 gives the distributions of intra-event intervals. Twenty-nine out of the 32 10-dB fades had intra-event intervals in excess of 2 min. These data should be very useful in system engineering applications such as site diversity and power control.

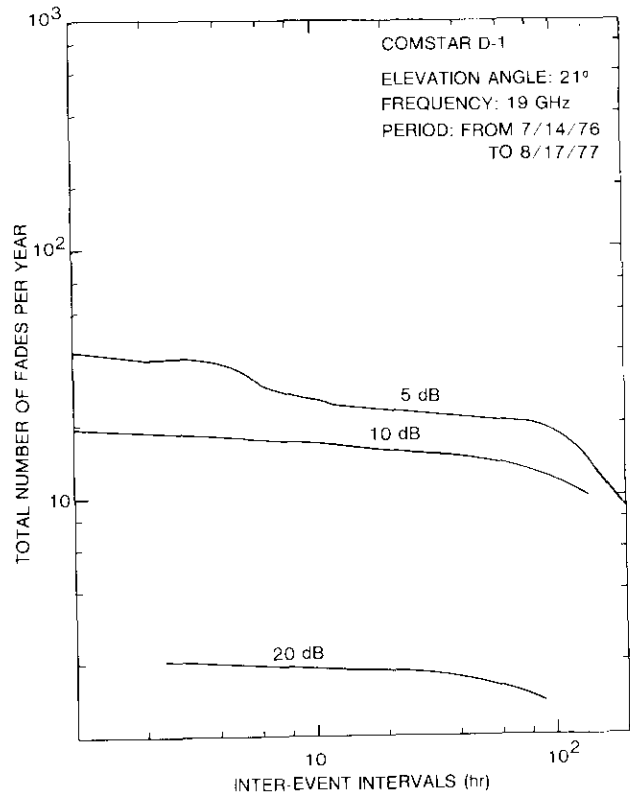


Figure 11. Distribution of Inter-Event Intervals

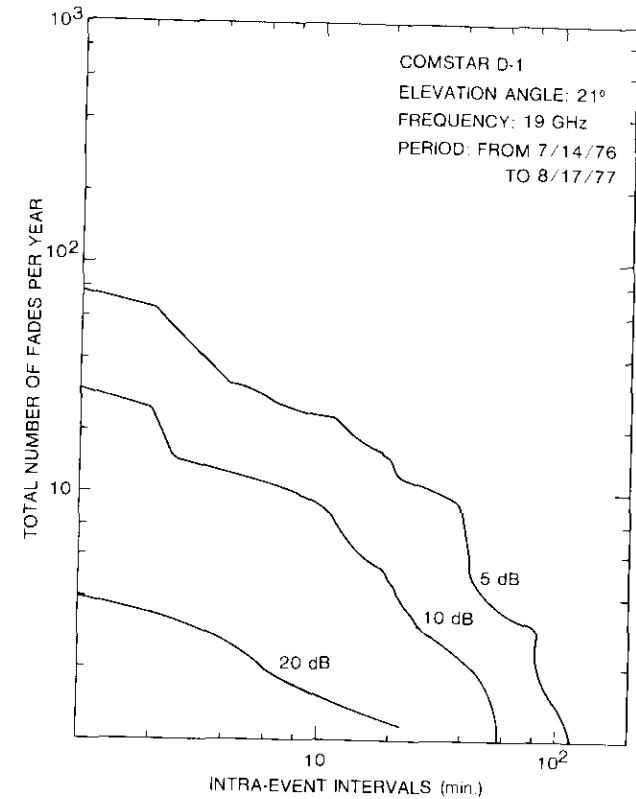


Figure 12. Distribution of Intra-Event Intervals

**Conclusions**

The dependence of rain fade duration on elevation angle and frequency has been investigated for data collected at Clarksburg, Maryland. The ratios of the total number of fades and their durations for two frequencies at a given fade depth were quite similar to the ratios of attenuation. The ratios of the total number of fades and their durations for different path elevation angles were also similar to the ratios of attenuation. The mean fade duration appeared to depend on both frequency and elevation angle. For these measured data, at a given frequency, the mean fade duration decreased with increasing path elevation angle. The occurrence of higher attenuation fades was found to be two to three times greater in June, July, and August than during the rest of the year. Ninety-five percent of the higher attenuation events (>20 dB) in a year occurred in the summer.

## Acknowledgments

Special thanks are due to D. V. Rogers for a critical review of the manuscript. Thanks are also due to D. J. Fang and C. Mahle for their useful comments. G. Hyde supervised the experiment and data collection. P. Ackermann, N. Nguyen, and C. Zaks provided hardware support, maintenance, and day-to-day operation of the receiver. K. Yeh, O. Piontek, and P. Fritz reduced, rechecked, and made computer runs for all the data. Thanks are also due to L. Pollack for his interest in supporting this work.

## References

- [1] F. M. Galante, "Statistical Evaluation of Rain Fades and Fade Durations at 11 GHz in the European Region," International Conference on Satellite Communications Systems Technology, London, England, April 7-10, 1975, *Proceedings*, IEE Conference Publication 126, pp. 302-307.
- [2] G. Brussaard, "Attenuation Due to Rain on a Slant Path," *Alta Frequenza*, Vol. XLVII, No. 4, 1979, pp. 104-108.
- [3] E. Matricciani, "Duration of Rain Induced Fades of the Signal from the SIRIO at 11.6 GHz," *Electronics Letters*, Vol. 17, No. 1, 1981, pp. 29-30.
- [4] S. H. Lin, H. J. Bergmann, and M. V. Pursley, "Rain Attenuation on Earth-Satellite Paths—Summary of 10-Year Experiments and Studies," *Bell System Technical Journal*, Vol. 59, No. 2, February 1981, pp. 183-228.
- [5] D. V. Rogers, "Diversity and Single-Site Radiometric Measurements of 12-GHz Rain Attenuation in Different Climates," IEE Conference Publication No. 195, Vol. 2, 1981, pp. 118-123.
- [6] H. W. Arnold, D. C. Cox, and H. H. Hoffman, "Fade Duration and Interfade Interval Statistics Measured on a 19-GHz, Earth-Space Path," *IEEE Transactions on Communications*, Vol. COM-30, No. 1, January 1982, pp. 265-269.
- [7] P. N. Kumar, "Precipitation Fade Statistics for 19/29-GHz COMSTAR Beacon Signals and 12-GHz Radiometric Measurements," *COMSAT Technical Review*, Vol. 12, No. 1, Spring 1982, pp. 1-27.
- [8] W. J. Vogcl, "Measurements of Satellite Beacon Attenuation at 11.7, 19.04, and 28.56 GHz and Radiometric Site Diversity at 13.6 GHz," *Radio Science*, Vol. 17, No. 6, November-December 1982, pp. 1511-1520.
- [9] International Radio Consultative Committee (CCIR), "Propagation Data Required for Space Telecommunications Systems," Report 564-2, Recommendations and Reports of the CCIR XVth Plenary Assembly, Vol. 5, 1982, pp. 331-373.
- [10] D. C. Cox and H. W. Arnold, "Results from the 19- and 28-GHz COMSTAR Satellite Propagation Experiments at Crawford Hill," *Proceedings of the IEEE*, Vol. 70, No. 5, May 1982, pp. 458-488.

Prabha N. Kumar received a B.S. and an M.S. from Bangalore University, India, in 1968 and 1970; and a Ph.D. in applied physics from Southern Illinois University in 1976. From 1970 to 1972, she was a Senior Research Fellow in Modulated Surface Wave Structures at the Microwave Laboratory of the Indian Institute of Science, Bangalore. She was with Computer Sciences Corporation between 1977 and 1979, where she worked on laser reflector arrays. Dr. Kumar joined COMSAT Laboratories in 1979. From 1979 to 1984, she worked on various research projects to study the effects of precipitation on satellite signals for frequencies greater than 10 GHz and on the design analyses of a laser optical rain gauge. Dr. Kumar is currently with the Voice of America (VOA), Advanced Concepts and Plans Division of Systems Engineering Directorate. Her present responsibilities include monitoring contractual activities and coordinating in-house studies involving various system concepts related to the VOA modernization program. Dr. Kumar received the NASA recognition award for her work on laser reflectors in 1981. She is a member of IEEE and CCIR U.S. Study Groups 5 and 9.



# ***A field test for companded single sideband modulation: implications for capacity enhancement and transmission planning***

E. WALLACE, C. ADAMS, AND D. ARNSTEIN

(Manuscript received November 15, 1984)

## ***Abstract***

Late in 1983, AT&T and the Deutsche Bundespost (DBP) of the Federal Republic of Germany conducted a field test of companded single sideband (CSSB) modulation in a test carrying live traffic between the U.S. and Germany over the INTELSAT system. This paper describes the planning, conduct, and results of that test as well as the implications for transmission planning and future capacity with the CSSB technique. A 12-channel circuit group was tested between the AT&T switch in Pittsburgh, Pennsylvania, and the DBP switch in Frankfurt, Germany, via the Etam and Raisting satellite earth stations. A transponder bank that included existing FDM/FM carriers was chosen to match typical INTELSAT operating conditions, permitting the compatibility of FDM/FM and CSSB to be examined. Results of the objective performance tests are discussed, along with a description of the subjective testing methods used by AT&T and the DBP. Subjective testing rates CSSB as equal in quality to CFM and FDM/FM. Error rate measurements show its data-handling capability is adequate for a 4,800-bit/s VIF modem.

Results of voice level tests performed by AT&T at its New York switch are also introduced, and based on those measured values, this paper also provides a discussion of achievable transponder capacity and the variables affecting that capacity. Transmission planning for the field trial, which took into account existing traffic on other carriers, is also discussed.

## Introduction

From September to December 1983, the DBP, AT&T, and COMSAT conducted a field test of CSSB on operational circuits of the public switched telephone network (PSTN) between international switching centers (ISCs) at Frankfurt and Pittsburgh. Currently, AT&T operates CSSB on a COMSTAR satellite for commercial U.S. domestic service between New York City and San Francisco. Companded FM (CFM) is operational in the INTELSAT system on the PSTN and on private line circuits between Etam and Grand Cayman earth stations via an INTELSAT V satellite, with companders installed at the earth stations. Companders for CSSB circuits at the ISCs would reduce the effect of noise occurring in terrestrial links between the earth station (ES) and the ISC.

To remove a test bias that could consequently occur in favor of CSSB, it was considered desirable to also test the AT&T companded circuits over an FM link. At the conclusion of the CSSB test, therefore, the same 12-channel group was transmitted on a 2.5-MHz FM carrier, closely following the line-up procedures for a standard INTELSAT CFM carrier. Details of the line-up criteria for each test are given below. Subjective testing, which was identical for both trials, included side-by-side comparison with noncompanded FDM/FM circuits.

AT&T and the DBP established terrestrial links between their respective ISCs and the earth stations. To ensure compatibility with the unique baseband configuration created by the AT&T single-sideband modulation equipment, COMSAT, along with the DBP and INTELSAT, established the satellite path parameters and carrier size. In coordination with COMSAT and the DBP, AT&T established the single-sideband equipment configurations in the earth stations, as well as the echo canceller and compander configurations in the ISCs.

AT&T also provided echo cancellers and companders for the switches in Frankfurt and in Pittsburgh. In Frankfurt, echo cancellers were installed on the line side of the CCITT No. 5 signaling units (identified as No. 5 SIGNALING or No. 5 SIG in the figures that follow) and were disabled during signaling. In Pittsburgh, echo cancellers were installed on the drop side of the CCITT No. 5 signaling units. The companders, with 2:1 compression ratios and  $-16$  dBm0 unaffected signal power, were installed on the line side of the echo cancellers and signaling units in both Frankfurt and Pittsburgh.

At the conclusion of the test, a joint report was issued by the U.S. and German Signatories to the INTELSAT Board of Governors Technical Committee. This paper draws on the technical content of that report and goes beyond it to elaborate on transmission planning and capacity implications for the widespread use of CSSB within the INTELSAT system.

## Purpose of field test

Of primary importance in establishing the acceptability of CSSB on INTELSAT satellites was the subjective performance quality as perceived by the user. However, objective measurements were also taken, and based on the measured parameters, an analysis was conducted.

The field test was designed to accomplish the following:

- Demonstrate the feasibility of incorporating companders at ISCs.
- Demonstrate the feasibility of incorporating single-sideband equipment at INTELSAT earth stations.
- Compare satellite voice circuits using CSSB modulation with conventional FM as well as CFM.
- Establish that CSSB modulation can provide satisfactory voice and voiceband data circuit performance in the current INTELSAT environment.

## Equipment configuration

The complement of equipment needed to add a CSSB-modulated voice group is discussed next. It consists simply of companders at the international switch along with master group and multimaster group translators at the earth station. Installation and checkout were conducted in about 1 week.

Test circuit installation configurations for the Pittsburgh and Frankfurt companders and echo cancellers are shown in Figures 1 and 2. The single-

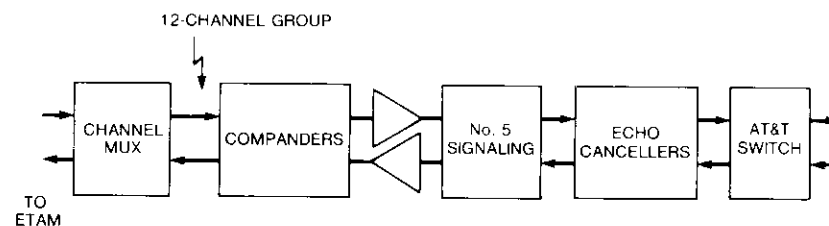


Figure 1. CSSB/CFM Equipment Configuration at AT&T Pittsburgh Switching Facility

sideband equipment installation at the earth stations is shown in Figure 3. At Etam, the single-sideband equipment, which was installed in the AT&T area, transmitted the signal to COMSAT at IF. The IF frequency plan is shown in Figure 4. Because of equipment limitations, the output of the single-sideband equipment is 5 MHz below the standard INTELSAT IF of 70 MHz,

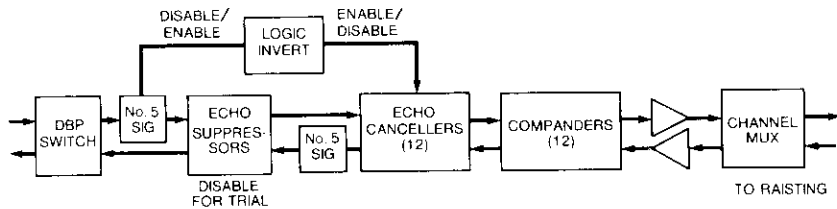


Figure 2. CSSB/CFM Equipment Configuration at DBP Frankfurt Switching Facility

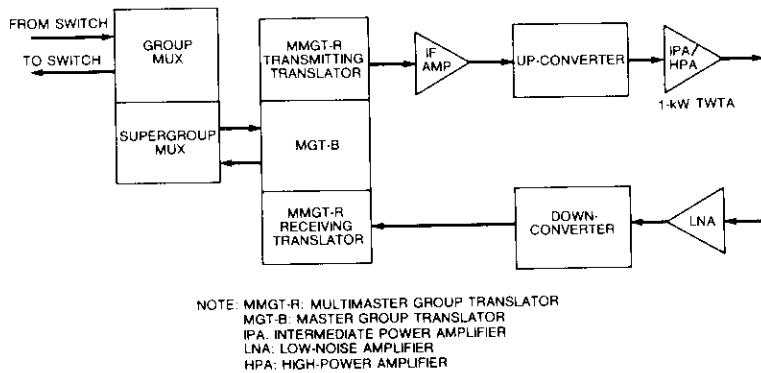


Figure 3. Earth Station Equipment Configuration for CSSB Test

instead of centered on it. Figure 5 shows the equipment configuration for the CFM test.

**Satellite link and transmission analysis methodology**

The operational test was conducted over the Atlantic Ocean Region (Major Path 2), using INTELSAT V (F-6). The transponder selected was chosen to provide a nominal INTELSAT operating environment for the CSSB channels, which typically means encountering two or three co-channel interference sources as well as multicarrier operation of the transponder. Additionally, sufficient bandwidth was required to accommodate either the CSSB or CFM control test channels. Table 1 gives the measured satellite and earth station parameters applicable to this test. (In the tables that follow, *G/T* = ratio of

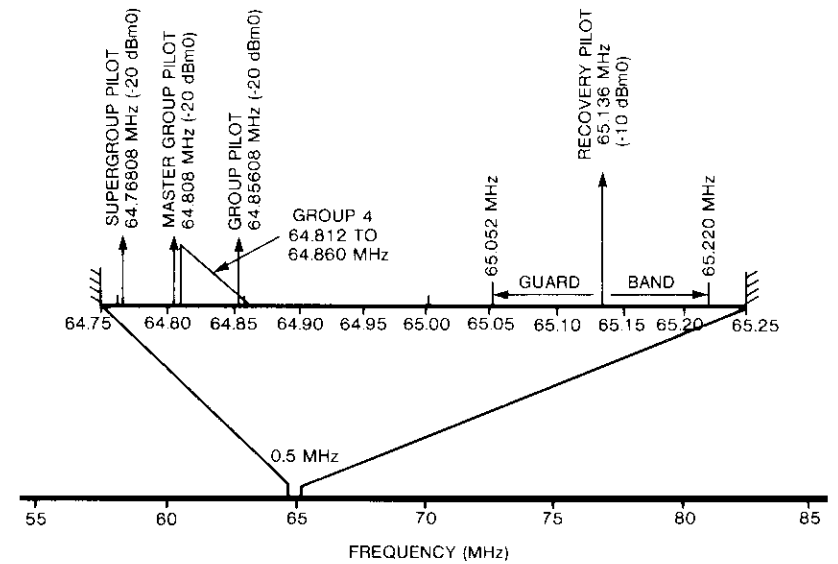


Figure 4. IF Frequency Plan

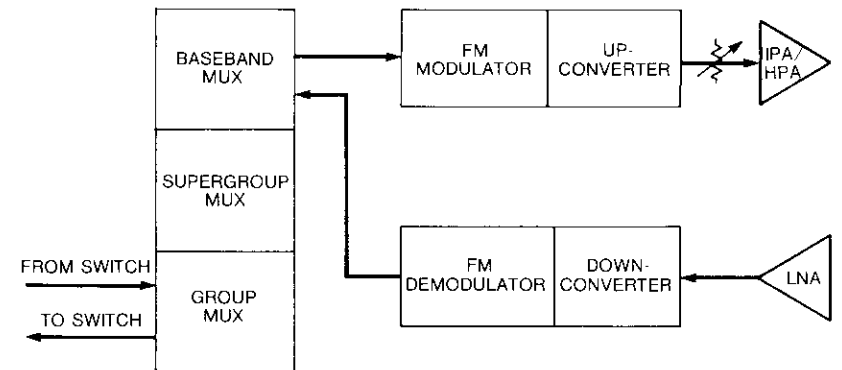


Figure 5. Earth Station Equipment Diagram for CFM Test

gain-to-noise temperature; *SFD* = saturation flux density; e.i.r.p. = equivalent isotropically radiated power.)

The specific frequencies used for the CSSB test were selected by COMSAT and INTELSAT. INTELSAT provided the FDM/FM frequency plan of the transponder bank and the power levels of the FDM/FM carriers. The CSSB frequencies were chosen to operate at least 1 MHz away from the center

TABLE 1. MEASURED SATELLITE AND EARTH STATION PARAMETERS

PARAMETER	TRANSPONDER 13	TRANSPONDER 53
Satellite e.i.r.p.	32.5 dBW	31.6 dBW
Satellite SFD	-72.2 dBW/m <sup>2</sup>	-69.8 dBW/m <sup>2</sup>
Satellite G/T	-3.6 dB/K	-2.4 dB/K
Earth Station G/T	41.6 dB/K	42.9 dB/K

frequency of any co-channel FM carrier to avoid the highest interference power density. Another frequency selection criterion was that intermodulation noise be set at levels low enough to achieve the required total signal-to-total noise,  $S/(N + I)$ , for the CSSB channels. Figure 6 shows the transponder frequency plan. Note that the transponder plan meets the condition that CSSB be tested in a nominal "fully loaded" configuration of FDM/FM carriers.

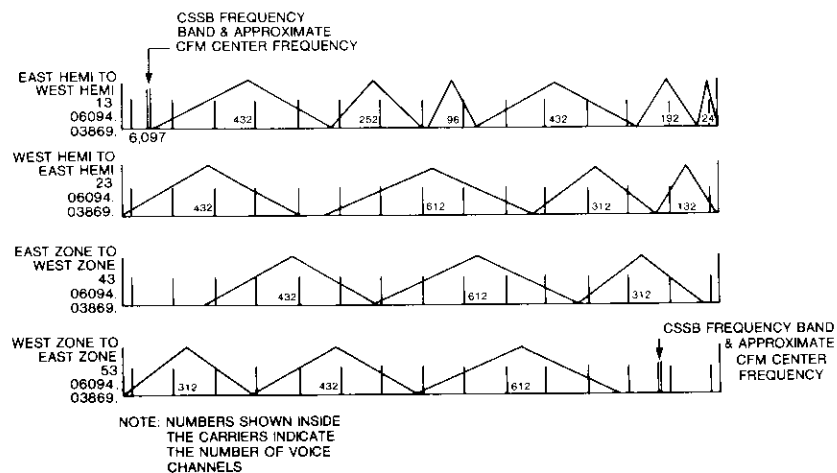


Figure 6. Transponder Frequency Plan

INTELSAT also analyzed the frequencies and power levels chosen by COMSAT to ensure that CSSB transmissions would not degrade the performance of FM carriers, either in the transponders carrying CSSB or those co-frequency with CSSB.

Transmission parameters for the recovery pilot were estimated before the field trial to achieve an  $S/(N + I)$  of 29 dB for the -10 dBm0 recovery

pilot in a 3.1-KHz bandwidth. These estimates were obtained by an iterative process, as explained below.

First, up-link and down-link powers were estimated (assuming thermal noise only) by working backward to find the required transmit e.i.r.p. of the pilot tone that would result in the desired signal-to-noise ratio ( $S/N$ ). Next, a transmission analysis computer program that optimizes voice channel quality in an FDM/FM transponder bank was used by INTELSAT to determine the power levels of the FM carriers. These power levels were used to estimate interference power from FM carriers that would be cofrequency with the CSSB recovery pilot. Signal-to-co-channel interference ratios were then determined, and signal-to-intermodulation noise was estimated. Next, the  $S/(N + I)$  was computed. If it was not equal to the required value of 29.0 dB, the computed CSSB carrier power was adjusted, and the process was repeated until that value was reached. The final recovery pilot link budgets for Etam to Raisting (transponder 13) and Raisting to Etam (transponder 53) are given in Table 2.

TABLE 2. RECOVERY PILOT LINK BUDGET

PARAMETER	TRANSPONDER 53	TRANSPONDER 13
Up-Link Frequency	6,158.645 MHz	6,097.136 MHz
Up-Link e.i.r.p.	48.9 dBW	46.1 dBW
Boltzmann's Constant	228.6 dB/K-Hz	228.6 dB/K-Hz
Satellite G/T	-2.4 dB/K	-3.6 dB/K
Satellite SFD	-69.8 dBW/m <sup>2</sup>	-72.2 dBW/m <sup>2</sup>
Up-Link Free-Space Path Loss	200.6 dB	200.1 dB
Miscellaneous Up-Link Loss	0.5 dB	0.5 dB
Up-Link S/N (thermal)	39.1 dB	35.6 dB
Up-Link S/Interference (co-channel)	40.5 dB	41.3 dB
Up-Link S/(N + I)	36.7 dB	34.6 dB
Satellite Saturated e.i.r.p.	31.6 dBW	32.5 dBW
Output Backoff	39.2 dB	39.1 dB
Down-Link Free-Space Path Loss	196.2 dB	196.6 dB
Miscellaneous Down-Link Loss	0.5 dB	0.5 dB
Earth Station G/T	42.9 dB/K	41.6 dB/K
Noise Bandwidth	34.9 dB-Hz	34.9 dB-Hz
Down-Link S/N (thermal)	32.3 dB	31.6 dB
Down-Link S/Interference (co-channel)	38.8 dB	42.4 dB
S/Intermodulation	34.9 dB	38.0 dB
Down-Link S/(N + I)	29.8 dB	30.4 dB
S/(N + I) Total	29.0 dB	29.0 dB

The CFM carriers were standard 24-channel, 2.5-MHz carriers with only the 12-channel companded group actively loaded in each carrier. The normal spreading waveform was used on the carrier, which had a required carrier-to-total noise of 12.2 dB.

Operational up-link and down-link e.i.r.p. measurements for the FDM/FM carriers and CSSB recovery pilots in transponders 13 and 53 were made by the INTELSAT Communications Systems Monitor (CSM) to verify the computed transmission parameters of the CSSB recovery pilot. Periodic measurements of the values were made throughout the field test to provide information on the stability of the carriers and recovery pilots. At the same time, live FDM/FM signal levels were checked by the CSM to verify that they were close to predicted levels. Although the measured and optimized levels for individual FDM/FM carriers differed by as much as 6.5 dB on the up-link, down-link levels as well as composite input and output backoffs showed close agreement (0.1 dB). The disagreement that was found in up-link levels may have been caused by the larger degree of uncertainty in the assumed earth station and satellite up-link parameters.

The output backoff required for a CSSB channel and the composite output backoff for the FDM carriers were such that the CSSB down-link power per channel was very low compared to the composite down-link power. Therefore the CSSB power had a negligible effect on the total output backoff and intermodulation spectrum. Likewise, the CFM carriers had negligible effect on total output backoff and intermodulation during the CFM portion of the test.

The down-link power of the CSSB recovery pilot was measured at  $-6.74$  dBW for transponder 13, and at  $-7.48$  dBW for transponder 53. These values compare well with the estimated values from the link budgets of  $-6.6$  dBW and  $-7.6$  dBW for transponders 13 and 53, respectively.

The close agreement between estimated and measured down-link powers of the recovery pilots provides confidence in the estimation procedure and the assumptions used.

### Objective tests

Before the subjective tests were started, objective performance measurements were taken between the ISCs on all circuits under test. These measurements included commonly measured voice channel transmission parameters as well as data channel parameters. In all cases, results of the CSSB and CFM circuit performance parameters were within an acceptable range. Following is a list of the objective tests that were conducted for the field test. Shown in parentheses are pertinent CCITT, Bell System, or other recommendations or standards for the tests.

Nominal Overall Loss (CCITT REC.M.1025)  
 Loss/Frequency Distortion (M.580, M.590)  
 Random Circuit Noise (M.580, M.1025)  
 Impulsive Noise (M.1025)  
 Phase Jitter/Hits (M.1025)  
 Group-Delay Distortion (M.1020)  
 Single Tone Interference (M.1025)  
 Frequency Error (M.1025)  
 Harmonic Distortion (M.1025)  
 Intermodulation Distortion (G.162, pp. 5.2)  
 Go-Return Crosstalk (G.134, pp. 5.2; G.151, pp. 4.2)  
 Signal to Notch Noise (IEEE P473/D3)  
 Echo Canceller Performance  
 Propagation Delay

Using standard, commercial modems, measurements were made of 4,800-bit/s voiceband data bit and block error rate performance at a  $-13$ -dBm0 precompanding level between the international switches. By adjusting the earth station drive levels downward, these measurements were made at noise levels equal to  $-41.5$ ,  $-39.5$ , and  $-37.5$  dBm0p in uncompanded voice channels. Table 3 gives the error rate measurement results. The noise level was returned to  $-41.5$  dBm0p [recovery pilot  $S/(N + I)$  equal to 29 dB] for the subjective tests.

TABLE 3. ERROR RATE MEASUREMENT RESULTS FOR 4,800-BIT/S DATA

UNWEIGHTED S/N	BIT ERROR RATE	1,000-BIT BLOCK ERROR RATE
24.5*	$2.9 \times 10^{-7}$	$8.3 \times 10^{-5}$
22.5	$1.5 \times 10^{-6}$	$6.1 \times 10^{-4}$
20.5	$1.1 \times 10^{-5}$	$4.0 \times 10^{-3}$

\* The nominal value of the uncompanded noise ( $-41.5$  dBm0p) during the subjective tests corresponds to a data S/N of 24.5 dB.

CCITT Automatic Transmission Maintenance Equipment (ATME) tests were performed each day by AT&T to check voice circuit loss, noise, and line signaling. In addition, traffic patterns were checked each day by a DBP computer to ensure uniform traffic usage of all circuits. Results of the ATME tests were used to detect equipment problems that occurred during the subjective tests and to ensure that the satellite link remained properly aligned. With the exception of a few isolated equipment failures, noise levels remained stable for the duration of the test.

**Average channel load**

When computed in relation to the noise floor, the average channel load\* determines the operating *S/N* in a 3.1-kHz bandwidth, which in turn relates to capacity. The average channel load is not an arbitrary parameter that can be set by the transmission engineer. The average load has decreased over the years as a result of improvements in the telephone system, while still yielding the required end-to-end quality.

Using a Bell digital volume meter, AT&T made a series of speech-level measurements on international satellite circuits. These included volume measurements on approximately 100 transmit and receive circuits to each of five countries. The resulting active mean power,  $V_0$ , and standard deviation,  $\sigma$ , of these measurements, adjusted to 0 dBr, are provided in Table 4. The calculated average channel load for both uncompanded ( $L$ ) and companded ( $L_c$ ) channels with an unaffected signal power (USP), sometimes called the unaffected level, of -16 dBm0 were calculated by using the techniques described below, and are listed in Table 4.

TABLE 4. SPEECH-LEVEL MEASUREMENT AND PER-CHANNEL SPEECH LOAD RESULTS

CONDITION	MEAN SPEECH LEVEL ( $V_0$ ), VOLUME UNITS	STANDARD DEVIATION ( $\sigma$ ), dB	NONCOMPANDED	COMPANDED
			PER-CHANNEL SPEECH LOAD ( $L$ ), dBm0	PER-CHANNEL SPEECH LOAD ( $L_c$ ), dBm0
Country A Receive	-19.9	5.6	-22.3	-23.0
Country A Transmit	-22.9	4.4	-26.7	-24.9
Country B Receive	-20.3	6.1	-22.0	-23.1
Country B Transmit	-23.8	5.2	-26.7	-25.1
Country C Receive	-20.7	5.9	-22.7	-23.3
Country C Transmit	-22.1	5.4	-24.7	-24.2
Country D Receive	-18.4	5.8	-20.5	-22.2
Country D Transmit	-21.6	4.4	-25.4	-24.2
Country E Receive	-18.9	6.5	-20.0	-22.2
Country E Transmit	-20.2	5.0	-23.3	-23.4
Average Receive	-19.6	6.0	-21.5	-22.8
Average Transmit	-22.1	4.9	-25.3	-24.4

The uncompanded average channel load is given by

$$L = V_0 + 0.115\sigma^2 + 10 \log (\tau) \quad \text{dBm0} \quad (1)$$

\* The term "average channel load" here refers to the long-term average speech power, which takes into account the speech activity factor,  $\tau$ .

where  $\tau$  is the mean activity factor, taken as 0.25 or -6 dB (CCITT recommended value; see also Reference 1). The  $0.115\sigma^2$  is a result of the log-normal distribution of talker volumes, and  $10 \log \tau$  accounts for long-term power. In making this computation, which converts volume units to power, AT&T assumed that the 1.4-dB conversion between syllabic volume and continuous talker power was absorbed into the activity factor of 0.25. The per-channel companded load is then given by

$$L_c = \frac{V_0}{2} + \frac{USP}{2} + \frac{0.115\sigma^2}{4} - 6.0 \quad \text{dBm0} \quad (2)$$

Note that the average channel load measured by AT&T is well below the nominal -15-dBm0 level usually assumed in the INTELSAT system in accordance with the CCITT.

The reference level for *S/N* on the link was the setting of a -10-dBm0 recovery pilot to have 29-dB *S/N* in a 3.1-KHz bandwidth. This setting ensures that at -13 dBm0, the signal will have adequate *S/N*, as shown in Table 3. Thus, a companded voice channel with average load  $X$  dBm0 will have an average *S/N* given by

$$\text{Voice Channel } S/N = 29 + 10 + X \quad \text{dB} \quad (3)$$

and an unweighted carrier-to-noise density given by

$$S/N_o = \text{Voice Channel } S/N + 10 \log (3100) \quad \text{dB-Hz} \quad (4)$$

Table 5 shows the required average *S/N* ( $S_{ave}/N$ ) and signal-to-noise density ratio ( $S_{ave}/N_o$ ) for the links given in Table 4.

TABLE 5. SUMMARY OF REQUIRED *S/N* FOR SPEECH

CONDITION	REQUIRED $S_{ave}/N$ (dB)	REQUIRED $S_{ave}/N_o$ (dB-Hz)
Country A Receive	16.0	50.9
Country A Transmit	14.1	49.0
Country B Receive	15.9	50.8
Country B Transmit	13.9	48.8
Country C Receive	15.7	50.6
Country C Transmit	14.9	49.8
Country D Receive	16.8	51.7
Country D Transmit	14.8	49.7
Country E Receive	16.8	51.7
Country E Transmit	15.6	50.5
Average Receive	16.2	51.1
Average Transmit	14.6	49.5

For the CFM portion of the field test, the recovery pilot was not present. For simplicity, the noise floor was set during lineup according to Satellite System Operations Guide (SSOG) procedures for INTELSAT standard CFM at  $-41.0$  dBm<sub>0p</sub>. To compare the resulting noise floors for CSSB and CFM, refer to Table 6 below. As shown, the actual noise floors for CFM and CSSB were set to within 0.5 dB. Note that the value of *componder advantage*, which in one publication [2] is defined as the difference between *talker-active* and *talker-off* noise floors, was not of direct consequence in the field test. The data in Table 6 show that the compander advantage achieved for this field trial was 8.5 dB, the difference between the companded and un-companded noise floors [3].

TABLE 6. NOISE FLOOR COMPARISONS FOR CSSB AND CFM

SIGNAL	POWER LEVEL
1-mW test tone	0 dBm <sub>0</sub>
Recovery pilot	-10 dBm <sub>0</sub>
Unweighted noise in 3.1-kHz bandwidth around recovery pilot	-39 dBm <sub>0</sub>
CSSB equivalent weighted noise	-41.5 dBm <sub>0p</sub>
CFM equivalent weighted noise according to INTELSAT SSOG	-41.0 dBm <sub>0p</sub>
FDM/FM equivalent weighted noise according to INTELSAT SSOG	-50.0 dBm <sub>0p</sub>

### Subjective tests

The subjective performance tests administered by AT&T and DBP were conducted differently: AT&T used call-back interviews; the DBP used service observation.

AT&T identified individual calls by using a traffic analysis unit. AT&T evaluated the quality of these calls by conducting a call-back interview. Using a standardized list of interview questions concerning the quality of various aspects of the circuit as perceived by the talkers, interviewers queried call participants and recorded their answers. The results were processed by an on-site computer, rating the quality as excellent, good, fair, or poor. The data reduction facility at Bell Telephone Laboratories provided the Mean Opinion Score (MOS) and standard deviation for the ratings. The MOS was calculated by assigning values to the ratings (excellent = 4; good = 3; fair = 2; and poor = 1) and then computing the average response value.

In Frankfurt, the DBP routed the 24 circuits under test (12 CSSB and 12 FDM/FM) via the manual international gateway as semiautomatic circuits. Collect calls were monitored during a conversation by experienced operators, a method known as *service observation*. Twelve criteria were used to evaluate the quality of service. At the end of each call, the operators rated the quality of each call as very good, good, fair, or poor. A MOS was then calculated

in a manner similar to that used for the AT&T data.

The three test conditions used in the subjective tests were:

- Condition I 12 SSB AM modulated circuits with companders (CSSB)
- Condition II 12 FM modulated circuits with no companders (FM)
- Condition III 12 FM modulated circuits with companders (CFM)

In the first phase of the subjective tests, conditions I and II operated simultaneously; in the second phase, conditions II and III were run simultaneously. Because of circuit access constraints, each test phase was conducted sequentially by AT&T and DBP. During the first test phase, problems with echo cancellers in Pittsburgh required that they be replaced by echo suppressors. Therefore phase I was divided into two parts: 1A, with echo suppressors; 1B, with echo cancellers. Test results are given in Tables 7 and 8.

TABLE 7. RESULTS OF AT&amp;T SUBJECTIVE EVALUATION

TEST PHASE	SAMPLE SIZE	EXCELLENT	GOOD	FAIR	POOR	MOS*
CSSB-1A	552	43%	38%	13%	6%	3.17
FM-1A	710	43%	41%	12%	4%	3.23
CSSB-1B	400	41%	42%	14%	3%	3.20
FM-1B	421	46%	41%	11%	3%	3.30
CFM-2	628	47%	38%	9%	6%	3.27
FM-2	635	48%	40%	10%	2%	3.34

\* For method of calculating MOS value, see second paragraph at the beginning of this section.

TABLE 8. RESULTS OF DBP SUBJECTIVE EVALUATION

TEST PHASE	SAMPLE SIZE	VERY GOOD	GOOD	FAIR	POOR	MOS*
CSSB-1A	996	12%	75%	11%	2%	2.97
FM-1A	908	14%	73%	11%	2%	2.99
CSSB-1B	309	20%	63%	13%	4%	2.99
FM-1B	275	21%	66%	11%	2%	3.06
CFM-2	516	18%	69%	11%	2%	3.03
FM-2	535	17%	71%	10%	2%	3.03

\* For method of calculating MOS value, see second paragraph at the beginning of this section.

The small differences in MOS values for individual test conditions are not statistically significant. Differences in ratings between Tables 7 and 8 have more to do with the different interpretation of the words "very good" in German and "excellent" in English than with differentiating modulation types. The reasons for this are as follows. It is generally accepted that German operators tend to evaluate the link more critically than do telephone

users interviewed in the U.S. Second, the German expression "very good" is not the equivalent of "excellent" in English. Small differences between results for the A and B portions of the tests can be attributed to differences in quality between echo cancellers and echo suppressors. Note the increase in "very good" scores and the decrease in "good" scores on the DBP side that resulted when echo suppressors were replaced with echo cancellers in the U.S.

It is significant that side-by-side tests of CFM and FDM/FM showed no statistically significant differences from CSSB and FDM/FM. Had both CFM and CSSB scored better than FDM/FM, it would have been justified to say that the companders were masking a noisy terrestrial link. Since this was not the case, noise on terrestrial links between the ISC and the ES could not have contributed significantly to the rating.

The closeness in results for CSSB and CFM warrants one final word. Before the field test, there was some speculation that satellite co-channel and intermodulation noise, being non-thermal in origin, might force differences between the subjective scores for CSSB and CFM, even though thermal equivalent noise floors for both modulations were adjusted to within 0.5 dB of each other. This line of reasoning is based on CSSB being a type of "naked modulation," protected from link noise only by the compander, whereas FM demodulation might also provide immunity from non-thermal impairments. That these differences were not found in this field test is considered quite significant. It is recommended that listener tests be conducted under a laboratory-controlled environment to quantify subjective immunity differences, if any, between CSSB and FM.

### Capacity estimates

The CSSB transponder capacities that can ultimately be achieved in the INTELSAT system will vary, depending on the specific transponder and earth segment characteristics, required  $S/N$ , and interference environment encountered. A parametric study was performed to demonstrate one technique for computing capacity.

The value of 16.2-dB  $S/N$  obtained, shown in Table 5, was rounded to 17.0 dB to account for signaling and tones present in the multichannel load. This value provides a starting point for link budget analysis. Two specific sets of earth station and transponder characteristics were used. The first was a zone beam transponder and earth station with parameters set at the values measured for transponder 53 and the Raisting earth station, respectively. Capacity estimates for this set of parameters are shown in Table 9. The second set of parameters consisted of the published specification values for

a Standard A earth station and specified INTELSAT V zone beam transponder parameters. Results for this set are shown in Table 10.

TABLE 9. CAPACITY ESTIMATES FOR ZONE BEAM WITH MEASURED SPACECRAFT AND EARTH STATION PARAMETER VALUES AND MEASURED AVERAGE LOAD,  $L_c = -22.8$  dBm0

Parameter <sup>a</sup>	INTERFERENCE ENTRIES			
	0	2 (1 reuse)	4 (2 reuses)	6 (3 reuses)
$S/N_{Tot}$ (dB)	17.0	17.0	17.0	17.0
$S/I$ (dB)		24.0	21.0	19.2
$S/(N_{Th} + IM)$ (dB)	17.0	18.0	19.2	21.0
$S/N_{Th}$ (dB)	20.0	21.0	22.2	24.0
$S/IM$ (dB)	20.0	21.0	22.2	24.0
$BO_{ch}$ (dB)	50.3	49.3	48.1	46.3
$BO_{Tot}$ (dB)	6.1	6.6	7.2	6.6
$IBO_{Tot}$ (dB)	12.1	12.6	13.2	12.6
Capacity (channels)	18,000 <sup>b</sup>	18,000 <sup>b</sup>	12,300	9,300

<sup>a</sup>  $S/N_{Tot}$  = signal-to-total noise

$S/I$  = signal-to-co-channel interference

$S/(N_{Th} + IM)$  = signal-to-thermal plus intermodulation noise

$S/N_{Th}$  = signal-to-thermal noise

$S/IM$  = signal-to-intermodulation noise

$BO_{ch}$  = per-channel transponder output backoff

$BO_{Tot}$  = total transponder output backoff

$IBO_{Tot}$  = total transponder input backoff

<sup>b</sup> Bandwidth limited capacity

The estimates in both tables represent transponders that are fully loaded with CSSB only, and for a signal-to-noise density ratio based on the average per-channel load (companded) reported by AT&T for the receive direction. If the  $S/N$  for 4,800-bit/s data is to remain at 24.5 dB, or equivalently, if the recovery pilot-to-noise ratio is to remain at 29 dB, then an average per-channel load different from that reported by AT&T would result in a required  $S/N$  value for a voice channel other than 17 dB. For example, if the average per-channel companded load is  $-20.8$  dBm0 rather than  $-22.8$  dBm0, the required  $S/N$  for a voice channel would be 19 dB; that is, a one-to-one correspondence exists between average per-channel companded load and required voice-channel  $S/N$  if the data  $S/N$  requirement remains fixed.\* This argument implies that any capacity increase which is obtained by decreasing average channel load is made at the expense of objective quality.

\* This conclusion assumes that the unaffected level remains at  $-16$  dBm0; it is not adjusted in response to a change in the average talker level.

TABLE 10. CAPACITY ESTIMATES FOR ZONE BEAM WITH SPECIFIED SPACECRAFT AND EARTH STATION PARAMETERS<sup>a</sup> AND MEASURED AVERAGE LOAD,  $L_c = -22.8$  dBm0

PARAMETER <sup>b</sup>	INTERFERENCE ENTRIES			
	0	2 (1 reuse)	4 (2 reuses)	6 (3 reuses)
$S/N_{Tot}$ (dB)	17.0	17.0	17.0	17.0
$S/I$ (dB)		24.0	21.0	19.2
$S/(N_{Th} + IM)$ (dB)	17.0	18.0	19.2	21.0
$S/N_{Th}$ (dB)	20.0	21.0	22.2	24.0
$S/IM$ (dB)	20.0	21.0	22.2	24.0
$BO_{ch}$ (dB)	46.0	45.0	43.8	42.0
$BO_{Tot}$ (dB)	4.6	5.2	5.2	5.2
$IBO_{Tot}$ (dB)	10.6	11.2	11.2	11.2
Capacity (channels)	13,800	9,550	7,244	4,800

<sup>a</sup> The parameters here are INTELSAT V, VA specified parameters, and the Standard A earth station specification,  $G/T = 41.7$  dB/K.

- <sup>b</sup>  $S/N_{Tot}$  = signal-to-total noise
- $S/I$  = signal-to-co-channel interference
- $S/(N_{Th} + IM)$  = signal-to-thermal plus intermodulation noise
- $S/N_{Th}$  = signal-to-thermal noise
- $S/IM$  = signal-to-intermodulation noise
- $BO_{ch}$  = per-channel transponder output backoff
- $BO_{Tot}$  = total transponder output backoff
- $IBO_{Tot}$  = total transponder input backoff

The CCITT accepted value of average channel load under noncompanded conditions is  $-15$  dBm0, with a standard deviation of 5.8 dB. By using the equation for  $L$  given above in the section on average channel load,  $V_o$  for this case is extrapolated back to be  $-12.87$ . Substituting this value into  $L_c$ , and assuming that unaffected level, standard deviation for the uncompanded load, and  $\tau$  do not change,  $L_c$  is found to be  $-19.5$  dBm0, or 3.3 dB higher than the average load measured by AT&T. This means that a  $S/N$  3.3 dB above that used for the CSSB test, or 20.3 dB, would be required when the average load (uncompanded) is  $-15$  dBm0. Tables 11 and 12 show capacity estimates for this average channel load, using measured and specification spacecraft/earth station parameters, respectively. Results in Table 12 can be directly compared to current INTELSAT transponder loading average capacities for other access techniques (FDM/FM, SCPC, CFM, etc.).\*

It is also worth noting that if pilot tone  $S/N$  requirements had been set to a value suitable for 7.2-kbit/s or 9.6-kbit/s voiceband modems (to provide

\* See, for example, Reference 3 on CFM capacity.

TABLE 11. CAPACITY ESTIMATES FOR ZONE BEAM WITH MEASURED SPACECRAFT AND EARTH STATION PARAMETERS AND CCITT SPECIFIED AVERAGE LOAD,  $L = -15$  dBm0 ( $L_c = -19.5$  dBm0)

PARAMETERS*	INTERFERENCE ENTRIES		
	0	2 (1 reuse)	4 (2 reuses)
$S/N_{Tot}$ (dB)	20.3	20.3	20.3
$S/I$ (dB)		24.0	21.0
$S/(N_{Th} + IM)$ , (dB)	20.3	22.7	28.6
$S/N_{Th}$ (dB)	23.3	25.7	31.6
$S/IM$ (dB)	23.3	25.7	31.6
$BO_{ch}$ (dB)	47.0	44.6	38.7
$BO_{Tot}$ (dB)	7.7	6.6	6.7
$IBO_{Tot}$ (dB)	13.7	12.6	12.7
Capacity (channels)	8,500	6,250	1,600

- \*  $S/N_{Tot}$  = signal-to-total noise
- $S/I$  = signal-to-co-channel interference
- $S/(N_{Th} + IM)$  = signal-to-thermal plus intermodulation noise
- $S/N_{Th}$  = signal-to-thermal noise
- $S/IM$  = signal-to-intermodulation noise
- $BO_{ch}$  = per-channel transponder output backoff
- $BO_{Tot}$  = total transponder output backoff
- $IBO_{Tot}$  = total transponder input backoff

the same capability as current FDM/FM circuits), the required speech  $S/N$  would also go up, causing a drop in capacity.

The method that was used to develop Tables 9 through 12 is as follows. For any single frequency reuse, the value of signal-to-co-channel interference ( $S/I$ ) on each of the up- and down-links caused by imperfect cross-polarization and/or spatial isolation of the antennas was assumed to be 27 dB, resulting in a total  $S/I$  of 24 dB for each reuse. For each number of reuses given in the tables, the signal-to-thermal noise plus intermodulation [ $S/(N_{Th} + IM)$ ] allowable in combination with co-channel interference to achieve the desired  $S/N_{Tot}$  was first determined. In all cases, it was assumed that  $S/N_{Th}$  and the signal-to-intermodulation noise ( $S/IM$ ) were equal. (It should be noted that equal  $S/N_{Th}$  and  $S/IM$  may not provide optimum channel capacity). The desired value of  $S/N_{Th}$  was used to find the output backoff per channel ( $BO_{ch}$ ) by working backwards through down- and up-links to solve for up-link e.i.r.p. The value of  $S/IM$  was used to determine the total transponder output backoff ( $BO_{Tot}$ ) by using the approximation formula,  $S/IM = K_{IM}/(BO_{Tot})^{2*}$ ,

\* This is a convenient rule of thumb for soft-limiter AM/AM characteristics. For a derivation, see Reference 4, p. 246.

TABLE 12. CAPACITY ESTIMATES FOR ZONE BEAM WITH INTELSAT-SPECIFIED SPACECRAFT AND EARTH STATION PARAMETERS<sup>a</sup> AND CCITT SPECIFIED AVERAGE LOAD,  $L = -15$  dBm0 ( $L_c = -19.5$  dBm0)

PARAMETER <sup>b</sup>	INTERFERENCE ENTRIES		
	0	2 (1 reuse)	4 (2 reuses)
$S/N_{Tot}$ (dB)	20.3	20.3	20.3
$S/I$ (dB)		24.0	21.0
$S/(N + I)$ (dB)	20.3	22.7	28.7
$S/N_{Th}$ (dB)	23.3	25.7	31.6
$S/IM$ (dB)	23.3	25.7	31.6
$BO_{ch}$ (dB)	42.7	40.3	34.4
$BO_{Tot}$ (dB)	5.2	5.2	5.2
$IBO_{Tot}$ (dB)	11.2	11.2	11.2
Capacity (channels)	5,600	3,250	825

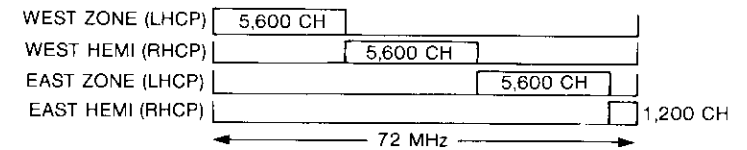
<sup>a</sup> The parameters here are INTELSAT V. VA-specified parameters, and the Standard A earth station specification,  $G/T = 41.7$  dB/K.

- <sup>b</sup>  $S/N_{Tot}$  = signal-to-total noise
- $S/I$  = signal-to-co-channel interference
- $S/(N_{th} + IM)$  = signal-to-thermal plus intermodulation noise
- $S/N_{Th}$  = signal-to-thermal noise
- $S/IM$  = signal-to-intermodulation noise
- $BO_{ch}$  = per-channel transponder output backoff
- $BO_{Tot}$  = total transponder output backoff
- $IBO_{Tot}$  = total transponder input backoff

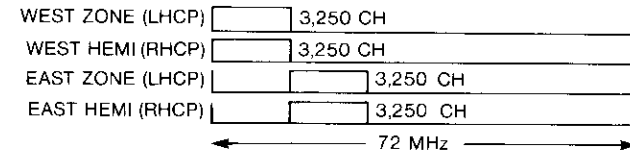
where  $K_{IM}$  is a TWTA-dependent constant, here taken to be 6.025. A bandwidth improvement factor, that is, an improvement in  $S/IM$  when occupancy is less than 50 percent, was also factored into the choice of  $BO_{Tot}$  [5]. Finally, the difference between  $BO_{Tot}$  and  $BO_{ch}$  yields the capacity figure in dB, which, in the bottom row of Tables 9 through 12, is converted into linear units.  $IBO_{Tot}$  is the total transponder input backoff. The methodology described above sets an upper limit on the number of reuses in Tables 9 through 12, since the capacity decreases rapidly as reuse noise approaches the required  $S/N_{Tot}$ .

Capacities higher than those of standard FDM/FM have been estimated in most cases shown in Tables 9 through 12. (For a sample capacity estimate, see Appendix.) Note that the estimated capacity varies with changes in the average channel load, transponder and earth station characteristics, and interference environment. When properly taken into account in the system design, changes in these assumptions will also lead to changes in derived FDM/FM capacities.

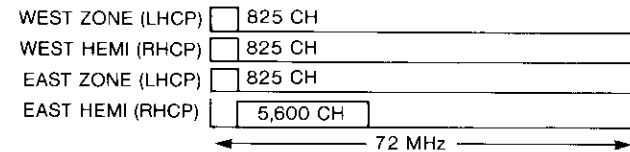
If all transponders in a bank were loaded with CSSB, the achievable capacity would also be highly variable, depending on system assumptions and the specific frequency plan used within the bank of transponders. If the loss of capacity caused by reuse interference is greater than the proportion of transponder bandwidth corresponding to that number of reuses, the transponder bank capacity will usually be maximized by minimizing (or eliminating) reuse interference. This is illustrated in Figure 7 for the capacity estimates shown in Table 12. For convenience, Figure 7 shows the occupied frequencies in each transponder as large blocks of frequencies. In a real system, the CSSB channels would be distributed throughout the transponder in smaller blocks, with the number of frequency reuses being that shown in Figure 7.



(a) Average of 4,500 Channels per Transponder (No Frequency Reuse)



(b) Average of 3,250 Channels per Transponder (1 Frequency Reuse)



(c) Average of 2,019 Channels per Transponder (2 Frequency Reuses)

NOTE: LHCP - LEFT-HAND CIRCULAR POLARIZATION  
RHCP - RIGHT-HAND CIRCULAR POLARIZATION

Figure 7. Transponder Loading Plans for Capacities Using Spacecraft and Earth Station Parameters and  $L_c = -19.5$  dBm0 ( $L = -15$  dBm0)

The above computations are based on an unaffected level of  $-16$  dBm0, which is the Western Electric compander USP. Some variation in this level, depending on average channel load, may be appropriate. As explained in Reference 6, a logical choice for USP is the value that achieves equal multichannel companded and un-companded loads. This choice, which results in efficient system loading, occurs when the USP is  $-14.6$  dBm0 for a  $-22$ -dBm0 average channel load. The value of USP also determines the level of test tones used for transmission checking.

### Conclusions

As with other estimates of capacity that have appeared in the literature (see References 2, 7, and 8), this study established that CSSB is potentially a highly bandwidth efficient analog modulation technique. With a conservative choice of transmission parameters, the study showed that up to 4,500 channels could be accommodated in an INTELSAT V 72-MHz transponder, assuming no frequency reuse (see Figure 7).

Within measurement accuracy, the field test demonstrated that with a noise level equal to  $-41.5$  dBm0p in an un-companded voice channel, CSSB, CFM, and standard FM voice circuits were equally acceptable. The test also showed that 4,800-bit/s modems operated satisfactorily when using CSSB or CFM with a signal level of  $-13$  dBm0 and an unweighted  $S/N$  of 24.5 dB, or equivalently, with a weighted noise floor of  $-41.5$  dBm0p.

With CSSB, achievable transponder capacities will vary greatly, depending on the average per-channel load in the system, the choice of unaffected level in the compander, the ability to frequency plan to minimize intermodulation noise, the level of frequency reuse interference encountered, and the earth and space segment performance characteristics.

### Acknowledgments

*This field test owes a great deal to the initiative and early interest of AT&T, including staff members at the Bell Telephone Laboratories. R. Hedinger, A. Lowe, and D. Boone of AT&T were instrumental in planning, implementing, and running the CSSB test. The Deutsche Bundespost played a key role in establishing the distant-end link. S. Pfaff and R. Schlolaut of the DBP implemented the terrestrial interface and arranged subjective testing. At INTELSAT, H. Keel provided CSM measurements throughout the test. At COMSAT, I. Knight, S. J. Campanella, J. Kolsrud, and H. G. Suyderhoud provided valuable guidance throughout the test and documentation phases.*

### References

- [1] Bell Telephone Laboratories, *Transmission Systems for Communications*, 4th Edition, (Bell Labs Blue Book) 1971, Chap. 9.
- [2] S. J. Campanella, "Companded Single Sideband (CSSB) AM/FDMA Performance," *International Journal of Satellite Communications*, Vol. 1, Issue 1, July-September 1983, pp. 25-29.
- [3] G. G. Szarvas and H. G. Suyderhoud, "Enhancement of FDM-FM Satellite Capacity by Use of Companders," *COMSAT Technical Review*, Vol. 11, No. 1, Spring 1981.
- [4] J. J. Spilker, *Digital Communications by Satellite*, Englewood Cliffs, New Jersey: Prentice-Hall, 1977.
- [5] R. J. F. Fang and W. A. Sandrin, "Carrier Frequency Assignment for Nonlinear Repeaters," *COMSAT Technical Review*, Vol. 7, No. 1, Spring 1977, pp. 227-245.
- [6] R. Brown et al., "Companded Single Sideband (CSSB) Implementation on COMSTAR Satellites and Potential Application to INTELSAT V Satellites," IEEE ICC, 1983, *Proceedings*, Paper E.2.1.
- [7] R. Brown et al., "Companded Single Sideband (CSSB) Transmission," IEEE GlobeCom, 1982, *Proceedings*, Paper A.5.4.
- [8] K. Jonnalagadda, "Single Sideband, Amplitude Modulated, Satellite Voice Communication System Having 6000 Channels Per Transponder," *RCA Review*, Vol. 43, September 1982, pp. 464-488.

### Appendix

To illustrate the method used to estimate transponder capacity, the case of three frequency reuses from Table 9 is used; that is,  $L_c = -22.8$  dBm0 as well as earth station and spacecraft specified parameter values.

In this case, the required signal-to-total noise,  $S/N_{Tot}$ , is 17.0 dB. With three frequency reuses, six interference entries occur—three on each of the up- and down-links. INTELSAT specifies that antenna isolation (spatial or cross-polarization) for its 6/4-GHz antenna systems be at least 27 dB, so it was assumed that all six interference entries were 27 dB each, resulting in a 19.2-dB signal-to-co-channel interference ( $S/I$ ). Thus, to reach the target  $S/N_{Tot}$  value of 17.0 dB, the signal-to-thermal plus intermodulation noise  $[S/(N_{Th} + IM)]$  must be 21.0 dB. It was then assumed that signal-to-thermal noise,  $S/N_{Th}$ , and signal-to-intermodulation noise,  $S/IM$ , were equal, resulting in  $S/N_{Th} = S/IM = 24.0$  dB.

The per-channel up-link e.i.r.p. that would provide a link  $S/N_{Th}$  of 24.0 dB was estimated to be 48.3 dBW. By using the per-channel up-link e.i.r.p., the transponder output backoff per channel,  $BO_{ch}$ , was found from the following:

$$BO_{ch} = \Psi - \text{e.i.r.p.}_u + L_u + U - G - C \quad (\text{A-1})$$

where

- $\Psi$  = satellite saturation flux density, dBW/m<sup>2</sup> (-67.1 dBW/m<sup>2</sup>)  
 e.i.r.p.<sub>g</sub> = per-channel up-link e.i.r.p., dBW (48.3 dBW)  
 $L_u$  = up-link free-space path loss, dB (200.1 dB)  
 $U$  = miscellaneous up-link loss, dB (0.5 dB)  
 $G$  = gain of a 1-m<sup>2</sup> antenna, dBi (37.2 dBi)  
 $C$  = estimated difference between the total input and total output backoff of the transponder, dB (6 dB).\*

By using the above values,  $BO_{ch}$  is 42.0 dB.

The initial estimate of total output backoff is found from the following [4]:

$$10^{(S/IM)/10} = \frac{K_{IM}}{(10^{BO_{Tot}/10})^2} \quad (A-2)$$

where

- $S/IM$  = signal-to-intermodulation ratio, dB  
 $BO_{Tot}$  = total transponder output backoff, dB (expressed as a positive number)  
 $K_{IM}$  = constant, taken to be 6.025.

Converting to dB,

$$S/IM = 10 \log K_{IM} + 2 BO_{Tot} \quad (A-2a)$$

For the present example,  $S/IM = 24.0$  dB. Solving equation (A-2a) for the total transponder output backoff results in  $BO_{Tot} = 8.1$  dB. The initial estimated capacity is then the difference between the per-channel output backoff,  $BO_{ch}$ , and the total output backoff, expressed in absolute terms. In this case,

$$\text{capacity} = 10^{(42.0 - 8.1)/10} = 2,454 \text{ channels}$$

For transponders with less than 50 percent of the bandwidth occupied, an improvement in  $S/IM$  can be achieved with an appropriate random frequency plan; thus, the transponder can be operated closer to saturation to achieve a given  $S/IM$  [5]. Taking this improvement into consideration allows for a higher capacity. The improvement in  $S/IM$  is found by taking the ratio of total transponder bandwidth to total allocated bandwidth.

\* The value of 6 dB was taken from the results of INTEL.SAT's transmission analysis computer program (described in the section on Satellite Link and Transmission Analysis Methodology) for one of the actual TWTs in the test. The value of  $C$  may vary by several decibels between actual TWTs.

$$S/IM \text{ improvement factor} = 10 \log \left( \frac{BW_T}{\# \text{ of channels} \times BW_{ch}} \right) \text{ dB} \quad (A-3)$$

where

- $BW_T$  = transponder bandwidth  
 $BW_{ch}$  = allocated bandwidth per channel

The number of channels (capacity) is the difference between the per-channel output backoff and total output backoff, that is,

$$\text{capacity} = 10^{(BO_{ch} - BO_{Tot})/10} \text{ channels} \quad (A-4)$$

Substituting this into equation (A-3), the result is

$$S/IM \text{ improvement factor} = 10 \log \left( \frac{BW_T}{BW_{ch}} \right) - BO_{ch} + BO_{Tot} \text{ dB} \quad (A-5)$$

This improvement factor can be added to  $S/IM$  in equation (A-2a), and so

$$S/IM = 10 \log K_{IM} + 10 \log \left( \frac{BW_T}{BW_{ch}} \right) - BO_{ch} + 3BO_{Tot} \text{ dB} \quad (A-6)$$

All of the values shown above are known, with the exception of  $BO_{Tot}$ . Thus, equation (A-6) is solved for  $BO_{Tot}$ , and the result is used in equation (A-4) above to find capacity. In the present example,  $S/IM$  is 24 dB,  $K_{IM}$  is 6.025,  $BW_T$  is 72 MHz,  $BW_{ch}$  is 4 kHz, and  $BO_{ch}$  was found to be 42 dB. Thus,  $BO_T$  is 5.2 dB, with a capacity of 4,786 channels (rounded to 4,800 in Table 9), or nearly double the number found without the  $S/IM$  improvement factor.

Note that when the capacity derived from equation (A-6) approaches 50-percent occupancy, equation (A-3) becomes less reliable. In Tables 8 through 11, some entries have as much as 55-percent channel occupancy; above 55 percent, no improvement factor was used.



*Ernest L. Wallace received a B.S. from Southeast Missouri State University in 1959, and an M.S.E.E. in 1972 from the Naval Postgraduate School in Monterey, California. He joined COMSAT in 1982 as an Operations Engineer in the International Standards Group, where he worked on a 32-kbit/s voiceband encoding study for INTELSAT and on the CSSB field trials, and acted as COMSAT Chairman for CCITT Study Group II. He is currently COMSAT's Manager for National Security/Emergency Preparedness telecommunications. Before joining COMSAT, Mr. Wallace spent 22 years in U.S. Naval Communications.*

*Connie Adams received an M.S.E.E. in 1982 from Kansas State University. Since joining COMSAT World Systems Division in 1982, she has been a Member of the Communications Systems Analysis Department, where her responsibilities have included systems analysis for thin-route, low-density telephone service, customer premises business satellite service, and cable restoration for the TAT-7 and 8 cables. Her current interest is in the application of novel (simplified) transmission analysis techniques, analysis techniques for hybrid analog and digital accessing, and signal design for satellite communications.*



*Donald Arnstein is currently Manager of Communications Systems Analysis in COMSAT's Space Communications Division. He has been actively involved in all phases of the analysis, specification, testing, and planning of advanced satellite modulation and in multiple-access techniques for satellite communications, working closely with COMSAT's representatives on the INTELSAT Board of Governors and Technical Committees. Dr. Arnstein received a Ph.D. from UCLA in 1972. Before joining COMSAT in 1979, Dr. Arnstein's career spanned 17 years in systems engineering of defense-related and government-owned satellite and terrestrial communications systems.*

Index: integrated circuits, ion implantation, gallium arsenide

## **Formation of high-quality n-layers in GaAs by ion implantation**

P. J. McNALLY

(Manuscript received December 3, 1984)

### **Abstract**

This paper describes the formation of high-mobility n-type layers and high dopant-activation efficiency by ion implantation of  $^{29}\text{Si}^+$  into semi-insulating GaAs. Room temperature Hall mobility of 4,400  $\text{cm}^2/\text{V}\cdot\text{s}$  for a peak doping density of approximately  $3 \times 10^{17} \text{ cm}^{-3}$ , and computed doping efficiency greater than 90 percent have been achieved. At reduced temperature (100 K) and lower carrier density, mobility of 8,500  $\text{cm}^2/\text{V}\cdot\text{s}$  has been measured. These characteristics of the implanted layer correspond to a computed compensation ratio of approximately 10 percent, which is among the lowest values achieved by ion implantation. This study was conducted using a number of different semi-insulating GaAs substrates grown by both low- and high-pressure liquid-encapsulated Czochralski (LEC) techniques. Results are described which show the dependence of substrate effects on the quality of the implanted layer characteristics.

### **Introduction**

Ion implantation into GaAs has become an established doping technique in the fabrication of devices which range from discrete transistors to large-scale integrated circuits [1]–[3] (for example). The evolution of GaAs implantation technology has been similar to that of silicon-based implantation technology. A viable ion-implantation technology and the availability of improved-quality, large-diameter, semi-insulating GaAs wafers are respon-

sible for many of the advances now being made in increasing the performance and complexity of GaAs devices. The issue of material quality and its effect on device performance is receiving increased attention as the technology moves to the device manufacturing stage [4].

This paper presents results that compare the characteristics of ion-implanted layers produced in both low- and high-pressure LEC undoped GaAs wafers. Czochralski material is grown as a single crystal from a GaAs melt, which may have either a high or low arsenic overpressure during growth. This study was designed to address the key elements of the ion implant/substrate material combination that affect device performance.

### Experimental procedures

Direct ion implantation into undoped semi-insulating GaAs wafers sliced from ingots grown by both the high- and low-pressure LEC methods was performed. Wafers from five ingots were evaluated. Table 1 lists the wafers used from the two growth methods.

TABLE 1. DESCRIPTION OF SLICES USED

INGOT	SLICE NO.	GROWTH TECHNIQUE
1267	184	High Pressure
1267	258	High Pressure
374	4	High Pressure
1-61	13	Low Pressure
1-66	1	Low Pressure
1120	37	Low Pressure

Sample preparation consisted of solvent cleaning followed by removal of approximately 2  $\mu\text{m}$  of the surface in 5:1:1  $\text{H}_2\text{SO}_4:\text{H}_2\text{O}_2:\text{H}_2\text{O}$  at 35°C. Ion implantation was performed with  $^{29}\text{Si}^+$  ions at 200 keV with a dose of  $7 \times 10^{12} \text{ cm}^{-2}$ . The GaAs wafers were (100) oriented and inclined 7° to the ion beam direction to avoid channeling effects. Post-implantation processing included the following steps:

- a. Plasma-enhanced, chemical-vapor deposition of a  $\text{Si}_3\text{N}_4$  cap,  $1,000 \pm 100 \text{ \AA}$  thick.
- b. Furnace annealing at 850°C for 20 min. in  $\text{N}_2/\text{H}_2$  (10-percent  $\text{H}_2$ ).
- c.  $\text{Si}_3\text{N}_4$  stripping and mesa-etching.
- d. Ohmic contact metalization of AuGeNiAgAu and alloy.
- e. Test measurements of  $I_{DSO}$ ,  $\rho_s$ , and  $r_c$ .
- f. Recess etching of one-half of each wafer.
- g. Aluminum Schottky barrier metalization and lift-off.
- h. Wafer dicing and test measurements of  $\mu_H$ ,  $N_s$ , and  $\rho_s$ .

These steps are similar to those previously reported in GaAs FET fabrication [5].

The implanted layer was initially evaluated following the ohmic contact alloying step. Ungated saturation current ( $I_{DSO}$ ), sheet resistance ( $\rho_s$ ), and contact resistance ( $r_c$ ), were measured. The  $I_{DSO}$  measurement is used to determine the sheet carrier concentration,  $N_s$ , between the surface depletion layer and the substrate, using the expression

$$I_{DSO} = qwv_s N_s,$$

where  $q$  is the electron charge,  $w$  is the source-drain width, and  $v_s$  is the electron saturation velocity, taken to be  $1.18 \times 10^7 \text{ cm s}^{-1}$  [6].

All measurements at this stage in the wafer evaluation were taken on the transfer length measurement (TLM) pattern of the mask set, which includes nominal gaps of 5, 10, and 15  $\mu\text{m}$  long  $\times$  300  $\mu\text{m}$  wide. However, the actual measured gap dimensions were used in data analysis to eliminate a potential source of error. In addition, saturation current measurements were made on ungated FETs with source-drain spacing at 2.6  $\mu\text{m}$  as a check on the current values obtained using the TLM structures. The wafers were mapped across the wafer along two perpendicular diameters, using  $I_{DSO}$  as an indication of the uniformity of the implanted layer.

Upon completion of these measurements, the wafers were processed through the remaining steps, as outlined above. To obtain information on that portion of the implanted layer that is important to device operation, recess etching was performed on one-half of the wafer. The target etch depth (the peak of the impurity distribution,  $R_p$ ) was successfully realized on four wafers. This region of the implanted distribution between  $R_p$  and the substrate interface is of particular interest in determining device performance. Hall samples from the wafers were measured, and these measurements were used to obtain sheet carrier concentrations and mobility.

### Ion-implanted layer characteristics

Table 2 gives the results of initial characterization measurements ( $I_{DSO}$ ,  $\rho_s$ , and  $r_c$ ). Both the mean values ( $\overline{I_{DSO}}$ ) and the spread in values (minimum, maximum) of  $I_{DSO}$  across the wafer are listed. The standard deviation,  $\sigma$ , for each wafer was computed, and the ratio  $\sigma/\overline{I_{DSO}}$  was used to determine wafer uniformity. The percent of uniformity for all wafers is between 1.6 and 6.4 percent. The 1.6-percent value determined for wafer 1-61-13 approaches the limit of the implant equipment, which is approximately  $\pm 1$  percent. Implant doping efficiency,  $\eta$ , defined as

TABLE 2. SUMMARY OF DATA FROM  $I_{DSO}$ ,  $\rho_s$ , AND  $r_c$  MEASUREMENTS

WAFER	$\overline{I_{DSO}}$ (mA/mm)	$\sigma(I_{DSO})$ (mA/mm)	$I_{DSO}$ (min)	$I_{DSO}$ (max)	$\sigma/I_{DSO}$ (%)	$\eta$ (%)	$\rho_s$ ( $\Omega/\square$ )	$r_c$ ( $\Omega$ -mm)	SAMPLE SIZE	
									$I_{DSO}$	$\rho_s$
1267-184	1,020	65	933	1,115	6.4	96	255	0.12	36	5
1267-258	999	33	933	1,067	3.3	94	238	0.25	35	5
1-61-13	960	15	933	983	1.6	90	261	0.16	30	5
1-66-1	1,012	26	967	1,066	2.6	95	257	0.22	32	5
374-4	917	27	867	983	2.9	86	282	0.24	27	5
1120-37	716	37	660	767	5.2	67	407	0.20	36	5

$$\eta = \frac{N_s}{N}$$

where  $N_s$  is corrected sheet carrier concentration and  $N$  is implant dose, is shown for the various wafers.

The wafers were corrected for surface depletion using a surface potential value,  $\phi_s = 0.6$  V [6]. Details of this correction have been described by Shenai [7] and Yamazaki et al. [8]. The projected range,  $R_p$ , of the implant profile, and the standard deviation in projected range,  $\sigma_p$ , used to perform the surface depletion correction, are the same values as the LSS range statistics [9], adjusted for a diffusion component in  $\sigma_p$  according to the relation

$$\sigma_p' = \sqrt{\sigma_p^2 + 2Dt}$$

where  $\sigma_p'$  = corrected  $\sigma_p$

$$D = 1.4 \times 10^{-14} \text{ cm}^2\text{s}^{-1}$$

$$t = 1,200 \text{ s}$$

$$\sigma_p = 0.068 \times 10^{-4} \text{ cm.}$$

The correction to the measured sheet carrier concentration is approximately 20 percent of the total implanted sheet charge. The accuracy of this correction is estimated to have about a 5 percent effect on the accuracy of the computed dopant activation efficiencies. The lowest value for  $\eta$  was 67 percent, measured on ingot 1120-37. All other wafers show doping efficiencies in the range of 86 to 96 percent. Within an ingot (represented in the table by the seed and tail wafers from ingot 1267), uniformity values of 3.3 and 6.4 percent and  $\eta$  values of 94 and 96 percent were measured. Data averaged over four of the ingots (1120-37 excluded) are as follows:

$$\overline{I_{DSO}} = 982 \text{ mA/mm}$$

$$\sigma(I_{DSO}) = 38.3 \text{ mA/mm}$$

$$\sigma/\overline{I_{DSO}} = 3.9 \text{ percent}$$

$$\overline{\rho_s} = 258.7 \Omega/\square$$

$$\sigma_{\rho_s} = 14 \Omega/\square$$

$$\sigma/\overline{\rho_s} = 5.4 \text{ percent}$$

These results show good uniformity and doping efficiency among the ingots evaluated. No significant difference was observed between the low-pressure and high-pressure LEC wafers, with the exception of 1120-37 which apparently is of lower quality material. Differences in doping efficiency

between the wafers indicate varying compensation levels in the starting wafers.

Hall measurements were made on the wafers after additional processing, including recess etching as previously mentioned. The results of these measurements reveal significant differences between the low- and high-pressure LEC wafers. Temperature-dependent measurements were carried out on both the full implanted layers and the recess-etched portion of the implanted layer where available. Figure 1 shows the Hall mobility ( $\mu_H$ ) data for the full implanted layer. The sheet carrier concentrations derived from Hall

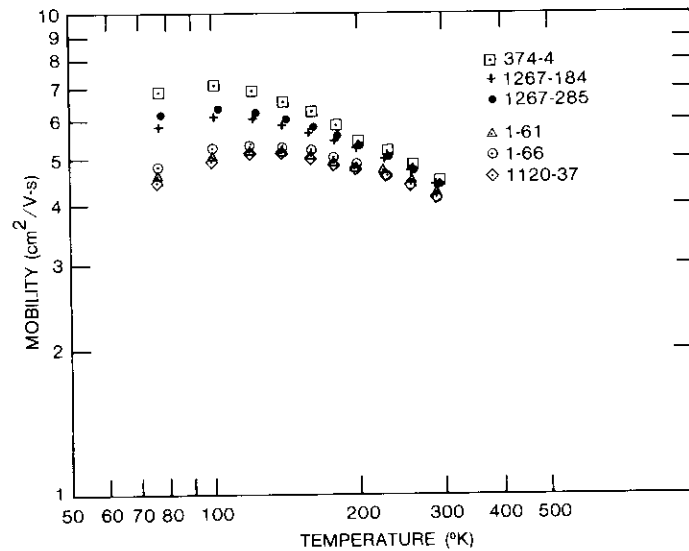


Figure 1. Mobility vs Temperature for the Full Implanted Layer

measurements are shown in Figure 2 for each wafer. The measured values for high-pressure LEC wafers are significantly higher at reduced temperature when compared to the values measured for low-pressure LEC material.

The measurements for both Hall mobility and sheet carrier concentration on wafer 374-4 represent a partially etched implanted layer which occurred during the recess etching step. The mobility is slightly higher, suggesting a lower sheet carrier concentration, as the data in Figure 2 indicate.

Figures 3 and 4 show data measured on four wafers recess-etched to approximately  $R_p$ . These figures compare results on wafers from two low-pressure LEC ingots (1-61 and 1-66) with wafers from a high-pressure LEC ingot (1267). The two growth techniques exhibited similar differences in

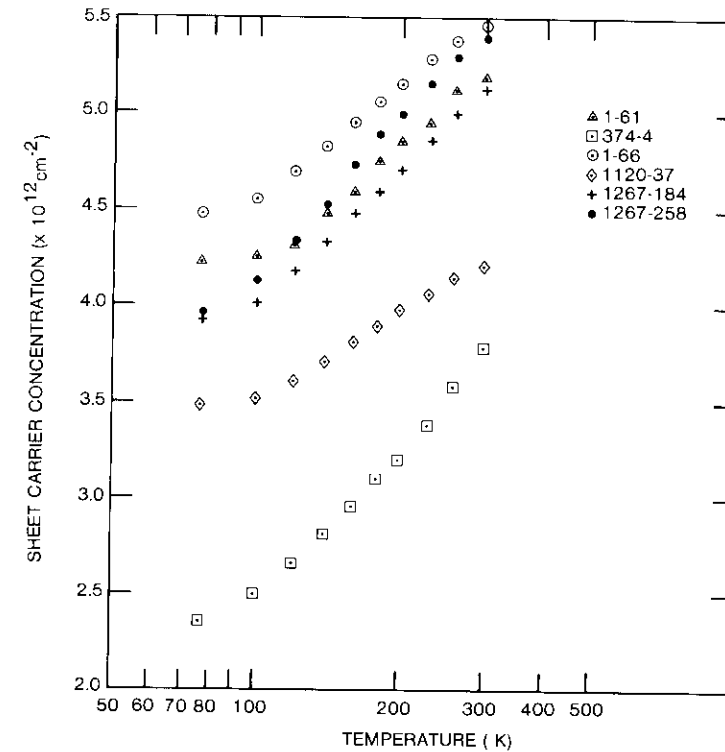


Figure 2. Sheet Carrier Concentration vs Temperature for the Full Implanted Layer

mobility at reduced temperature. Slight differences in recess etch depths are responsible for the differences in measured sheet carrier concentration. The peak values of mobility occur at approximately 100 K for all wafers. Values taken at this temperature, as well as at 300 and 77 K, are listed in Table 3. The highest mobility is observed for ingots 1267 and 374, both for the full implanted distribution (UE) and for the region between  $R_p$  and the substrate interface (E). Mobility increases for the recess-etched wafers, indicating a lower sheet carrier concentration and a high-quality implanted layer/substrate interface. The temperature of maximum mobility and the high values at this temperature ( $\sim 100$  K) are indicative of the low contribution of impurity scattering, which is a measure of the quality of GaAs material [10].

The 300 K Hall mobility values are plotted in Figure 5 for the full implanted layer. This plot shows the dependence of mobility on net donor

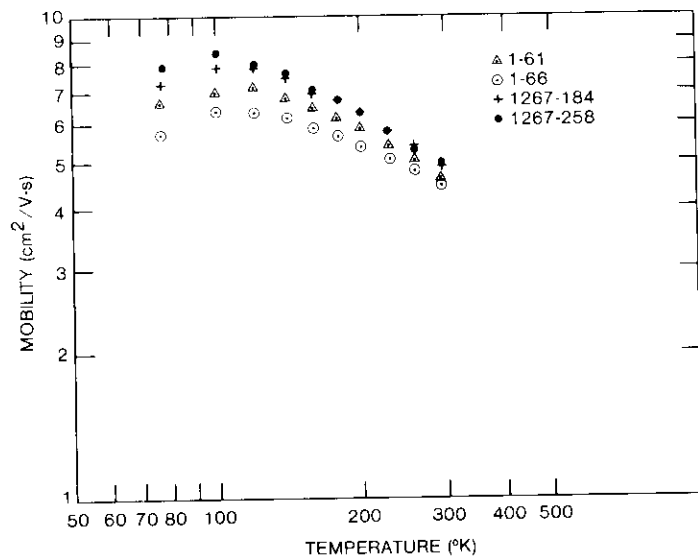


Figure 3. Mobility vs Temperature for the Implanted Region Between  $\sim R_p$  and the Substrate Interface

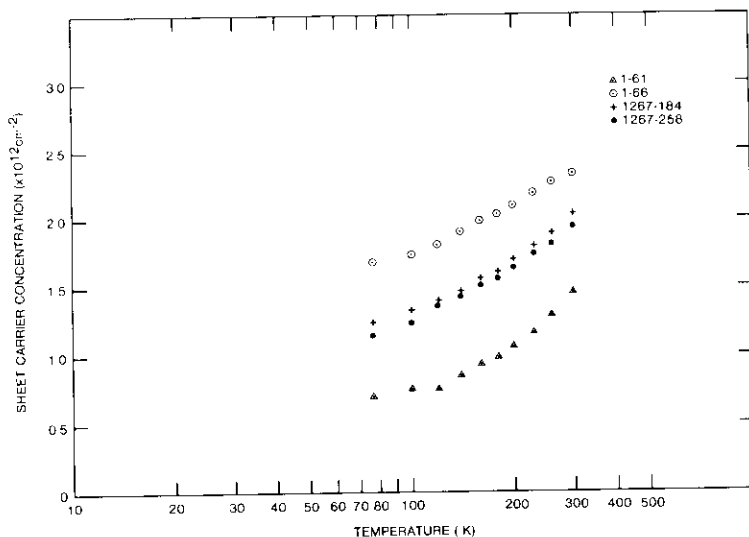


Figure 4. Sheet Carrier Concentrations for Recess-Etched Wafers

TABLE 3. SUMMARY OF HALL DATA TAKEN AT 300, 100, AND 77 K

INGOT	300 K		100 K		77 K	
	$\mu_H$	$N_s$	$\mu_H$	$N_s$	$\mu_H$	$N_s$
1267-184						
UE	4,428	$5.15 \times 10^{12}$	6,170	$3.98 \times 10^{12}$	5,866	$3.77 \times 10^{12}$
E	4,860	$2.04 \times 10^{12}$	7,900	$1.33 \times 10^{12}$	7,290	$1.24 \times 10^{12}$
1267-258						
UE	4,443	$5.4 \times 10^{12}$	6,400	$4.08 \times 10^{12}$	6,280	$3.87 \times 10^{12}$
E	5,120	$1.85 \times 10^{12}$	8,500	$1.22 \times 10^{12}$	8,100	$1.11 \times 10^{12}$
1-61-13						
UE	4,345	$5.09 \times 10^{12}$	5,072	$4.25 \times 10^{12}$	4,680	$4.23 \times 10^{12}$
E	4,615	$1.46 \times 10^{12}$	6,940	$7.57 \times 10^{11}$	6,604	$7.03 \times 10^{11}$
1-66-1						
UE	4,220	$5.48 \times 10^{12}$	5,242	$4.54 \times 10^{12}$	4,825	$4.46 \times 10^{12}$
E	4,450	$2.33 \times 10^{12}$	6,389	$1.74 \times 10^{12}$	5,742	$1.67 \times 10^{12}$
374-4						
UE*	4,488	$3.79 \times 10^{12}$	7,252	$2.47 \times 10^{12}$	7,110	$2.28 \times 10^{12}$
1120-37						
UE	4,188	$4.22 \times 10^{12}$	5,000	$3.52 \times 10^{12}$	4,532	$3.50 \times 10^{12}$

\*Wafer received partial etch of the n-layer.

concentration for different values of the compensation ratio,  $\theta$  [10]. The net donor concentration for the wafers was determined from Hall and  $I_{DSO}$  data and the relation

$$N_s = \sqrt{\pi/2} N_m \sigma_p [1 + (\text{erf } R_p / \sqrt{2} \sigma_p)]$$

where  $N_s$  = sheet carrier concentration  
 $N_m$  = net donor concentration at  $R_p$   
 $\sigma_p$  = standard deviation in projected range  
 $R_p$  = projected range.

The data in Figure 5 show a clustering near the  $\theta = 0.1$  curve which agrees with the doping efficiency values obtained in Table 2. The mobility was observed to be nearly constant through the implanted layer based on gated Hall measurements. Figure 6 shows an example of measurements on Hall samples from wafer 1267-258. These results are similar to previously published results on mobility vs depth for ion-implanted profiles in GaAs [11], [12].

Look has shown [12] that the Hall and drift mobilities are approximately equal for carrier concentrations in the  $10^{17} \text{ cm}^{-3}$  range in GaAs. This permits comparison with theoretical values. In Figure 5, data from Duncan et al. [13] and Clark et al. [14] taken under ion implant conditions similar to those

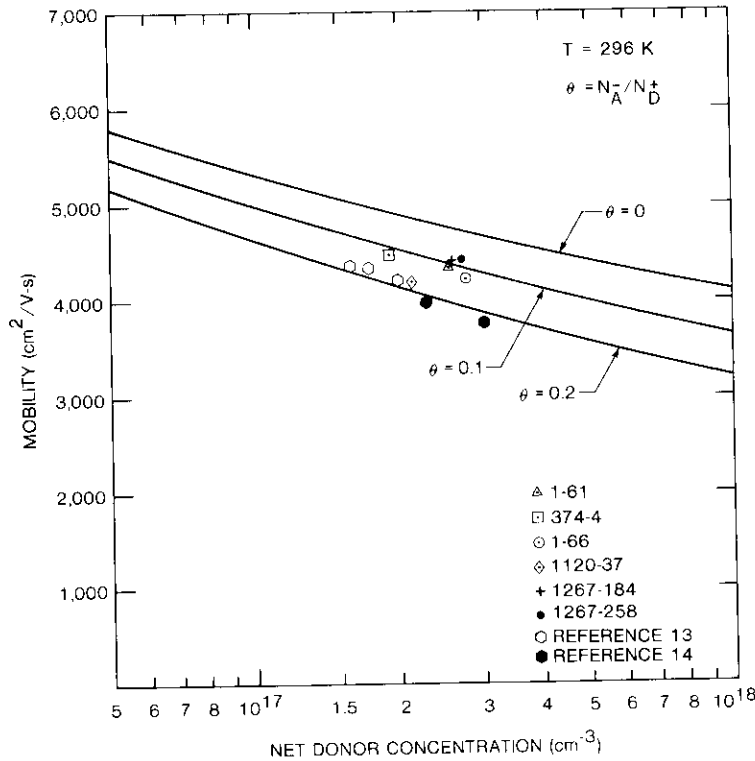


Figure 5. Mobility vs Net Donor Concentration for the Full Implanted Layer Showing Compensation Ratios in the Different Wafers

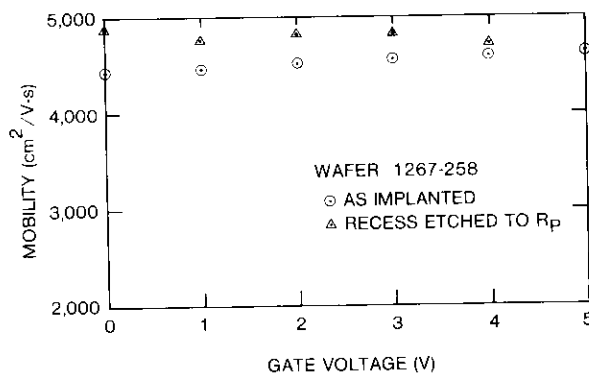


Figure 6. Mobility vs Gate Voltage Indicating Depth Dependence Through the Implanted Impurity Distribution

of the present work, are shown for comparison. The referenced data show compensation ratios near 0.2, and lower mobility values for similar net donor concentrations. The data were derived from Hall measurements to determine compensation ratio and mobility. The work in Reference 13 included both low- and high-pressure LEC starting material and concluded that both material types produce similar implanted layer behavior. As the present work demonstrates, it is necessary to perform characterization measurements at reduced temperatures in order to compare the quality of the implanted layers.

The work in Reference 14 was performed with high-pressure LEC material which showed lower dopant activation efficiency and thereby indicated a higher compensation ratio than was observed in the present work. The referenced study does not report on implanted layer characteristics at reduced temperature.

### Summary

Semi-insulating undoped GaAs wafers from five ingots grown by both low- and high-pressure LEC methods were ion-implanted and characterized. Ungated saturation current measurements showed high dopant activation efficiency in the 90-percent range and uniformity of the implanted layers as low as 1.6 percent. These characteristics, measured at 300 K, do not seem to depend on the growth method used to produce the GaAs. Also, mobility data taken at 300 K show little dependence on the source of material for the full implanted layer. The measured values range between 4,188 and 4,433 cm<sup>2</sup>/V-s and indicate a compensation ratio of approximately 10 percent or less in the carrier concentration range of 2 to 3 × 10<sup>17</sup> cm<sup>-3</sup>.

Recess etching to remove approximately one-half of the implanted layer produced higher mobilities for the portion of the implanted region between R<sub>p</sub> and the substrate interface. The data show differences between the two growth methods, with the high-pressure LEC wafers yielding higher values of mobility. This is particularly evident at reduced temperatures, where it is expected that increased scattering (reflecting material quality) will be encountered. The data also show that the implanted region near the substrate interface, which forms the conducting channel of FET devices, exhibits good transport properties.

At 100 K, mobilities of 6,940 and 8,500 cm<sup>2</sup>/V-s were measured for low- and high-pressure LEC material, respectively. Comparison of these results with published data for similar ion implant conditions and net donor concentrations in the implanted layer showed that higher mobilities and lower compensation ratios were achieved in the present work.

## Acknowledgment

The author is indebted to R. Porter for his excellent technical assistance in performing electrical measurements on the wafers used in this work.

## References

- [1] M. Feng et al., "Optimization of Ion Implanted Low Noise GaAs Metal-Semiconductor Field Effect Transistors," *Journal of Applied Physics*, Vol. 54, No. 4, August 15, 1984, pp. 1171-1176.
- [2] B. M. Welch et al., "LSI Processing for Planar GaAs Integrated Circuits," *IEEE Transactions on Electron Devices*, Vol. ED-27, No. 6, June 1980, pp. 1116-1124.
- [3] Y. Ishii et al., "Processing Technologies for GaAs Memory LSIs," GaAs IC Symposium, Boston, MA, October 1984, *Technical Digest*, pp. 121-124.
- [4] A. Christou, "GaAs MMICs: Manufacturing Trends and Issues," GaAs IC Symposium, Boston, MA, October 1984, *Technical Digest*, pp. 149-153.
- [5] P. J. McNally, "Ion Implantation of Boron in GaAs MESFETs," *IEEE Electron Device Letters*, Vol. EDL-5, No. 4, April 1984, pp. 126-128.
- [6] H. M. Hobgood et al., "High Purity Semi-Insulating GaAs Material for Monolithic Microwave Integrated Circuits," *IEEE Transactions on Electron Devices*, Vol. ED-28, No. 2, February 1981, pp. 140-149.
- [7] K. Shenai, "Analytical Solutions for Threshold Voltage Calculations in Ion Implanted IGFETs," *Solid State Electronics*, Vol. 26, No. 8, August 1983, pp. 761-766.
- [8] H. Yamazaki et al., "Low Dose Si Ion Implantation Into Semi-Insulating LEC GaAs," *Electronics Letters*, Vol. 17, No. 21, 1981, pp. 817-819.
- [9] S. G. Liu et al., "Ion Implantation of Sulfur and Silicon in GaAs," *RCA Review*, Vol. 41, June 1980, pp. 227-262.
- [10] W. Walukiewicz et al., "Electron Mobility and Free-Carrier Absorption in GaAs: Determination of the Compensation Ratio," *Journal of Applied Physics*, Vol. 50, No. 2, February 1979, pp. 899-907.
- [11] P. R. Jay et al., "Magnetotransconductance Mobility Measurements on GaAs MESFETs," *IEEE Electron Device Letters*, Vol. EDL-2, No. 10, October 1981, pp. 265-267.
- [12] D. C. Look, "Schottky Barrier Profiling Techniques in Semiconductors: Gate Current and Parasitic Resistance Effects," to be published.
- [13] W. M. Duncan et al., "A Direct Comparison of LEC GaAs Grown Using Low- and High-Pressure Techniques," *IEEE Electron Device Letters*, Vol. EDL-4, No. 6, June 1983, pp. 199-201.
- [14] R. C. Clark et al., "Transient Capless Annealing of Ion-Implanted GaAs," *IEEE Transactions on Electron Devices*, Vol. ED-31, No. 8, August 1984, pp. 1077-1082.



Philip J. McNally received a B.S. in Physics from St. Francis College in 1959 and pursued graduate studies at Pennsylvania State University and Northeastern University. Prior to joining COMSAT Laboratories in 1974, he was with Ion Physics Corporation and Honeywell, Inc., where he was an early contributor in the field of ion implantation and its application to semiconductor device technology. These activities included both silicon and compound semiconductor devices, the latter emphasizing photodetector development. He is currently a Research Scientist in the Microelectronics Division at COMSAT, where he has been involved in research on IMPATT diodes, ion implanted GaAs FETs, and Schottky barriers. He is currently responsible for ion implantation technology development for GaAs integrated circuits. He is a member of the IEEE, Sigma Pi Sigma, and Delta Epsilon Sigma.

## ***Simulation of deployment dynamics for INTELSAT VI transmit and receive boom/antenna systems\****

P. K. JAMES

(Manuscript received November 16, 1984)

### ***Abstract***

The INTELSAT VI satellite is one of the largest commercial communication satellites currently under development. Both its 4- and 6-GHz transmit and receive antenna systems are stowed during launch and subsequently deployed to their on-orbit configurations. The deployment dynamics of both antenna systems are simulated using NBOD2, a general-purpose dynamics computer program. The spacecraft's stationary platform and both antenna systems are modeled as five bodies coupled by gimbaled hinges, forming a topological tree. The deployment mechanism in each case is a negator spring integrated with a viscous-fluid-damped actuator. The torques generated by these mechanisms are input into the program at the hinge axis. Each hinge axis is initially frozen, then released during simulation as deployment begins. Inertia and kinematic effects are also modeled. Results of the simulation provide data at fraction-of-a-second intervals for the deployment rate, acceleration, torque, angular momentum, kinetic energy, latch-up time, and latch-up velocity associated with each deployment system. Results of the simulation are then correlated with preliminary empirical data gathered from engineering models on which life tests both with and without system inertia were conducted. The key accomplishments of this simulation

---

\* This paper is based on work performed at COMSAT Laboratories under the sponsorship of the International Telecommunications Satellite Organization (INTELSAT). Views expressed are not necessarily those of INTELSAT.

program, as addressed here, have been to predict the behavior of both deployment systems; the use of simulation as a design tool in the final design of the deployment mechanism; and the successful simulation of viscous-fluid-damped actuators.

### Introduction

The deployment sequence of the antenna systems has been analytically modeled using NBOD2 [1], a general-purpose dynamics computer program. In the INTELSAT VI 4-GHz transmit antenna system, the deployment mechanism located at the boom/antenna interface deploys the dish. In both the 6-GHz receive-boom deployment and the 4-GHz transmit-boom deployment, the deployment mechanism located near the spacecraft platform surface deploys that body. The deployment mechanism, also known as the actuator, is represented by the gimbaled hinge in NBOD2, and is used to control the deployment rate so that the latch-up load generated by the deploying member is minimized.

To achieve the final on-orbit configuration of the receive and transmit antennas, both antennas are deployed from their stowed launch configuration. The deployment of the transmit antenna, a 3.2-m dish, is accomplished in two stages. First the dish is deployed through an angle of  $223.7^\circ$ , which provides the necessary clearance to deploy the receive antenna. After the transmit antenna has been deployed, the 2.0-m receive antenna is fully deployed. The receive antenna is deployed using a single-stage,  $84.75^\circ$  deployment. The final stage of the transmit antenna deployment consists of deploying the antenna/boom assembly through an angle of  $119.7^\circ$ .

Deployment in each case is accomplished by using a rotary negator spring mechanism with an integral viscous-fluid damping assembly. At the beginning of the deployment, the viscous damped actuator provides low damping up to a certain deployment angle, since high kinetic energy is needed to initiate deployment. After this angle is reached, the damping is increased exponentially to a high level for the balance of the deployment sequence [2]. NBOD2 was used to model and analyze the deployment sequence based on estimated and measured data provided by Hughes Aerospace Corporation (HAC). Parameters of interest were deployment rate, acceleration, magnitude of applied torque, damping characteristics, spacecraft body forces, and kinetic energy. These parameters are computed at each time step throughout the deployment process, and are used for determining the adequacy of the deployment mechanism. The deployment simulation of the receive and transmit antenna system was conducted, and the results have provided data at fraction-of-a-second intervals of each deploying member's dynamic state, from its initial release to latchup. The importance of these results lies in the insight gained by the analyst or

designer in monitoring mechanism performance before actual design development begins.

The basic assumptions underlying the simulation model are as follows:

- a. The stationary platform is taken to be the inertial reference, and its center of mass is the origin of the model coordinate system.
- b. The spinning rotor and its associated angular momentum have a negligible effect on the deployment dynamics of the two systems.

### The dynamic model and general program input data

The INTELSAT VI spacecraft platform and the 4- and 6-GHz antenna/boom assemblies are modeled as two 3-body systems, coupled by gimbaled hinges, forming a topological tree. Each 3-body system consists of the antenna, the boom, and the spacecraft body (which is shared by both systems). The model thus has a total of five bodies. Figure 1 is an illustration of the INTELSAT VI spacecraft with its deployable members fully deployed.

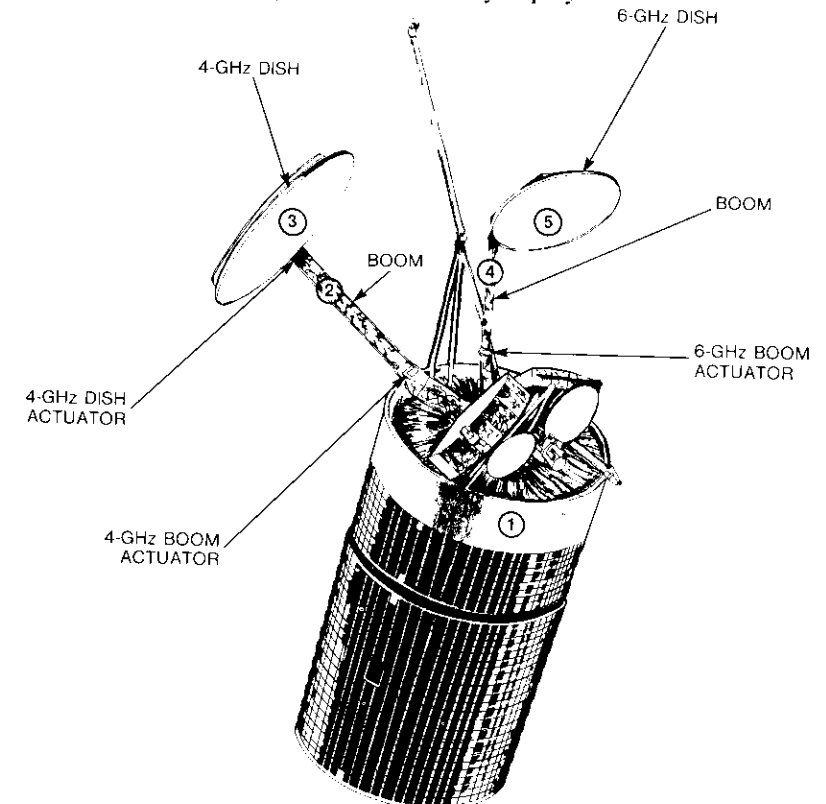


Figure 1. Deployment Mechanisms of the INTELSAT VI Spacecraft

To establish the dynamic model, it is necessary to know the mass, moments and products of inertia, applied torque, damping characteristics, physical geometry, initial angular displacement, and initial angular rate of each body. The deployable members of the model are initially stowed, and no angular displacement or motion takes place in the reference system. It is necessary to locate each body's center of mass with respect to the deployment mechanism that it is attached to, and also to locate the relative position of deployment mechanisms between each body. These parameters are input into the program as position vectors, which act as connecting branches of the topological tree. All parameters used were obtained from HAC and served as input data to the program. Additional program inputs include the integration step-size and the time to end the simulation.

Each body and its associated parameters are input into the program and labelled sequentially, beginning with the body whose mass is predominant. The principal body in the program is the stationary platform within the INTELSAT VI spacecraft. Other components of the spacecraft are modeled as rigid bodies and labeled according to their positions relative to the principal body (see Figure 1). These positions then determine the order by which other spacecraft components are labeled. The deployment mechanisms (actuators) are characterized in the NBOD2 program as gimballed hinges providing three degrees of freedom, which allow rotational motion between the bodies they connect. These hinges are also assigned labels according to the same format mentioned above. Figure 2 represents the INTELSAT VI spacecraft platform with its deployable members stowed. The center of mass of body 1 is chosen

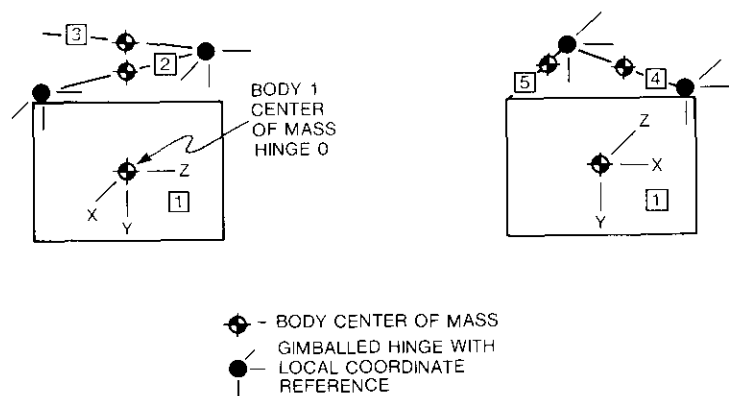


Figure 2. INTELSAT VI Spacecraft Model With Deployable Members Stowed

to be the origin of the system and is characterized as a motionless, six-degree-of-freedom gimballed hinge, thereby establishing the necessary labeling sequence of the hinges. Each hinge contains three mutually orthogonal axes, which constitute a local coordinate reference. All vectors associated with forces, torques, and relative body kinematics can be referred to any set of hinge axes via an input transformation matrix, which must be specified. The program default is an identity matrix which implies that the hinge axes are parallel to the system spacecraft axes (see the sample input data in Appendix A, Figure A-1, lines 8 through 10).

**Deployment mechanism characterization**

The deployment mechanism is an integral negator spring mechanism with a viscous-fluid-damped actuator. An example of the receive-boom deployment mechanism is illustrated in Figure 3. Figures 4a and 4b show two additional views, which highlight the characteristics of the ball-bearing configuration

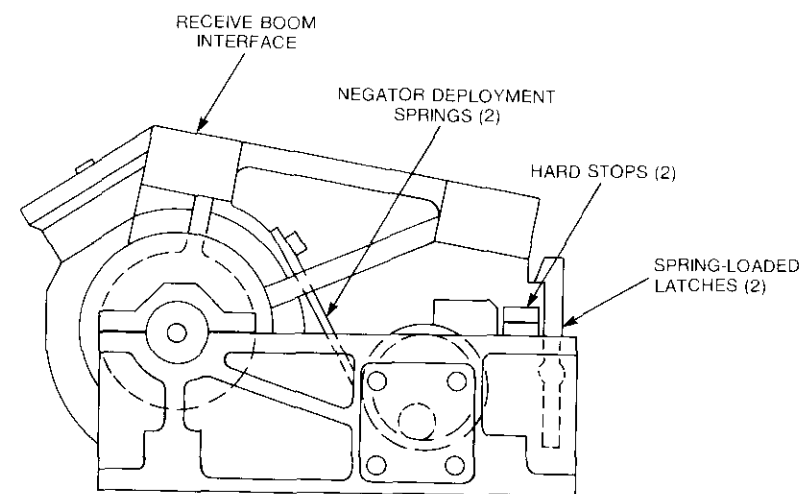
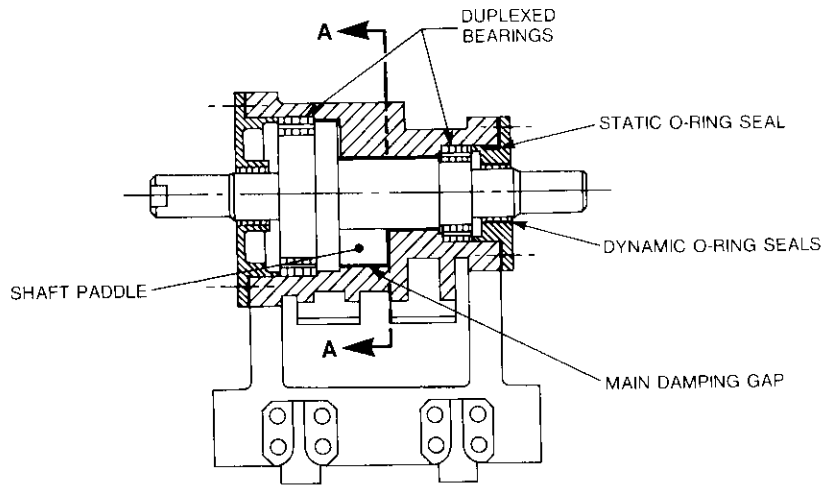
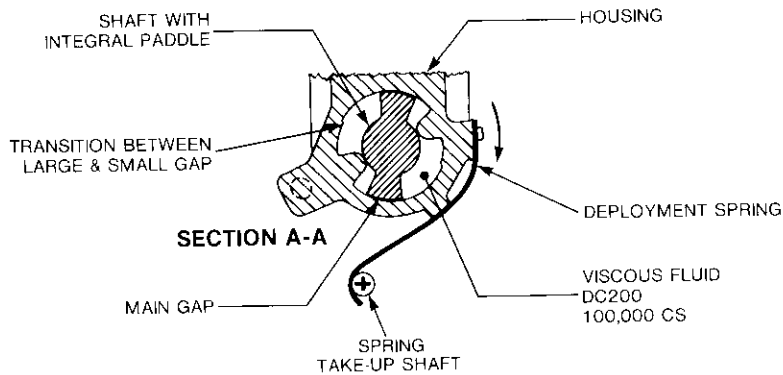


Figure 3. Receive-Boom Deployment Mechanism (Deployed State)

and the viscous-damped actuator. These figures illustrate the basic characteristics of each of the three actuators, which, as mentioned above, are the gimballed hinges in NBOD2. Since these hinges allow rotational motion about one axis only, input conditions of the program are adjusted to constrain motion about two of the axes. Thus, for each hinge, one free degree of freedom and two constrained degrees of freedom are required.



(a)



(b)

Figure 4. Receive-Boom Deployment Mechanism

The deployment mechanism provides the torque that ensures full deployment of the boom or antenna and minimizes latch-up loads. This is accomplished by the combined action of the negator spring and the viscous-damped actuator. The viscous-damped actuator is designed to include a transition region where damping is increased significantly (see Figures 4a and 4b). The internal cavity of the damping mechanism is filled with Dow Corning 200, a fluid with a viscosity of 100,000 centistokes. The damping torque is induced as the

paddle moves during deployment, forcing the transfer of oil through the main gap from one side of the paddle to the other. When the paddle enters the transition region, the damping torque increases dramatically because of the reduction in the gap. The behavior of the actuator just described is typical of the five actuators on the INTELSAT VI satellite.

The variation in damping system response between the three deployments is shown in the simulated graphical representations of Figures 5a, 5b, and 5c. (Program input parameters and the viscous shear-damping formulation were obtained from HAC [2].) Figures 5a-5c differ because of the actuator design requirement that the damping rate be predicated on the magnitude of kinetic energy, which must be retarded at the end of deployment. For example, the 6-GHz receive-boom actuator has two paddles, as shown in Figure 4b, and the damping limit is approximately 720 N-m-s/rad as seen from the graph in Figure 5c. On the other hand, the 4-GHz transmit-boom actuator whose internal features (not illustrated) are similar to those shown in Figure 4b, has an approximate damping limit of 960 N-m-s/rad, as seen in Figure 5b. The 4-GHz transmit antenna or dish actuator whose internal features consist of only one paddle (not illustrated) has a damping limit of approximately

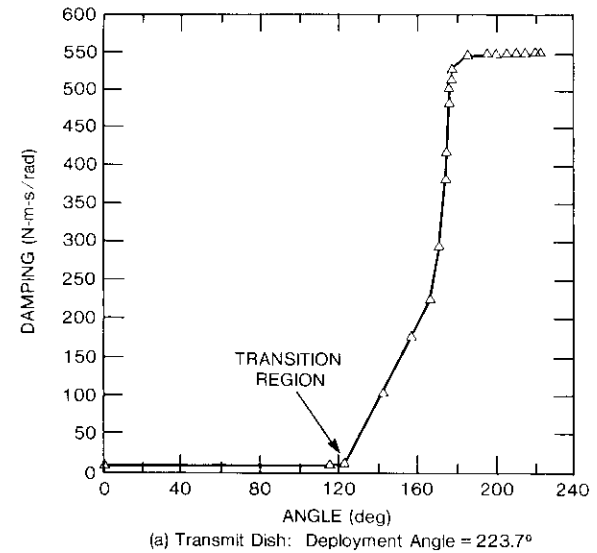
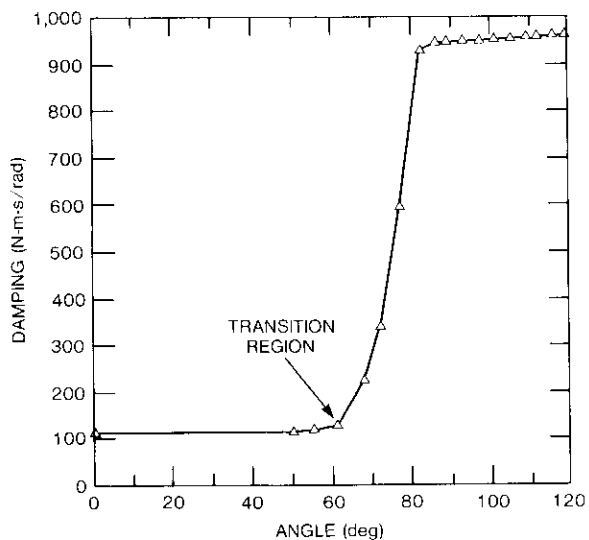
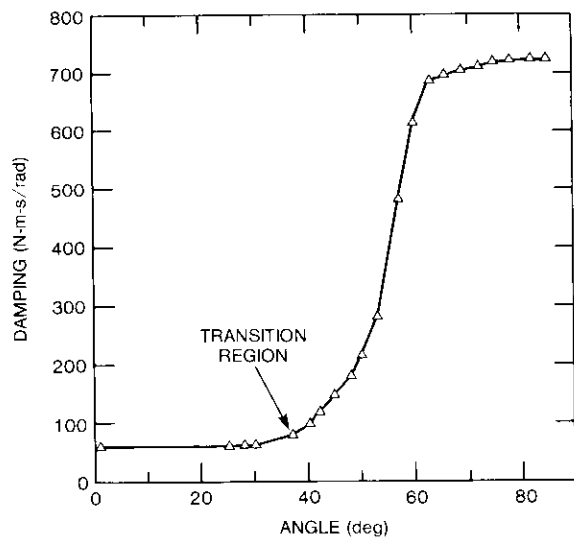


Figure 5. Actuator Damping Rates for Three Actuators



(b) Transmit Boom: Deployment Angle = 119.7°

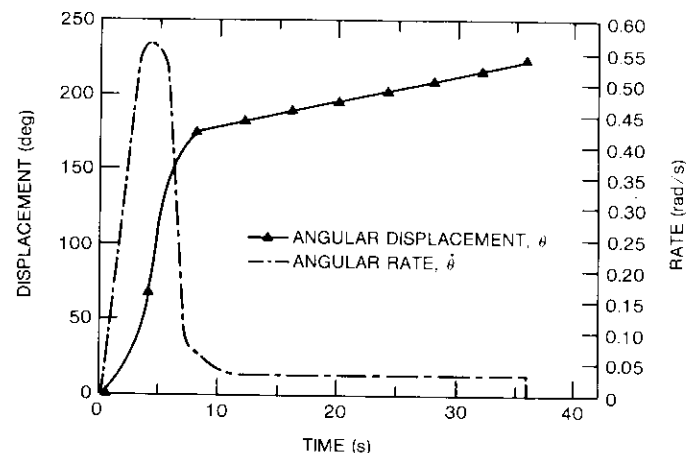


(c) Receive Boom: Deployment Angle = 84.75°

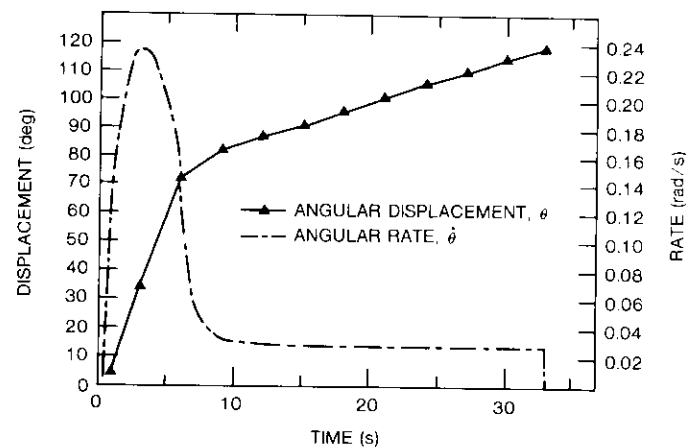
Figure 5 (continued).

550 N-m-s/rad, shown in Figure 5a. The mass that must be deployed is a distinguishing factor in the design of each actuator, shown in Figure 1. The mass deployed by the 4-GHz transmit-boom actuator is 45.16 kg. The mass

deployed by the 6-GHz receive-boom actuator is 19.61 kg, and the mass deployed by the 4-GHz transmit-antenna (dish) actuator is 35.06 kg. The actuators are also designed so that damping will be constant during initial deployment and nearly constant at the end, to ensure a high and low kinetic energy of the respective members. The behavior of the actuators during deployment is illustrated in a series of graphs that show the curves for simulated angular rate and displacement vs time (see Figures 6a, 6b, and 6c).



(a) Transmit Dish



(b) Transmit Boom

Figure 6. Angular Displacement and Rate for Three Actuators

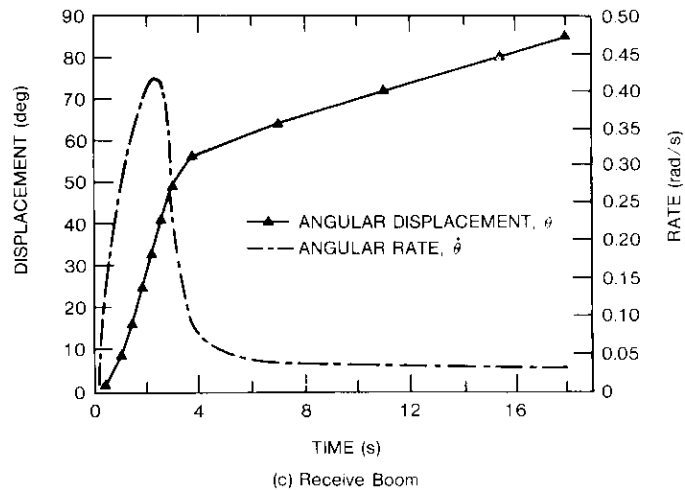


Figure 6 (continued).

The overall effect of the actuators can be summarized in this way: The action of the negator spring, which is barely resisted by constant low damping during initial deployment, causes a steep rise in the actuator rate. As the actuator enters the transition region, its angular rate decreases rapidly as high viscous damping is applied; this increase does not overcome the negator spring action but reduces it, so that the angular rate is small and constant at the end of deployment. The angular momentum ( $I\dot{\theta}$ ) and the kinetic energy ( $1/2 I\dot{\theta}^2$ ) of the deploying system are reduced rapidly and remain constant toward the end of deployment, producing the effect for which the actuators were designed and for which the NBOD2 program has provided the modeling and simulation capability.

#### Mechanism equation of motion and torque input data

The deployment equation of motion for each deployment mechanism can be characterized accordingly:

$$T_{\text{negator}} = [I] \ddot{\theta} + \text{DPC}(\lambda) \dot{\theta} + T_{\text{bearing/cable}}$$

where  $T_{\text{negator}}$  is the spring torque applied by the deployment actuator. It is a fourth-order polynomial function of the angular displacement  $\theta$ , which is the angular rotation between the stowed and deployed state (see Table 1).  $\text{DPC}(\lambda)$

TABLE 1. APPLIED AND RESISTIVE TORQUE (N-m)

SYSTEM	APPLIED TORQUE* (NEGATOR SPRING; N-m)	BEARING/ CABLE TORQUE,* (N-m)	DEPLOYMENT DEVICE
4 GHz	$22.78 - 3.5\theta + 0.83\theta^2 - 0.19\theta^3 + 0.028\theta^4$	-0.68	Dish Actuator
4 GHz	$-31.01 - 5.32\theta - 4.29\theta^2 - 2.24\theta^3 - 0.43\theta^4$	0.68	Boom Actuator
6 GHz	$-29.76 + 2.19\theta + 3.78\theta^2 - 5.98\theta^3 - 3.83\theta^4$	0.68	Boom Actuator

\* For the input of the applied and resistive torques, clockwise is positive and counterclockwise is negative.

is primarily a function of temperature, gap size,  $\theta$ , shear rate, dynamic viscosity of the fluid, and paddle geometry configuration (see Figure 4b). This parameter must be computed interactively during the simulation. The variable  $\ddot{\theta}$  is the angular acceleration, and  $[I]$  is the inertia tensor of the deployable member. Variables  $\theta$ ,  $\dot{\theta}$ , and  $\ddot{\theta}$  are initialized to zero at the beginning of the simulation. The resistive bearing/electrical cabling torque is assumed to be constant throughout the deployment.

Moments and products of inertia, and the mass of each member of the model, are given in Tables 2 and 3. The torques are combined and input

TABLE 2. INERTIAL PROPERTIES

SYSTEM	INERTIA DATA (kg-m <sup>2</sup> )*						DEPLOYMENT DEVICE
	$I_{xx}$	$I_{yy}$	$I_{zz}$	$I_{xy}$	$I_{xz}$	$I_{yz}$	
4 GHz	17.94	4.13	15.18	0.10	-0.20	-6.1	Boom
	28.51	20.85	49.14		3.5	0.10	Dish
6 GHz	1.1	5.02	3.94	-0.50	0.30	-2.3	Boom
	3.72	3.04	6.73	0.30	-0.70	-0.70	Dish

\* All moments and products of inertia take into account the individual body's center of gravity.

TABLE 3. MASS PROPERTIES

SYSTEM	DISH (kg)	BOOM (kg)	DESPUN PLATFORM (kg)
4 GHz	35.06	10.1	1,044.5
6 GHz	12.57	7.04	

into the program at the hinge axis about which motion is allowed, via the body and hinge labeling scheme. Each hinge axis, which contains the free vector, is initially frozen and then released during simulation at the beginning of deployment. Figures 6a, 6b, and 6c show the simulated behavior of the angular displacement,  $\theta$ , and angular rate,  $\dot{\theta}$ , of the deployment system. These two variables, along with the angular acceleration (not shown), represent the motion of the actuator at any given instant. Figures 5 and 6 may be used to assess the simulated performance of the actuators during deployment. Figure 7 is a sketch depicting the deployment history of both assemblies: the 4-GHz antenna/boom deployment is performed in two separate stages with a time delay between them, during which the 6-GHz receive boom is deployed.

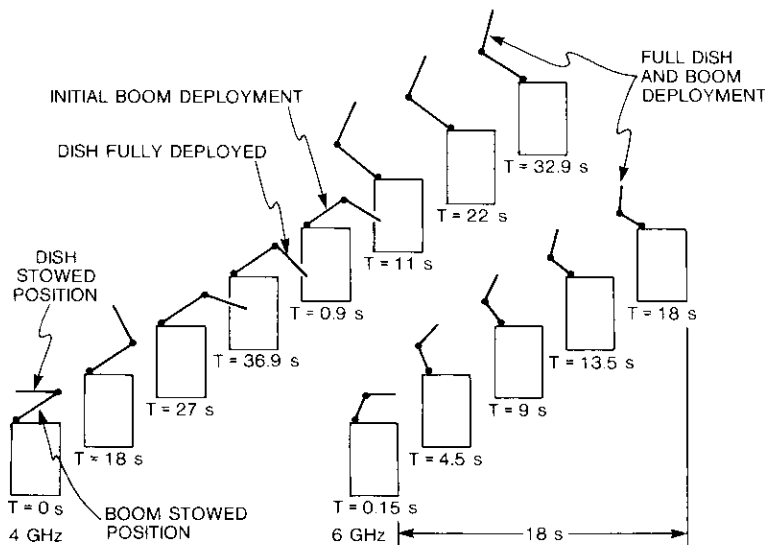


Figure 7. INTELSAT VI 4- and 6-GHz Antenna/Boom Deployment

### Simulation results

The main purpose in simulating and analyzing the dynamics of the deployable members of the INTELSAT VI spacecraft is to verify the adequacy of its deployment mechanisms. For this reason, it was useful to study the deployment dynamics at small time intervals from initial release to latchup.

Originally, on completion of the simulated deployment, high latch-up velocities were observed for both the transmit-boom and transmit-antenna

actuators. Hughes Aerospace, the designer of the deployment mechanisms, was informed of the simulation results, and the following changes were made to the actuators:

- a. The damper configuration of the transmit-dish actuator was altered by making the large gap region angularly smaller and rotating the paddle  $40^\circ$  closer to the high damping region.
- b. The applied spring torque of the transmit-boom actuator was changed by reducing the number of negator springs from 6 to 4 per set.

The receive-boom actuator remained unchanged. HAC later supplied COMSAT with a more accurate characterization of the resistive torque, which was caused by the viscous shear-damping output of each actuator. These changes to the torque were then input to the NBOD2 program, and results of the simulation indicated normal actuator performance. Table 4 is a summary of simulation results, indicating full inertial loading at an ambient temperature of  $72^\circ\text{F}$ . For comparison, HAC's life-test results for time and angular rate at end of deployment for the same temperature are also included.

Figures 5 and 6 showed the simulated deployment characteristics of the actuators during deployment: the damping rate, the angular displacement, and the angular rate. These figures are used to predict the performance of the three actuators developed by HAC that will be used in the deployment of the 4-GHz transmit antenna, the 4-GHz transmit boom, and the 6-GHz receive boom/antenna assembly. (The actuator is designed to maintain full deployment, reduce the latch-up rate, and reduce the latch-up loads.) The NBOD2 program cannot calculate latch-up loads, although the necessary parameters are included in the program. This feature is currently under development at COMSAT. Actual latch-up loads, which were calculated and measured by HAC, were found to have only a nominal effect on the deployment mechanisms. Because of the complexity of the actuator design, latch-up load calculations are not performed here; although such calculations are important, their estimation is outside the scope of this effort. A close correlation of deployment times and latch-up velocities for reduced inertial loading (simulated mass and inertia were reduced to one-tenth) between life-test results, measured data, and simulation results can be found in Table 5. The results presented in Tables 4 and 5 demonstrate the accuracy of the simulation when compared with HAC test results obtained from engineering models.

### Conclusions

The usefulness of NBOD2 as a tool for modeling, analyzing, and troubleshooting possible problem areas in the deployment of INTELSAT VI spacecraft antennas has been demonstrated. The work presented here has

TABLE 4. INTELSAT VI 4- AND 6-GHZ ANTENNA/BOOM DEPLOYMENT RESULTS AT 72°F

INTELSAT VI 4-GHZ TRANSMIT DISH DEPLOYMENT			
TIME (s)	$\theta$ (deg)	$\dot{\theta}$ (rad/s)	$\ddot{\theta}$ (rad/s <sup>2</sup> )
0.45	0.75	0.066	0.167
4.0	67.20	0.564	0.114
8.0	174.0	0.067	0.075
12.0	181.8	0.029	0.00005
16.0	188.5	0.029	0.00005
20.0	195.3	0.029	0.00005
24.0	202.0	0.029	0.00005
28.0	208.7	0.029	0.00005
32.0	215.5	0.029	0.00005
36.0	223.9	0.030	0.00006
INTELSAT VI 4-GHZ TRANSMIT-BOOM DISH ASSEMBLY DEPLOYMENT			
TIME (s)	$\theta$ (deg)	$\dot{\theta}$ (rad/s)	$\ddot{\theta}$ (rad/s <sup>2</sup> )
0.90	4.3	0.147	0.10
3.0	34.0	0.235	0.005
6.0	72.2	0.128	0.117
9.0	81.5	0.031	0.004
12.0	86.5	0.028	0.0001
15.0	91.3	0.027	0.00006
18.0	96.1	0.027	0.00006
21.0	100.8	0.027	0.00006
24.0	105.5	0.027	0.00006
27.0	110.2	0.027	0.00006
30.0	114.9	0.027	0.00006
32.9	118.8	0.027	0.00006
*HAC 31.2		*HAC 0.024	
INTELSAT VI 6-GHZ RECEIVE-BOOM DISH ASSEMBLY DEPLOYMENT			
TIME (s)	$\theta$ (deg)	$\dot{\theta}$ (rad/s)	$\ddot{\theta}$ (rad/s <sup>2</sup> )
0.40	1.25	0.122	0.309
1.0	8.2	0.269	0.191
1.45	16.1	0.341	0.132
1.85	24.5	0.385	0.091
2.20	32.5	0.416	0.148
2.55	40.9	0.401	0.215
2.95	48.7	0.275	0.359
3.75	56.0	0.079	0.105
7.0	64.0	0.035	0.00067
11.1	72.0	0.033	0.00044
15.4	80.1	0.032	0.00014
18.0	84.8	0.032	0.00009
*HAC 18.2		*HAC 0.034	

\* Hughes Aerospace Corporation's life-test results.

TABLE 5. INTELSAT VI AMBIENT DEPLOYMENT WITH REDUCED INERTIA

ACTUATOR	DEPLOYMENT TIME (s)			LATCH-UP RATE (R/S)		
	SIMULATED*	MEASURED**	LIFE-TEST**	SIMULATED*	MEASURED	LIFE-TEST
Receive Boom	15.7	16.9	17.5	0.039	0.036	0.038
Transmit Boom	30.0	31.4	31.4	0.030	0.031	0.036
Transmit Dish	29.3	31.5	—	0.046	0.049	—

\* Actual inertia and mass are reduced to one-tenth.

\*\* The Honeywell Corporation performed the measured data tests; HAC performed the life tests.

established the predictability of the deployment systems and has demonstrated the use of NBOD2 as a significant tool in the final design of two deployment mechanisms. The first successful simulation of the viscous damped actuators used on the spacecraft has also been demonstrated here. Because of the modeling and design capability it represents, this effort is useful to the satellite industry in general.

NBOD2 was successfully used to model the INTELSAT V solar array deployment, whose basic configuration consists of connected solar panels and yoke. The program has also been used to model a direct-broadcast satellite solar-array deployment, whose configuration consists of connected solar panels attached to a long and short boom. This program will continue to be a viable tool in the analysis of dynamic systems.

### Acknowledgments

The author would like to thank J. Simpson and J. Hsing for their helpful discussions. The author also thanks B. Shatzer, who helped with the data, and others who contributed to this work.

### References

- [1] H. P. Frisch, "The NBOD2 User's and Programmer's Manual," NASA Technical Paper 1146, Cosmic Program GSC-12846, Vol. 1, February 1978.
- [2] G. Hofmann, Hughes Aerospace Corporation, private communication.

**Appendix A. Samples of the INTELSAT VI receive boom/antenna input and output data**

**NBOD2 input parameters**

The input parameters of the receive boom/antenna and the rigid platform of INTELSAT VI are given in the following program listing (INBS). Lines 1 through 21 represent typical input data that characterize the model (hence, the actual spacecraft members), which are necessary to run the program (Figure A-1).

The data described below correspond numerically to the line numbers in Figure A-1:

1. Logic flags that control the mode of data input/output.
2. The number of bodies in the input segment.
3. The body label and name.
4. The type of body (rigid), connecting hinge number, hinge degree of freedom representation (1), body mass.
5. } Representation of inertia tensor of the body.
6. }
7. }
8. }
9. } Representation of transformation matrix from spacecraft to local hinge coordinates.
10. }
11. Vector components that run from hinge to the body center of mass.
12. Vector components that run from hinge to hinge, which bound the body.
13. Free axis of the hinge about which motion can occur (the z axis).
14. One locked axis of the hinge about which motion is constrained (the y axis).  
(The second locked axis is computed internally.)
15. } Initial angular displacement.
16. } Initial angular rate of the body.
17. Translational degrees of freedom of body 1, (3—no motion allowed).
18. Number of momentum wheels modeled.
19. Integration step size, time to end the simulation (in seconds).
20. Optional code word (release one free vector).
21. Assigned free-vector number, free-vector release time (in seconds).

**Input torque listing**

The main portion of the input torque subroutine of the receive boom/antenna is shown in Figure A-2. The resulting hinge torque is given by the expression:

$$TOR = TSP + TDAMP - CT \tag{1}$$

where TSP = applied negator spring torque  
 TDAMP = damping torque  
 CT = resistive bearing/cable torque.

```

1  FFFFFFFFFFFFFFFF
2  3
   1  RIGID PLATFORM
   T  0  3  1044.5
   1458.4      0.0      36.27
   0.0      1501.3      0.0
   36.27      0.0      1496.0
   1.0      0.0      0.0
   0.0      1.0      0.0
   0.0      0.0      1.0
   0.0      0.0      0.0
   0.0      0.0      0.0
   1.0      0.0      0.0
   0.0      1.0      0.0
3  2  RECEIVE BOOM
4  T  1  2  7.04
5  1.1      -0.5      0.3
6  -0.5      5.02      -2.3
7  0.3      -2.3      3.94
8  .7071      0.0      -7071
9  0.0      1.0      0.0
10 .7071      0.0      .7071
11 -204      1.370      -767
12 -848      .270      -1.216
13 0.0      0.0      1.0
14 0.0      1.0      0.0
15 0.0      0.0      0.0
16 0.0      0.0      0.0
   3  RECEIVE DISH
   T  2  3  12.57
   3.72      0.3      -0.7
   0.3      3.04      -0.7
   -0.7      -0.7      6.73
   1.0      0.0      0.0
   0.0      1.0      0.0
   0.0      0.0      1.0
   -.0392      .0516      .1765
   -.2786      1.8757      -1.161
   1.0      0.0      0.0
   0.0      1.0      0.0
17 3
18 0
19 .05      20.0
20 CAGE      1
21 1      .05
END OPTIONS
    
```

Figure A-1. Sample Input Listing

The resulting torque, equation (1), is assigned to a body and to the axis about which motion is allowed to occur. The expression is

$$\text{PHI}(3,2) = \text{TOR}$$

where 3 represents the z axis and 2 represents body 2, the receive boom.

```

C      TSP(J)=SPRING TORQUE
C      DPC(J)=DAMPING CONST.
C      CT(J)=CABLE TORQUE
C      J=HINGE NO.
C
C      TSP=-29.76+2.1889*THA(1)+3.7823*THA(1)**2-5.9777*THA(1)**3
1      -3.8318*THA(1)**4
C      DPC=58.3D0
C      CT=-.68D0
C      IF(DABS(THA(1)) .GE. .44) GO TO 4
C      TOR=TSP-DPC*THAD(1)-CT
C
C      GO TO 6
C      4 THA1=-THA(1)*57.2958D0
C      DPC1=-630.90D0+35.920D0*THA1-0.39460D0*THA1**2
C      1+0.0014422*THA1**3
C      IF(DABS(THA(1)) .GE. 1.39626) DPC1=450.5+ .08*THA1
C      4 TDAMP=-DAMPC*THAD(1)
C      TOR=TSP+TDAMP-CT
C      6 CONTINUE
C      PHI(3,2)=TOR
C      IF(DABS(THA(1)) .GE. 1.48) TOR=0.0
C      PRINT 7,DPC
C      PRINT 8,DAMPC,SHRATE
C      PRINT 10,TSP,TOR
C      PRINT 12,TDAMP
C      7 FORMAT(4X,'DPC=',D13.6)
C      8 FORMAT(4X,'DAMPC=',D13.6,2X,'SHRATE=',D13.6)
C      10 FORMAT(4X,'TSP=',D13.6,2X,'TOR=',D13.6)
C      12 FORMAT(4X,'TDAMP=',D13.6)
C      IF(DABS(THA(1)) .GE. 1.48) THAD(1)=0.0
C      IF(DABS(THA(1)) .GE. 1.48) CT=0.0
C      RETURN
C      END

```

Figure A-2. Input Torque Listing

#### Output data sample

A sample of the receive boom/antenna general data output for each integration step is given Figure A-3. The body parameters are as follows:

ROMC,FOMC—angular velocity of system and local coordinates  
 ACC—angular acceleration  
 ETC,PHI—gyroscopic torque and resulting torque  
 CAC,CBC—Hinge to body center of mass position vector and position vector from hinge to hinge, bounding the body  
 XMC—vector transformation matrix

VEL—linear velocity of system coordinates  
 HB,LM—angular momentum and linear momentum  
 XIC—inertia tensor  
 TK—kinetic energy

Most of these parameters were calculated from the body's center of mass.

THA(1), THAD(1), THADD(1), and QFC(1)—hinge angular DISPLACEMENT( $\theta$ ), ANGULAR RATE ( $\dot{\theta}$ ), ANGULAR ACCELERATION( $\ddot{\theta}$ ), and the axis about which motion occurs (the z axis), respectively.

### Appendix B. General-purpose dynamics program

NBOD2 is a general-purpose dynamics program that could be applied to a broad class of problems. It may be used to both derive and give output in vector dynamic form, and/or to numerically solve equations of motion for any system that may be modeled, for dynamic simulation as a topological tree of point-connected rigid bodies, flexible bodies, point masses, and symmetric momentum wheels [1]. The program can be expanded or contracted according to the user's needs. An interrogation system was developed to screen input data by setting up a series of logic flags that determine computational options. With this system, a certain amount of engineering judgment may be applied.

#### Input/Output

Two segments must be dealt with while using the program—the input and the output. Samples of each, taken from the simulation program, are given in Appendix A. Provision for data input is allowed by three separate subroutines, which may be described as follows (in sequential order):

a. *INBS*. The format of this subroutine cannot be changed. The basic coupled rigid body, point mass, and symmetric wheel model is described. Data inputs are connection topology, degrees of freedom, mass, inertia, geometric parameters, relative body orientation, and initial kinematic conditions.

b. *INOPT*. The format of this subroutine is flexible. Available options may be invoked by selecting and inputting option code words. For the deployment simulation considered here, the code word "cage" was chosen. This option allows specified degrees of freedom to be released at a designated time during simulation. (Motion is allowed to occur about a gimbaled axis with a free vector assigned to it.)

c. *INTOR*. This subroutine is for the user. Data to be input to the torque and output subroutines are entered here. This subroutine may be left empty, or an existing input subroutine may be inserted and set up with proper interface statements, thus overriding the input data of the existing subroutine.





Paul K. James received a B.M.E. from the City College of the City University of New York and an M.M.E. from Howard University in 1975 and 1977, respectively. From 1977 to 1979, he worked as a research assistant while pursuing a Ph.D in mechanical engineering at Howard University. He joined COMSAT in 1980 as a member of the technical staff. He has participated in fuel-slosh analysis and was responsible for the mechanical design and fabrication of the single-axis flexible spacecraft simulator. Currently, he is involved in the dynamic analysis and testing of deployment mechanisms for INTELSAT VI, STC/DBS, and ARABSAT. Mr. James is an associate member of Sigma Xi, and a member of Tau Beta Pi and AAS.

## CTR Note

### Geostationary satellite log

C. H. SCHMITT

(Manuscript received February 27, 1985)

This note provides lists of current and future geostationary satellites for the Fixed Satellite Service (FSS), the Maritime Mobile Satellite Service (MMSS), and the Broadcasting Satellite Service (BSS). Satellites in the Space Research Service (SRS) are listed only when their frequencies overlap those of satellites in the other services. Future satellites are listed when information has been published by the International Frequency Registration Board (IFRB), or when satellite construction has commenced. The lists are ordered along increasing East longitude orbit position and update the previously published material [1] through December 1984.

Table 1 lists the satellites that are operating as of late December 1984, or satellites that may be capable of operating. Satellites being moved to new orbital positions are shown at their planned final positions for 1985, unless another satellite occupies the position. Refer to the Remarks column for further information.

Table 2 lists newly proposed and replacement satellites and their currently planned orbital positions. Additional technical characteristics may be found in the IFRB circulars referenced, as published weekly in the circular's special sections [2] or obtained from the country or organization given.

---

*Carl H. Schmitt is an Assistant to the Director for Communications on the Staff of the Division Director, Engineering and System Integration, System Technology Service, COMSAT General Corporation.*

Table 3 is the key to the frequency bands used in Tables 1 and 2. Sub-band allocations are designated in the Up/Down-Link Frequency column of Tables 1 and 2 by the letter suffix given that sub-band in Column 1 of Table 3. Thus, 12a implies 11.7 to 12.2 GHz, down-link in Region 2. Table 3 also shows the service allocations and the applicable ITU region when the band is not allocated worldwide.

The author invites inquiries and comments, and would appreciate receiving information on newly planned satellite networks as they become available.

### References

- [1] C. H. Schmitt, "Geosynchronous Satellite Log," *COMSAT Technical Review*, Vol. 13, No. 1, Spring 1984, pp. 169-189.
- [2] *IFRB Circulars*, AR11/A/ or /C/ and SPA/AA/ or /AJ/, The International Telecommunications Union IFRB, CH 1211, Geneva 20, Switzerland.

TABLE 1. IN-ORBIT GEOSTATIONARY SATELLITES FOR FIXED, BROADCAST, AND MARITIME-MOBILE SERVICES, LATE DECEMBER 1984

Subsatellite Longitude*	Launch Date	Satellite Designation	Country or Organization	Function	Up/Down-Link Frequency (GHz)	Remarks
5.7°E	11 May 1978	OTS 2	ESA	FSS, BSS	14/11	Experimental, IFRB: 5°E
12.9°E	16 Jun 1983	EUTELSAT 1 (formerly ECS-1)	EUTELSAT-ESA	FSS	14/11	Designated ECS 1 before acceptance by EUTELSAT IFRB: 10° & 13°E
36.9°E	26 Nov 1982	RADUGA 11	USSR	FSS	6/4	IFRB: 35°E
36.9°E	25 Aug 1983	RADUGA 13	USSR	FSS	6/4	IFRB: 35°E
40.1°E	28 Dec 1979	GORIZONT 3	USSR	FSS	6.8/4.7	IFRB: 40°E
53°E	15 Mar 1982	GORIZONT 5 (STATIONAR 5)	USSR	FSS	6.8/4.7	IFRB: 53°E
57°E	23 May 1981	INTELSAT V (F-1) IND 3	INTELSAT	FSS	6.14/4.11	Indian Ocean Region--Spare IFRB: 57°E
60°E	19 Oct 1983	INTELSAT V (F-7) MCS-C IND C	INTELSAT INMARSAT Lease	FSS MNSS	6.14/4.11 1.6b, 6.4b /1.5a, 4	Indian Ocean Region--Spare IFRB: 60°E; INMARSAT Spare IFRB: 60°E
61.8°E	26 Dec 1980	EKRAN 6	USSR	BSS	6/UHF	Drifting 0.15°E per day on 12/21
62.9°E	28 Sep 1982	INTELSAT V (F-5) MCS-A	INTELSAT INMARSAT Lease	FSS MNSS	6.14/4.11 1.6b, 6.4b/ 1.5a, 4f	Indian Ocean Region--Maj. Path IFRB: 63°E Maritime Comm. sys. operational IFRB: 63°E
63.3°E	20 Feb 1980	RADUGA 6	USSR	FSS	6/4	On 12/21/84 drifting 25°W per day
64.7°E	25 Aug 1977	SIRIO 1	Italy	Experimental	UHF, 17/12b, UHF	Experimental--17/12b transponder to be shut off; satellite to be drifted to 75°E in 1st Qtr. of 1985 IFRB: 65°E in coordination

TABLE 1 (continued). IN-ORBIT GEOSTATIONARY SATELLITES FOR FIXED, BROADCAST,  
AND MARITIME-MOBILE SERVICES, LATE DECEMBER 1984

Subsatellite Longitude*	Launch Date	Satellite Designation	Country or Organization	Function	Up/Down-Link Frequency (GHz)	Remarks
72.5°E	10 Jun 1976	MARISAT 2	US-COMSAT General	MMS	UHF, 1.6b, 6.4c UHF 1.5a, 4.1b	Operational, but unused except for UHF transponder IFRB: 72.5°E
73.3°E	08 Apr 1983	RADUGA 12	USSR	FSS	6/4	
73.4°E	30 Aug 1983	INSAT 1B	India	FSS	6/4	IFRB: 74°E (INSAT 1A)
77°E	13 Mar 1977	PALAPA A-2	Indonesia	FSS	6/4	Backup for PALAPA B-1 IFRB: 77°E
79.1°E	01 Aug 1984	GORIZONT 10	USSR	FSS	6, 8/4, 7	
81.2°E	15 Feb 1984	RADUGA 14	USSR	FSS	6/4	Drifting 0.14°E per day on 12/24; IFRB: 80°E
83.1°E	08 Jul 1976	PALAPA A-1	Indonesia	FSS	6/4	Near retirement; IFRB: 83°E
85.8°E	09 Oct 1981	RADUGA 10	USSR	FSS	6/4	IFRB: 85°E (STATSIONAR 3)
88.1°E	30 Nov 1983	GORIZONT 8	USSR	FSS	6, 8/4, 7	IFRB: 90°E (STATSIONAR 6)
89.5°E	20 Oct 1982	GORIZONT 6	USSR	FSS	6, 8/4, 7	IFRB: 90°E (STATSIONAR 6)
92.4°E	30 Sep 1983	EKRAN 11	USSR	BSS	6/UHF	Drifting 2.4°E per day
96.3°E	26 Jun 1981	EKRAN 7	USSR	BSS	6/UHF	
101.3°E	24 Aug 1984	EKRAN 13	USSR	BSS	6/UHF	
102.3°E	12 Mar 1983	EKRAN 10	USSR	BSS	6/UHF	
103.3°E	15 Dec 1977	SAKURA (C.S.)	Japan-NTT	FSS	6, 30a/4, 20a	Experimental
107.3°E	18 Jun 1983	PALAPA B-1	Indonesia	FSS	6/4	Domestic and regional planned final 1985 location IFRB: 108°E
110°E	18 Jul 1978	RADUGA 4 and NASDA	USSR	FSS	6/4	
123.5°E	23 Jan 1984	BS 2A	Japan	BSS	2, 14/12b, 2	

136.1°E	05 Aug 1983	CS 2B	Japan	FSS	6, 30a/4, 20a	IFRB: 136°E
174°E	31 Mar 1978	INTELSAT IV-A (P-6)	INTELSAT	FSS	6/4	Pacific Ocean Region--Primary IFRB: 174°E
176.3°E	14 Oct 1976	MARISAT 3 (P-2)	US-COMSAT General	MMS	UHF, 1.6b, 6.4c/ UHF, 1.5a, 4.1b	Becomes spare for INMARSAT on 1 Jan 1985; also carries UHF capability; IFRB: 176.5°E
177.5°E	10 Nov 1984	MARECS B2	ESA-leased to INMARSAT	MMS	1.6b, 6.4e/1.5a, 4	Operational 1 Jan 1985 as Pacific Ocean Maritime Satellite IFRB: 177.5°E in coordination
179°E	07 Jan 1978	INTELSAT IV-A (P-3)	INTELSAT	FSS	6/4	Pacific Ocean Region--Spare IFRB: 179°E
217.1°E (142.9°W)	28 Oct 1982	SATCOM V (P-5)	US-Alascom, Inc.	FSS	6/4	IFRB: 143°W in coordination
220.9°E (139.1°W)	11 Apr 1983	SATCOM IR	US-RCA	FSS	6/4	IFRB: 139°W in coordination
226°E (134°W)	28 Jun 1983	GALAXY 1	US-Hughes Comm.	FSS	6/4	IFRB: 134°W adv. publication
229°E (131°W)	21 Nov 1981	SATCOM IIIR (P-3R)	US-RCA	FSS	6/4	IFRB: 131°W in coordination
232.9°E (127.1°W)	21 Feb 1981	COMSTAR D-4	US-COMSAT General	FSS	6/4	IFRB: 127°W adv. publication
236.5°E (123.5°W)	09 Jun 1982	WESTAR 5	US-Western Union	FSS	6/4	IFRB: 123.5°W
240°W (120°)	23 May 1984	SPACENET I	US-GTE Spacenet	FSS	6/14/4, 12a	IFRB: 119°W
242.5°E (117.5°W)	12 Nov 1982	ANIK C3 (E)	Canada-TELESAT	FSS	14/12a	IFRB: 117.5°W
251°E (109°W)	16 Dec 1978	ANIK B1 (4)	Canada-TELESAT	FSS	6, 14/4, 12a	IFRB: 109°W
254.7°E (105.3°W)	05 Nov 1967	ATS 3	US-NASA	Experimental	UHF, 6/UHF, 7, 4	IFRB: 86°W
255°E (105°W)	18 Jun 1983	ANIK C2	Canada-TELESAT	FSS	14/12a	Temporary--to be moved by 1 July 1985

TABLE I (continued). IN-ORBIT GEOSTATIONARY SATELLITES FOR FIXED, BROADCAST,  
AND MARITIME-MOBILE SERVICES, LATE DECEMBER 1984

Subsatellite Longitude*	Launch Date	Satellite Designation	Country or Organization	Function	Up/Down-Link Frequency (GHz)	Remarks
255.5°E (104.5°W)	26 Aug 1982	ANIK D1	Canada-TELESAT	FSS	6/4	IFRB: 104.5°W
259°E (101°W)	30 Aug 1984	SBS 4	US-Satellite Business Systems	FSS	14/12a	Operational, but temporary location for up to 2 years
261°E (99°W)	15 Nov 1980	SBS 1	US-Satellite Business Systems	FSS	14/12a	Located at 99.08°W
261°E (99°W)	26 Feb 1982	WESTAR 4	US-Western Union	FSS	6/4	IFRB: 99°W adv. publication
263°E (97°W)	24 Sep 1981	SBS 2	US-Satellite Business Systems	FSS	14/12a	IFRB: 97°W in coordination USASAT 6A
264°E (96°W)	28 Jul 1983	TELSTAR 301 (3A)	US-AT&T	FSS	6/4	IFRB: 95°W in coordination
265°E (95°W)	11 Nov 1982	SBS 3	US-Satellite Business Systems	FSS	14/12a	IFRB: 95°W in coordination USASAT 6C
266.5°E (93.5°W)	21 Sep 1984	GALAXY III	US-Hughes Comm.	FSS	6/4	IFRB: 93.5°W adv. publication USASAT 12B
269°E (91°W)	10 Aug 1979	WESTAR 3	US-Western Union	FSS	6/4	IFRB: 91°W
274°E (86°W)	01 Sep 1984	TELSTAR 302	US-AT&T	FSS	6/4	IFRB: 86°W in coordination USASAT 3C
277°E (83°W)	16 Jan 1982	SATCOM IV	US-RCA	FSS	6/4	IFRB: 83°W in coordination
281°E (79°W)	10 Oct 1974	WESTAR 2	US-Western Union	FSS	6/4	IFRB: 79°W adv. publication USASAT 12A
283.8°E (76.2°W)	22 Jul 1976	COMSTAR D2	US-COMSAT General	FSS	6/4	Collocated for operational reasons; IFRB: 76°W adv. pub.
284°E (76°W)	29 Jun 1978	COMSTAR D3	US-COMSAT General	FSS	6/4	Collocated for operational reasons; IFRB: 76°W adv. pub.
286°E (74.0°W)	22 Sep 1983	GALAXY 2	US-Hughes Comm.	FSS	6/4	IFRB: 74°W adv. publication USASAT 7A
288°E (72°W)	08 Sep 1983	SATCOM IIR (VII)	US-RCA	FSS	6/4	Operational 29 Nov 1983 IFRB: 72°W in coordination USASAT 8B
291°E (69°W)	23 May 1984	SPACENET II	US-GTE Spacenet	FSS	6,14/4,12a	
307°E (53°W)	03 Mar 1984	INTELSAT V (P-8)	INTELSAT	FSS	6,14/4,11	Atlantic Ocean Region--Spare IFRB: 50°W in coordination
310.2°E (49.8°W)	22 May 1975	INTELSAT IV	INTELSAT (P-1)	FSS	6/4	Atlantic Ocean Region--Spare IFRB: 5°W in coordination
317.2°E (42.8°W)	05 Apr 1983	TDRS East	US-NASA US-Systematics Gen.	SRS FSS	1,14d/2.2,13a 6/4	IFRB: 41°W
335.5°E (24.5°W)	15 Dec 1981	INTELSAT V (P-3)	INTELSAT	FSS	6,14/4,11	Atlantic Ocean Region--Primary IFRB: 24.5°W
335.7°E (24.3°W)	05 Oct 1980	RADUGA 7	USSR (STATSIONAR 8)	FSS	5,6/3	Operates below INTELSAT V frequencies; IFRB: 25°W
338.5°E (21.5°W)	25 May 1977	INTELSAT IV-A (P-4) ATL 1	INTELSAT	FSS	6/4	Atlantic Ocean Region--Spare IFRB: 21.5°W
341.6°E (18.4°W)	19 May 1983	INTELSAT V (P-6)	INTELSAT INMARSAT Lease	FSS MMSS	6,14/4,11 1,6b,6.4b/1.5a, 4g	Atlantic Ocean Region--Maj. Path 2. IFRB: 18.5°W MCS B is a spare for MARECS A
345.3°E (14.7°W)	19 Feb 1976	MARISAT 1	US-COMSAT General	MMSS	UHF 1,6b,6.4c/ UHF 1,5a,4.1b	Operational, but only UHF transponder is used IFRB: 15°W
349.6°E (10.4°W)	14 Jun 1980	GORIZONT 4 STATSIONAR 11	USSR	FSS	6,8/4,7	IFRB: 11°W in coordination
352°E (8°W)	04 Aug 1984	TELECOM 1A	France	FSS	2,6,8,14/2.2,4, 7,12b,12d	28°E on 12/24 drifting 0.44°W per day IFRB: 8°W
356.2°E (3.8°W)	29 Jan 1976	INTELSAT IV A (P-2) ATL 1	INTELSAT	FSS	6/4	Atlantic Ocean Region--Spare IFRB: 4°W in coordination
359°E (1°W)	21 Nov 1974	INTELSAT IV (P-8)	INTELSAT	FSS	6/4	Atlantic Ocean Region--Spare IFRB: 1°W

\*The list of satellite longitudes was compiled from the best information available.

TABLE 2 PLANNED GEOSTATIONARY SATELLITES FOR FIXED, BROADCAST,  
AND MARITIME-MOBILE SERVICES, LATE DECEMBER 1984

Subsatellite Longitude	Launch Date	Satellite Designation	Country or Organization	Function	Up/Down-Link Frequency (GHz)	Remarks
1°E	1985	GDL 5	Luxembourg	FSS/BSS		
3°E	1985	TELECOM 1C	France	FSS/BSS <sup>a</sup>	2,6,8,14/2.2,4,7,12b,12d	AR11/A/29/1339 AR11/C/116 ADD-2 AR11/C/157/1598 AR11/C/131/1594
5°E	1985-86	TELE-X	Norway, Sweden	FSS/BSS	2,6,30a,17a/2,12b,20,	AR11/A/27/1535
7°E	1984-85	EUTELSAT I-3	France	FSS/BSS	14/11,12b,12d	AR11/A/59/1578
7°E	1987	F-SAT 1	France	FSS	2,14,30a/12d,20a	AR11/C/568/1649 AR11/A/79/1587
10°E	1985	EUTELSAT I	France (Spare)	FSS/BSS	14/11,12b,12d	AR11/A/61/1578 AR11/A/60ADD-3
10°E	1986	APEX	France	BSS/FSS	6,30a/2,4,20a,39a,49a	AR11/C/1583-584/1651 AR11/A/62/1578
12°E	Unknown	PROGNOZ 2	USSR	SRS	-/3,4	SPA-AA/317/1471
13°E	31 Dec 1987	ITALSAT	Italy	FSS	30/2,20,39a,49a	AR11/A/151/1633
13°E	1984-85	EUTELSAT I-2	France	FSS/BSS	14/11,12b,12d	SPA-AJ/328/1492 AR11/A/61/1578 & 1589 & 1582
14°E	Unknown	Nigerian National System	Nigeria	FSS	6/4	SPA-AA/2091346
15°E	1986	AMS 1	Israel	FSS	6,14/4,11	AR11/A/39/1554 AR11/B/301593

15°E	1986	AMS 2	Israel	FSS	6,14/4,11	AR11/A/39/1554
16°E	1987	SICRAL 1A	Italy	FSS	8,14b,43a/7,12d,20,44	AR11/A/44/1588
17°E	Unknown	SABS	Saudi Arabia	BSS	14/12b	SPA-AA/235/1387
17°E	1988	SABS 1-2	Saudi Arabia	BSS	14a,14/12b	AR11/A/125/1616
19°E	1985	GDL 6	Luxembourg	FSS,BSS	6.5-7,14/11,12d	AR11/A/94/1594
19°E	1985	ARABSAT I	Arab League	FSS/BSS	6/4,2.5	SPA-AJ/172/1388 RES-33/C/1597
20°E	Unknown	Nigerian National System	Nigeria	FSS	6/4	SPA-AA/209/1346
22°E	1987	SICRAL 1B	Italy	MMSS/FSS	UHF,8,14,43a/7,12d,20	AR11/A/45/1557 AR11/A/45/1588
23.5°E	1987	DFS 1	Germany	FSS	2,14,30a/11,12d,20,3D	AR11/A/40/1556
26.°E	1985	ARABSAT II	Arab League	FSS/BSS	6/4,2.5	SPA-AJ/173/1388 RES 33/C/2/1597
26°E	Unknown	ZOHREH 2	Iran	FSS	14/11	SPA-AA/164/1278 SPA-AJ/76/1303
28.5°E	1987	DFS 2	Germany	FSS	2,14,30a/11,12d,20a,30	AR11/A/41/1556
32°E	1987/10	VIDEOSAT 1	France	FSS	14/2,12d	AR11/A/80/1588
34°E	Unknown	ZOHREH 1	Iran	FSS	14/11	SPA-AA/163/1278
35°E	Unknown	PROGNOZ 3	USSR	SRS	-/3,4	SPA-AA/318/1471
38°E	1986	PAKSAT 1	Pakistan	FSS	14/11,12d	AR11/A/90/1592
40°E	Unknown	STATSIONAR 12	USSR	FSS	6/3	SPA-AA/271/1425 SPA-AJ/304/1469

TABLE 2 (continued). PLANNED GEOSTATIONARY SATELLITES FOR FIXED, BROADCAST,  
AND MARITIME-MOBILE SERVICES, LATE DECEMBER 1984

Subsatellite Longitude	Launch Date	Satellite Designation	Country or Organization	Function	Up/Down-Link Frequency (GHz)	Remarks
41°E	Unknown	ZOHREH 4	Iran	FSS	14/11	SPA-AA/203/1330
41°E	1986	PAKSAT 2	Pakistan	FSS	14/12d	AR11/A/91/1592
45°E	Unknown	VOLNA 3	USSR	MMSS	UHF, 1.6b/1.5a, UHF	SPA-AA/274/1425
45°E	Unknown	LOUTCH P2	USSR	FSS	14/11	SPA-AA/178/1289 SPA-AJ/122/1340
45°E	Unknown	STATIONAR 9	USSR	FSS	6/4	SPA-AJ/51/1276
47°E	Unknown	ZOHREH 3	Iran	FSS	14/11	SPA-AA/165/1278
53°E	Unknown	LOUTCH 2	USSR	FSS	14/11	SPA-AJ/85/1318 Leased to Intersputnik
57°E	1988	INTELSAT VI (IND 2)	INTELSAT	FSS	5, 6 14/3, 4, 11	AR11/A/72/1584
57°E	1985	INTELSAT V-A (IND 2)	INTELSAT	FSS	6, 14/4, 11	AR11/A/68/1580
60°E	1986	INTELSAT V-A (IND 1)	INTELSAT	FSS	6, 14/4, 11	AR11/A/67/1580
60°E	1988	INTELSAT VI (IND 1)	INTELSAT	FSS	5, 6, 14/3, 4, 11	AR11/A/71/1584
64.5°E	Unknown	MARECS (IND 1)	INMARSAT (F)	MMSS	1.6b, 6.4e/1.5a, 4f	SPA-AJ/243/1432
64.5°E	1989	INMARSAT IOR	INMARSAT (G)	MMSS	1.6b, 6.4b/1.5a, 3.9b, 4c, 3.6a	AR11/A/178/1644
66°E	1984	INTELSAT IV-A (IND 1)	INTELSAT	FSS	6/4	SPA-AA/82/1182 SPA-AA/52/1162
66°E	1986	INTELSAT V (IND 4)	INTELSAT	FSS	6, 14/4, 11	SPA-AA/253/1419
66°E	1987	INTELSAT MCS (IND D-Spare)	INTELSAT	MMSS	1.6b, 6.4b, /1.5a, 4f	SPA-AA/275/1425
66°E	1989	INTELSAT V-A (66E)	INTELSAT	FSS	6, 14/4, 11	
70°E	Unknown	STW 2	China, Peoples Republic of	FSS	6/4	SPA-AA/142/1255
73°E	Unknown	MARECS (IND 2)	INMARSAT (F)	MMSS	1.6b, 6.4e, /1.5a, 4f	AR11/D/3/1551
80°E	Unknown	STATIONAR 13	USSR	FSS	6/4	SPA-AA/276/1426 SPA-AJ/305/1469
80°E	Unknown	POZOK 2	USSR	FSS	6/4	AR11/A/179/1645 SPA-AA/345/1485
85°E	Unknown	LOUTCH P3	USSR	FSS	14/11	SPA-AA/179/1289 SPA-AJ/123/1340
85°E	Unknown	VOLNA 5	USSR	MMSS	UHF, 1.6b/1.5a, UHF	SPA-AJ/100/1329 SPA-AA/173/1286
90°E	Unknown	LOUTCH 3	USSR	FSS	14/11	SPA-AJ/86/1318
90°E	Unknown	VOLNA 8	USSR	MMSS	UHF, 1.6b/1.5a, UHF	SPA-AA/289/1445 AR11/C/15/1589
93°E	1986	INSAT 1B	India	FSS	6/4	SPA-AJ/231/1429 Since INSAT 1B is in orbit, this will be INSAT 1C
95°E	1985	CSDRN	USSR	SRS	14d/10, 11, 13	SPA-AA/342/1484
95°E		STATIONAR 14	USSR			

TABLE 2 (continued). PLANNED GEOSTATIONARY SATELLITES FOR FIXED, BROADCAST, AND MARITIME-MOBILE SERVICES, LATE DECEMBER 1984

Subsatellite Longitude	Launch Date	Satellite Designation	Country or Organization	Function	Up/Down-Link Frequency (GHz)	Remarks
99°E	Unknown	STATSIONAR T	USSR	FSS/BSS	6/UHF	RES-SPA2-3-AA10/1426 SPA-AJ/316/1473
99°E	Unknown	STATSIONAR T2	USSR	FSS/BSS	6/UHF	SPA-AJ/316/1473
110°E	Unknown	BSE	Japan TCSJ	BSS	2,14/	SPA-AA/305/1459 AR11/C/10/1556
110°E	1985	BS 2	Japan	BSS	2,14/12b,2	Spare in orbit
113°E	Unknown	PALAPA B-2	Indonesia	FSS	6/4	SPA-AA/198/1319 SPA-AJ/201/1407
118°E	1988	PALAPA B-3	Indonesia	FSS	6/4	AR11/A/157/1637
125°E	1985	STW 1	China, Peoples Republic of	FSS	6/4	SPA-AJ/240/1431
128°E	1984	STATSIONAR 15	USSR	FSS	6/4	SPA-AA/273/1425 SPA-AJ/307/1469
128°E		VOLNA 9	USSR	FSS/BSS		UHF, 1.60/1.5a, UHF
130°E	Unknown	ETS 2	Japan	Experimental		
132°E	Unknown	CS 2A	Japan	FSS	2,6,30a/4,2,20a	SPA-AA/256/1421 SPA-AJ/323/1490
140°E	Unknown	LOUTCH 4	USSR	FSS	14/11	SPA-AJ/87/1318
140°E	Unknown	STATSIONAR 7	USSR	FSS	6/4	SPA-AJ/31/1251
140°E	Unknown	VOLNA 6	USSR	FSS/BSS	3	
145°E	1987	STATSIONAR 16	USSR	FSS	6/4	AR11/A/76/1593 & 1586
150°E	Unknown	CSE	Japan	FSS	14/12a	AR533/6/3/1639 AR533/6/3/164, AR11/C/177/1606
156°E	1985	AUSSAT 1	Australia (OTC)	FSS/BSS	14/12b,12d	RES SPA2-3/AA/12/1456, 15/1575, SPA-AA/372/1575
160°E	1985	AUSSAT 2	Australia (OTC)	FSS/BSS	14/12b,12d	RES SPA2-3/AA/13/1456, 16/1575, SPA-AA/373/1575, RES33/B/1/1583 RES33/C/5/1673 RES33/G/5/1647
164°E	1985	AUSSAT 3	Australia (OTC)	FSS/BSS	14/12b,12d	RES SPA2-3/AA/14/1456, 17/1575, SPA-AA/374/1575
173°E	Feb 1986	INTELSAT V (PAC 1)	INTELSAT	FSS	6,14/4,11	AR11/C/170/1600; may move to 174°E
173°E	1988-89	INTELSAT V-A (PAC 1)	INTELSAT	FSS	6,14/4,11	AR11/A/65/1580; may move to 174°E
176°E	1986	INTELSAT V (PAC 2)	INTELSAT	FSS	6,14/4,11	AR11/A/81/1588 SPA-AA/255/1419
176°E	1987	INTELSAT V-A (PAC 2)	INTELSAT	FSS	6/14/4,11	AR11/A/66/1580
179°E	Sep 1985	INTELSAT V (PAC 2)	INTELSAT	FSS	6,14/4,11	SPA-AJ/377/1511
179°E	1986	INTELSAT MCS (PAC A)	INTELSAT	MMSS	1.6b, 6/1.5a,4	SPA-AJ/477/1577 SPA-AA/332/1476
179°E	1991	INTELSAT V-A (PAC 3)	INTELSAT	FSS	6,14/4,11	Could be INTELSAT V IBS at 180°E

TABLE 2 (continued). PLANNED GEOSTATIONARY SATELLITES FOR FIXED, BROADCAST,  
AND MARITIME-MOBILE SERVICES, LATE DECEMBER 1984

Subsatellite Longitude	Launch Date	Satellite Designation	Country or organization	Function	Up/Down-Link Frequency (GHz)	Remarks
189°E (171°W)	1985	TDRS WEST	USA-NASA/SPACECOM	SRS	2,14d/2.2,13	SPA-AA/232/1381 AR11/C/47/1568 See FCC filing
190°E (170°W)	Unknown	LOUTCH P4	USSR	FSS	14/11	SPA-AA/180/1289 SPA-AJ/124/1340
190°E (170°W)	Unknown	STATSIONAR 10	USSR	FSS	6/4	SPA-AJ/64/1280
190°E (170°W)	Unknown	VOLNA 7	USSR	MMSS	UHF,1.6b/1.5a,UHF	SPA-AA/175/1286
192°E (168°W)	Unknown	POTOK 3	USSR	FSS	6/4	SPA-AA/346/1485
200°E (160°W)	1985	ESDRN	USSR	SRS	14d/10,11,13	SPA-AA/343/1484
214°E (146°W)	1985	AMIGO 2	Mexico	BSS	17a/12b	RES 33/A/2/1560
215°E (145°W)	Unknown	ILHUICAHUA 4	Mexico	FSS	6,14/4,12a	AR11/A/25/1533
219°E (141°W)	Unknown	ILHUICAHUA 3	Mexico	FSS	6,14/4,12a	AR11/A/24,1533
218°E (132°W)	1987	USASAT 11C	USA	FSS	14/12a	AR11/111/1609
128°E (132°W)	Unknown	US SATCOM 3	USA	FSS	6/4	SPA-AA/247/1412
230°E (130°W)	31 Dec 1987/10 <sup>b</sup>	USRDS West	USA	FSS/RDSC <sup>c</sup>	1.6a,6.5a/2.4, 5/1a	AR11/A/176/1641

234°E (126°W)	15 Sep 1987/10 10C	USASAT	USA	FSS	14/12a	AR11/A/107/1609
236°E (124°W)	15 Sep 1986/10	USASAT 10B	USA	FSS	14/12a	AR11/A/106/1609
240°E (120°W)	15 Jan 1987	USASAT 10A	USA	FSS	14/12a	AR11/105/1609
243.5°E (116.5°W)	1985	MORELOS II	Mexico	FSS	6,14/4,12a	AR11/A/30/1540
246°E (114°W)	Unknown	TELESAT D2 (ANIK)	Canada-TELESAT	FSS	6/4	SPA-AA/358/1500
247.5°E (112.5°W)	1985 <sup>d</sup>	ANIK C2	Canada-TELESAT	FSS	14/12a	May be moved to 110°W ANIK C2 temporarily at 105°W, AR11/C/3/1554
251°E (109°W)	Unknown (see remarks)	TELESAT C3	Canada-TELESAT	FSS	14/12a	Presently in orbit at 112.5°W
252.5°E (107.5°W)	1985	ANIK C1	Canada-TELESAT	FSS	14/12a	Launch scheduled Apr 1985
253.5°E (106.5°)	1987	MSAT	Canada	FSS/MMSS	UHF-EHF/UHF-EHF	AR11/A/55/1563
254°E (106°W)	1985	GSTAR I	US-GTE Satellite	FSS	14/12a	AR11/A/14/1525, AR11/A/14ADD-1/1548
257°E (103°W)	1986	GSTAR II	US-GTE Satellite	FSS	14/12a	AR11/A/15/1525, AR11/A/15ADD-1/1548
260°E (100°W)	30 Sep 1987/10	USRDS Central	USA	FSS/RDS	1.6a,6.5a/2.4, 5.1a	AR11/A/175/1641
265°E (95°W)	1984	USASAT 6C	USA	FSS	14/12a	AR11/A/35/1553

TABLE 2 (continued). PLANNED GEOSTATIONARY SATELLITES FOR FIXED, BROADCAST,  
AND MARITIME-MOBILE SERVICES, LATE DECEMBER 1984

Subsatellite Longitude	Launch Date	Satellite Designation	Country or Organization	Function	Up/Down-Link Frequency (GHz)	Remarks
269°E (91°W)	20 Dec 1985	WESTAR VI-S	US-Western Union	FSS	6/4	Will replace WESTAR III which will move to 79°W: WESTAR II will be retired in early 1986
273°E (87°W)	14 Oct 1985 15 Jun 1985/10	SATCOM K-1 (USASAT 9B)	US-RCA USA	FSS	14/12a	Under construction AR11/A/102
274°E (86°W)	1985	USASAT 3C	USA	FSS	6/4	AR11/C/246
275°E (85°W)	15 Mar 1987/10	USASAT 9C	USA	FSS	14/12a	AR11/A/103/1609
277°E (83°W)	1988	STSC 1	Cuba	FSS	6/4	AR11/A/58/1578. Note 83°W occupied by USASAT 7B or SATCOM IV
279°E (81°W)	Dec 1986	USASAT 7D	USA	FSS	6,14/4,12a	AR11/C/50/1568: was 79°W AR11/A/12/1525 AR11/C/257/1623
281°E (79°W)	1985	TDRS Central	USA-NASA/SPACECOM USA-Systemat. Gen.	SRS FSS	2,14d/2.2,13a 6/4	SPA-AA/233/1381
281°E (79°W)	15 Mar 1987	USASAT 11A	USA	FSS	14/12a	AR11/A/109/1609
283°E (77°W)	15 Jun 1987/10 27 Nov 1985	USASAT 11B (SATCOM K-2)	USA RCA	FSS	14/12a	AR11/A/110/1609 Under construction
284.6E (75.4°W)	1986 1986	SATCOL 1A SATCOL 1B	Colombia Colombia	FSS FSS	6/4 6/4	SPA-AA/322,323/1474 AR11/C/19/1573
285°E (75°W)	1986	SATCOL 2	Colombia	FSS	6/4	SPA-AJ/127/1343

290°E (70°W)	1st half of 1985/10	SBTS A-1	Brazil	FSS	6/4	AR11/A/16/1526, origin AR11/A/16/1526 AR11/C/94/1576
290°E (70°W)	1985	USASAT 7C	USA	FSS	6/4	AR11/A/1525
290°E (70°W)	30 Jun 1987/10	USRDS East	USA	FSS/RDS	1.6a,6.5a/2.4, 5.1a	AR11/A/174/1641
293°E (67°W)	01 Jan 1986/10	USASAT 8A	USA	FSS	6/4	AR11/C/394/1629, A/36/1553
294°E (66°W)	30 June 1989	USASAT 15D	USA	FSS	14/12a	AR11/A/165
295°E (65°W)	1985	SBTS A-2	Brazil	FSS	6/4	AR11 /A/17/1526
296°E (64°W)	1988	USASAT 15C	USA	FSS	14/12a	AR11/A/
297°E (63°W)	1986	USASAT 14D	USA	FSS	6/4	AR11/C/99/1576, confirm AR11/A/37/1553
298°E (62°W)	1988/10	USASAT 15B	USA	FSS	14/11.12a	AR11/A/163/1637
299°E (61°W)	1989/10	USASAT 14C	USA	FSS	6/4	AR11/A/160/1637
300°E (60°W)	31 Dec 1988/10	USASAT 15A	USA	FSS	14/12a	AR11/A/162/1637
300°E (60°W)	01 Jan 1986/10	INTELSAT IBS (300E)	INTELSAT	FSS	5c-6,14/4a,11d, 11f,12d,	AR11/A/167/1638
302°E (58°W)	1987	USASAT 8C	USA	FSS	6/4,10.7-12.744 11.7-12.2	AR11/A/38/1553
302°E (58°W)	30 Jul 1988/10	USASAT 13E	USA	FSS-Intern	14/11.12a,12b,12c	AR11/A/136/1620

TABLE 2 (continued). PLANNED GEOSTATIONARY SATELLITES FOR FIXED, BROADCAST,  
AND MARITIME-MOBILE SERVICES, LATE DECEMBER 1984

Subsatellite Longitude	Launch Date	Satellite Designation	Country or Organization	Function	Up/Down-Link Frequency (GHz)	Remarks
303°E (57°W)	30 Sep 1987/10	USASAT 13H	USA	FSS	5c-6/4,11b	AR11/A/177/1643
304°E (56°W)	30 Jul 1988/10	USASAT 13D	USA	FSS	6/4	AR11/C/246/1620
304°E (56°W)	01 Apr 1986/10	INTELSAT V-A (304E)	INTELSAT	FSS	6,14/4,11	AR11/A/168/1638
304°E (56°W)	01 Apr 1986/10	INTELSAT IBS (304E)	INTELSAT	FSS	5c-6,14/4a,11d, 11f,12d	AR11/A/169/1638
305°E (55°W)	31 Dec 1988/10	USASAT 14B	USA	FSS	6/4	AR11/A/159/1637
307°E (53°W)	1986 <sup>e</sup>	INTELSAT V (CONT 1)	INTELSAT	FSS	6,14/4,11	AR11/A/82/1588
307°E (53°W)	1986 <sup>e</sup>	INTELSAT IBS (307E)	INTELSAT	FSS	6,14,14b/4,11,12a	Under construction
310°E (50°W)	Unknown	INTELSAT IV-A (ATL 2)	INTELSAT	FSS	6/4	SPA-AJ/371/1509: 1°W SPA-AJ/213/1418: 18.5°W SPA-AA/66/1170 SPA-AA/49/1161
310°E (50°W)	1985 <sup>c</sup>	INTELSAT IV-A (ATL 2)	INTELSAT	FSS	6/4	AR11/C/140/1596
310°E (50°W)	1986	INTELSAT V-A (CONT 2)	INTELSAT	FSS	6,14,4,11	AR11/A/74/1586
310°E (50°W)	1986	INTELSAT IBS (310E)	INTELSAT	FSS	6,14/4,11,12	AR11/A/129/1617
(310°E (50°W)	30 Dec 1987/10	USASAT 13C	USA	FSS-Intern	14/11a,11.4a	AR11/A/134/1618

313°E (47°W)	30 Sep 1987/10	USASAT 13B	USA	FSS	14/11e,11.4a	AR11A/133/1618
315°E (45°W)	01 Jan 1988/10	USASAT 13F	USA	FSS-Intern	14,12a/11a,12d	AR11/A/154/1635
316.5°E (43.5°W)	31 Dec 1988/10	VIDEOSAT 3	France	FSS	14,2.0/11f,12d	AR11/A/148/1631
317°E (43°W)	01 Jun 1988/10	USASAT 13G	USA	FSS-Intern	14/12a,11a,12d	AR11/A/155/1635
319°E (41°W)	31 Dec 1988/10	USASAT 14A	USA	FSS	6/4	AR11/A/158/1637
319.5°E (40.5°W)	01 Apr 1986/10	INTELSAT V-A	INTELSAT	FSS	6,14/4,11	AR11/A/127/1617
319.5°E (40.5°W)	01 Apr 1986/10	INTELSAT IBS	INTELSAT	FSS	6a,14/4a,11d,11b, 12d	AR11/A/130/1617 (AR11/A/130 ADD-1/1628)
322.5°E (37.5°W)	1987/10	VIDEOSAT 2	France	FSS	14/2,12d	AR11/A/86/1589
322.5°E (37.5°W)	1987	USASAT 13A	USA	FSS	14/11,11a,4a	AR11/132/1618
325.5E (34.5°W)	1987	INTELSAT V-A (ATL 3)	INTELSAT	FSS	6,14/4,11	AR11/A/63/1580
325.5°E (34.5°W)	1985	INTELSAT MCS (ATL E)	INTELSAT	FSS/MMSS	1.6a,6.4a/1.5a, 4.1a,4.2	SPA-AJ/350/1500 SPA-AA/284/1432
329°E (31°W)	1986	UNISAT 1 ATL TELECOM	UK-Britain	FSS	14/11,12b,12d	AR11/A/26/1534 Also see entry below
329°E (31°W)	30 Jun 1986/10	UNISAT 1	UK	FSS/BSS	17c,17b,14a/12d, 2.2,4,11.7a,12e	AR11/C/576/1650 AR11/A/23/1532
329°E (31°W)	01 Jan 1987/10	INTELSAT V-A (ATL 6)	INTELSAT	FSS	6,14/4,11	AR11/A/119/1611 (AR11/A/119/ADD-1/1628) (AR11/A/119 ADD-2/1638)

TABLE 2 (continued). PLANNED GEOSTATIONARY SATELLITES FOR FIXED, BROADCAST,  
AND MARITIME-MOBILE SERVICES, LATE DECEMBER 1984

Subsatellite Longitude	Launch Date	Satellite Designation	Country or Organization	Function	Up/Down-Link Frequency (GHz)	Remarks
329°E (31°W)	01 Jan 1987/10	INTELSAT V (ATL 6)	INTELSAT	FSS	6,14/4,11	AR11/A/118/1611
332.5°E (27.5°W)	1985	INTELSAT V-A (ATL 2)	INTELSAT	FSS	6,14/4,11	SPA-AA/335/1478 AR11/C/123/1592
332.5°E (27.5°W)	01 Jan 1987/13	INTELSAT VI (ATL 2)	INTELSAT	FSS	5,6,14/3,4,11	AR11/A/70/1584
334°E (26°W)	31 Aug 1988/10	INMARSAT (AOR-Central)	UK	MMSS	1.6b,6.4b/1.5a, 3.9b,4c,3.6a	AR11/A/152/1634
335°E (25°W)	Unknown	LOUTCH P1	USSR	FSS	14/11	SP-AA/177/1289
335°E (25°W)	Unknown	STATSIONAR 8	USSR	FSS	6/4	SPA-AJ/62/1280
335°E (25°W)	Unknown	VOLNA 1	USSR	MMSS	UHF, 1.6b/ 1.5a, UHF	SPA-AA/169/1286
335°E (25°W)	Unknown	SIRIO 2	France	FSS/MSS	14,2.0/11,12d,2.2	AR11/A/148/1631
335.5°E (24.5°W)	Unknown	INTELSAT V-A (ATL 1)	INTELSAT	FSS	5,6,14/3,4,11	SPA-AA/334/1478 AR11/C/122/1592
335.5°E (24.5°W)	1987	INTELSAT VI (ATL 1)	INTELSAT	FSS	6,14/4,11	AR11/A/69/1584
335.5°E (24.5°W)	Unknown	INTELSAT MCS (ATL D)	INTELSAT	MMSS	1.6b,6.4b/1.5a,4g	SPA-AJ/349/1500
336°E (24°W)	Unknown	PROGNOZ 1	USSR	SRS	-/3,4	SPA-AA/316/1471

337°E (23°W)	Unknown	MARECS (ATL 2)	France	FSS/MMSS	1.6b,6.4b, UHF/1.5a,4d,UHF	SPA-AJ/241/1432 SPA-AA/219/1351 AR11/D/3/1551
338.5°E (21.5°W)	1986	INTELSAT V (ATL 5)	INTELSAT	FSS	6,14/4,11	SPA-AA/252/1419
338.5°E (21.5°W)	01 Jan 1989/10	INTELSAT V-A (338.5E)	INTELSAT	FSS	6,14/4,11	AR11/A/180/1645 SPA-AA/48/1161 SPA-AA/65/1170
340°E (20°W)	1985	GDL 4	Luxembourg	FSS/BSS	6.5-7,14/11,12d	AR11/A/92/1594
341°E (19°W)	1986	LUX-SAT	Luxembourg	BSS	17a/12b	AR11/A/20/1529
341°E (19°W)	1985	TDF 1	France	BSS	17a,12b	AR11/A/57/1570 AR11/C/107/1578
	01 Jun 1985	TDF 1 (17 GHz)	France	BSS	17b/-	AR11/C/142/1547 RR1042/2/1521
	01 Jun 1985/10	TDF 1 (11 GHz)	France	FSS/BSS	11.2a/-	AR11/C/124/1592 RR1042/2/1521
	01 Jun 1985/10	TDF 1 (2 GHz)	France	FSS/BSS	2.2/2.2	AR11/C/107/1578 RR1042/2/1521
341°E (19°W)	1985	L-SAT	ESA (France)	BSS/FSS	13a,14a,30a/12b, 20a	SPA-AA/308/1463 AR11/A/33/1544 AR11/A/88/1590 AR11/A/57/1570 AR11/C/124/1592
	01 Jul 1986	L-SAT (30/20 GHz)	France	FSS/FSS	27b/18a,29.6a	AR11/C/232/1619 AR11/A/32/1544
	01 Jul 1986	L-SAT (14,13 <sup>F</sup> /12 GHz)	France	BSS/FSS	14c,13c,12d	AR11/C/174/1605 AR11/C/174 ADD-1/1643 SPA-AA/337/1479 AR11/A/88/1590

TABLE 2 (continued). PLANNED GEOSTATIONARY SATELLITES FOR FIXED, BROADCAST, AND MARITIME-MOBILE SERVICES, LATE DECEMBER 1984

Subsatellite Longitude	Launch Date	Satellite Designation	Country or Organization	Function	Up/Down-Link Frequency (GHz)	Remarks
	01 Jul 1986/10	L-SAT (2/2 GHz)	France	BSS/FSS	2.0/2.2	AR11/C/176/1605 AR11/S/33/1544
341°E (19°W)	01 Dec 1985	L-SAT (17 GHz)	France	BSS	17a/-	AR11/C/6/1554 AR11/A/308/1463
341°E (19°W)	1986	HELVESAT 1	Switzerland	BSS	17a,18/12b,2	SPA-AA/365/1512
341°E (19°W)	1986	SARIT	Italy	BSS	17a,18/2b	SPA-AA/360/1505 SPA-AA/371/1547
341°E (19°W)	1985-86	TV-SAT	Federal Republic of Germany	BSS	17a,17.3a,18.0a, 2.0,11.7a,12e,2.0	SPA-AA/311/1464 SPA-AA/325/1474 SPA-AA/366/1526
341.5°E (18.5°W)		INTELSAT (ATL 2)	INTELSAT	FSS	6,14/4,11	SPA-AJ/218/1418 SPA-AA/119/1232
341.5°E (18.5°W)	1986-87	INTELSAT V-A (ATL 4)	INTELSAT	FSS	6,14/4,11	AR11/A/64/1580
341.5°E (18.5°W)	1986	INTELSAT IBS (341.5E)	INTELSAT	FSS	6,14/4,11,12a,12d	Under construction by Ford Aerospace; replaces INTELSAT V-A, above
342°E (18°W)	15 Oct 1989	SATCOM II	Belgium	FSS	8/7	SPA-AJ/137/1355 SPA-AA/144/1257
343.5°E (16.5°W)	01 Jan 1986/10	INTELSAT V (343.5E)	INTELSAT	FSS	6,14/4,11	AR11/A/172/1639
343.5°E (16.5°W)	01 Jul 1986/10	INTELSAT V-A (343.5E)	INTELSAT	FSS	6,14/4,11	AR11/A/170/1638
343.5°E (16.5°W)	01 Jul 1986/10	INTELSAT IBS (343.5E)	INTELSAT	FSS	6a,14/4a,11d,11b,12d	AR11/A/171/1638
344°E (16°W)	01 Jun 1986/20	WSDRN	USSR	FSS/SR	14d,11b,13	AR11/C/67/1570 SPA-AA/341/1484
345°E (15°W)	31 Aug 1985	INMARSAT (AOR-East)	UK	MMSS	16b,6.1a,6.4a, 6.4d/1.5a,3.9b, 4c,3.6a	AR11/A/153/1634
346°E (14.5°W)	Unknown	LOUTCH 1	USSR	FSS	14/11	SPA-AA/157/1262 SPA-AJ/84/1318
346°E (14°W)	31 Dec 1982	STATSIONAR 4	USSR	FSS	6.1b/3.8a	SPA-AJ/336/1494 SPA-AA/92/1197
346°E (14°W)	1980/10	VOLNA 2	USSR	MMSS	1.6c/1.5c	SPA-AJ/97/1329 SPA-AA/170/1286: 14°W
346.5°E (13.5°W)	Unknown	POTOK 1	USSR	FSS	-/4	SPA-AA/344/1485
347.5°E (12.5°W)	Unknown <sup>9</sup>	MAROTS-B	France	MMSS	1.6b, UHF/1.5a, UHF	SPA-AA/204/133
348°E (12°W)	Early 1988/10	HIPPARCOS	France	FSS/SR	2.0/2.2	AR11/A/138/1621
349°E (11°W)	Unknown	STATSIONAR 11	USSR	MMSS	5a/3	SPA-AJ/30/1469 SPA-AA/270/1425
349°E (11°W)	Unknown	STATSIONAR 11	USSR	FSS	6/4	SPA-AA/270/1425 SPA-AJ/303/1469
349°E (11°W)	1986	F-SAT 2	France	FSS	2,14,30a/12d,20a	AR11/C/466/1647 AR11/A/73/1586
355°E (5°W)	1985	TELECOM 1-B	France	FSS/BSS <sup>a</sup>	2,6,8,14/2.2 4,7,12b,12d	SPA-AJ/300/1461 AR11/C/128/1593
356°E (4°W)	01 Jul 1987/10	INTELSAT V (CONT 3)	INTELSAT	FSS	6,14/4,11	AR11/A/112/1609

TABLE 2 (continued). PLANNED GEOSTATIONARY SATELLITES FOR FIXED, BROADCAST,  
AND MARITIME-MOBILE SERVICES, LATE DECEMBER 1984

Subsatellite Longitude	Launch Date	Satellite Designation	Country or Organization	Function	Up/Down-Link Frequency (GHz)	Remarks
356°E (4°W)	01 Jul 1986/10	INTELSAT V-A (CONT 3)	INTELSAT	FSS	6.14/4.11	AR11/A/1116/1609 AR11/A/1116 ADD-1/1628 (AR11/A/1116 ADD-2/1638)
359°E (1°W)	1986	INTELSAT V (CONT 4)	INTELSAT	FSS	6.14, 4.11	SPR-A/J/371/1509
359°E (1°W)	01 Jan 1987/10	INTELSAT V-A (CONT 4)	INTELSAT	FSS	6.14, 4.11	AR11/A/1117/1609, (AR11/117 ADD-1/1628) (AR11/117 ADD-2/1638) AR11/A/117ADD-2/1638

<sup>a</sup>Community BSS only.

<sup>b</sup>/10 implies a 10-year life in orbit.

<sup>c</sup>Radio location service.

<sup>d</sup>Already launched; moves to new location at date shown.

<sup>e</sup>Either CONT 1 or 307E will be operated at this location.

<sup>f</sup>This frequency band is not on the coordination request.

<sup>g</sup>Launch failed; no current plans to replace.

TABLE 3. FREQUENCY BAND KEY WITH SERVICE ALLOCATIONS<sup>a</sup>

Frequency Abbreviation	ITU Frequency Band (GHz)	Service	Link Direction
UHF	0.13-1.5		Up or Down <sup>b</sup>
1.5a	1.530-1.535 1.535-1.544	MMSS MMSS	
1.5b	1.535-1.5425	MMSS	Down
1.5c	1.536275-1.536525 1.543575-1.543825	MMSS MMSS	Down
1.5d	1.537-1.541 1.5148-1.541515	MMSS	Down
1.6a	1.610-1.6265	MMSS	Up
1.6b	1.6265-1.6455	MMSS	Up
1.6c	1.63775-1.638025 1.652245-1.652595	MMSS MMSS	Up
1.6d	1.6385-1.6425	MMSS	Up
2._	Various 2-GHz Frequencies		Up or Down <sup>b</sup>
2.5	2.5-1.69	BSS	Down
3	3.400-3.950	BSS	
3.6a	3.6-3.621	FSS/MSS Feeder	Down
3.8a	3.800-3.850	FSS	Down
3.9a	3.945-3.946 3.954-3.955	FSS FSS	Down
3.9b	3.945-3.955	MMSS/FSS	Down
4	3.700-4.200	FSS	Down

TABLE 3 (continued). FREQUENCY BAND KEY WITH SERVICE ALLOCATIONS<sup>a</sup>

Frequency Abbreviation	ITU Frequency Band (GHz)	Service	Link Direction
4a	3.700-4.100	FSS	Down
4b	4.175-4.200	FSS/MMSS Feeder	Down
4c	4.175-4.200	FSS/MMSS Feeder	Down
4d	4.188-4.2005	FSS/MMSS Feeder	Down
4e	4.1925-4.200	FSS/MMSS Feeder	Down
4f	4.195-4.200	FSS/MMSS Feeder	Down
4g	4.195-4.2005	FSS/MMSS Feeder	Down
4.1a	4.195-4.199	FSS/MMSS Feeder	Down
4.1b	4.195-4.199	FSS/MMSS Feeder	Down
4.2a	4.200-4.250	FSS/MMSS Feeder	Down
5	5.725-5.925	FSS	Up
5a-6	5.725-6.225	FSS	Up
5b-6	5.925-6.300	FSS	Up
5c-6	5.925-6.925	FSS	Up
5.1a	5.116875-5.133125	FSS	Down
6	5.925-6.425	FSS	Up

TABLE 3 (continued). FREQUENCY BAND KEY WITH SERVICE ALLOCATIONS<sup>a</sup>

Frequency Abbreviation	ITU Frequency Band (GHz)	Service	Link Direction
6.1a	6/170-6.180	MMSS/FSS	Up
6.1b	6.125-6.175	FSS	UP
6.1c	6.1725-6.1765	FSS/MMSS Feeder	Up
6.4a	6.409-6.425	FSS/MMSS Feeder	Up
6.4b	6.417-6.425	FSS/MMSS Feeder	Up
6.4c	6.420-6.424	FSS/MMSS Feeder	Up
6.4d	6.425-6.441	MMSS/FSS Feeder	Up
6.4e	6.420-6.425	FSS/MMSS Feeder	Up
6.5a	6.524875-6.541125	FSS, RD <sup>c</sup>	Up
7	7.25-7.49	FSS	Down
8	7.975-8.165	FSS	Up
11	10.700-11.700	FSS	Down
11a	10.7-11.2	FSS	Down
11b	10.7-11.5	FSS, SRSD <sup>d</sup>	Down
11c	10.905-11.200	FSS	Down
11d	10.950-11.65	FSS	Down
11e	10.950-11.200	FSS	Down
11f-12	11.700-11.950	FSS	Down

TABLE 3 (continued). FREQUENCY BAND KEY WITH SERVICE ALLOCATIONS<sup>a</sup>

Frequency Abbreviation	ITU Frequency Band (GHz)	Service	Link Direction
11.2a	11.2 $\pm$ 500 Hz	FSS	Up
11.4a	11.45-11.47	FSS	Down
11.7a-12	11.7-11.714	FSS	Down
12a	11.7-12.2	FSS <sup>e</sup>	Down
12b	11.7-12.5	BSS <sup>f</sup>	Down
12c	12.2-12.7	BSS <sup>e</sup>	Down
12d	12.5-12.75	FSS <sup>f</sup>	Down
12e	12.487-12.500	FSS, BSS	Down
13a	13.0-13.25	FSS, SRS	Down
13b	13.25-14.0	SRC <sup>d</sup>	Up
13c	13.16-13.31	FSS, BSS	Up
14	14.0-14.5	FSS	Up
14a	14.0-14.9	FSS	Up
14b	14.0-14.25	FSS	Up
14c	14.09-14.32	FSS	UP
14d	14.5-15.5	SRS <sup>d</sup>	Up
14e	14.5-14.8	FSS	Up
17a	17.3-18.1	FSS, BSS Feeder	Up
17b	17.3-17.65	FSS	Up

TABLE 3 (continued). FREQUENCY BAND KEY WITH SERVICE ALLOCATIONS<sup>a</sup>

Frequency Abbreviation	ITU Frequency Band (GHz)	Service	Link Direction
17c	17.37-18.0	RSS	Up
17d	17.7-20.0	FSS	Down
17.3a	17.3-17.314	FSS	Up
17.3b	17.30-17.303	FSS	Up
18a-1a	18.9-19.8	FSS, BSS	Down
18.0a	18.089-18.1	FSS	UP
20	20.2-21.2	FSS	Down
27a	27.5-30.0	FSS	Up
27b	27.99-28.69	FSS	Up
29.6a	29.655-29.656	FSS, BSS	Down
30	30.0-31.0	FSS	Down
39a	39.5-40.0	FSS	Up
43a	43.5-47	MSS	Not specified
49	49.0-50.0	FSS	Up

<sup>a</sup>If regions (ITU) are not shown, the allocation is worldwide.

<sup>b</sup>See Tables 1 and 2.

<sup>c</sup>Radiolocation applications.

<sup>d</sup>Secondary.

<sup>e</sup>Region 2.

<sup>f</sup>Regions 1 and 3.

portadores, se registró una movilidad de 8500 cm<sup>2</sup>/V-s. Estas características de la capa implantada corresponden a un coeficiente de compensación calculado de aproximadamente el 10 por ciento, cifra que se encuentra entre las más bajas logradas con la implantación iónica. Este estudio se llevó a cabo utilizando diferentes substratos de arseniuro de galio (GaAs) semiaislante cultivados mediante técnicas de encapsulado líquido Czochralski (LEC), tanto a baja como a alta presión. Los resultados revelan como los efectos de substrato dependen de la calidad de las características de la capa implantada.

### **Simulación de la dinámica del despliegue en los sistemas de soporte y antena de transmisión y recepción para los satélites Intelsat VI**

P. K. JAMES

#### **Abstracto**

EL INTELSAT VI es uno de los satélites de telecomunicaciones comerciales más grandes que se están fabricando actualmente. Sus dos sistemas de antenas transmisoras y receptoras de 4 y 6 GHz permanecen plegados durante el lanzamiento y posteriormente son desplegados hasta alcanzar su forma definitiva en órbita. La dinámica del despliegue de ambos sistemas es simulada con ayuda del programa de computadora de propósito general NBOD2 sobre dinámica. La plataforma estacionaria del satélite y los dos sistemas de antenas adoptan la configuración de cinco cuerpos acoplados por medio de bisagras cardánicas, formando un árbol topológico. En cada caso, el mecanismo de despliegue consta de un resorte negador integral con un activador amortiguado por fluido viscoso. Los pares torsores que generan estos mecanismos son pasados por el programa a lo largo del eje de la bisagra. Para comenzar, cada eje de bisagra es bloqueado y luego liberado durante la simulación a medida que comienza el despliegue. También se prepararon modelos de los efectos de la inercia y la energía cinética. Los resultados de la simulación proporcionan información a intervalos de fracciones de segundo sobre el ritmo de despliegue, aceleración, pares torsores, momento angular, energía cinética, tiempo de enganche y velocidad de enganche relacionados con cada sistema. Los resultados luego se correlacionan con datos empíricos preliminares obtenidos de modelos técnicos en los que se realizaron pruebas de duración con inercia de sistema y sin ella. Los adelantos más importantes logrados con este programa de simulación han sido predecir el funcionamiento de ambos sistemas de despliegue, establecer la simulación como herramienta para el diseño definitivo del mecanismo de despliegue y la simulación satisfactoria de activadores amortiguados con fluido viscoso.

## **Author Index, CTR 1984**

The following index gives the code numbers that are to be used for ordering reprints from Lab Records, COMSAT Laboratories, 22300 Comsat Drive, Clarksburg, MD 20871.

- AGARWAL, A., see McCoskey, J. S. [CTR84/260]  
 AKERMAN, S., see Szarvas, G. G. [CTR84/273].  
 ASSAL, F. T., see Potukuchi, J. R. [84CTR274].  
 ATOHOUN, I. G., see Chou, S. M. [CTR84/275].  
 BENNETT, J. A., "Drop-Size Distribution: Cross-Polarization Discrimination and Attenuation for Propagation Through Rain" *COMSAT Technical Review*, Vol. 14, No. 1, Spring, pp. 113-136 [CTR84/264].  
 BERMAN, A. L., Helgert, H. J.,\* and Berman, N. G.,\* "Equivalence Classes of Alternant Codes," *COMSAT Technical Review*, Vol. 14, No. 2, Fall, pp. 313-338 [CTR84/271].  
 BINCKES, J. B., see Schnicke, W. R. [CTR84/272].  
 BRANDEL, D. L., and Klein, L., "A Derivation of the Boundary of the Glistening Region for Rough Surface Scatter," *COMSAT Technical Review*, Vol. 14, No. 1, Spring, pp. 165-167 [CTR84/266].  
 CHAKRABORTY, D., Ehrmann, J., and McCune, E. W., "Wideband Klystron High-Power Amplifiers for FDM/FM/FDMA Applications," *COMSAT Technical Review*, Vol. 14, No. 1, Spring, pp. 53-82 [CTR84/262].  
 CHOU, S. M., Atohoun, I. G., Ross, P. B., Urcuyo, M. J., and Johnson, R. R., "10-W Solid-State Power Amplifier for C-Band TWTA Replacement," *COMSAT Technical Review*, Vol. 14, No. 2, Fall, pp. 431-444 [CTR84/275].  
 EHRMANN, J., see Chakraborty, D., [CTR84/262].  
 ELATI, E., "Reducing the Effects of Structural Modes on the Performance of Attitude Control Systems," *COMSAT Technical Review*, Vol. 14, No. 2, Fall, pp. 445-466 [CTR84/276].  
 EZZEDDINE, A., and Hung, H-L. A., "A K-Band Distributed Microstrip Termination," *COMSAT Technical Review*, Vol. 14, No. 2, Fall, pp. 467-480 [CTR84/277].

\*Non-COMSAT author.

- HAGMANN, W. C., "Carrier Synchronizer for Overlapped Raised Cosine Pulse Amplitude Modulation," *COMSAT Technical Review*, Vol. 14, No. 1, Spring, pp. 25-52 [CTR84/261].
- HERSEY, W. J., see Snyder, J. S. [CTR84/270].
- HUNG, B., see McCoskey, J. S. [CTR84/260].
- HUNG, H-L. A., see Ezzeddine, A. [CTR84/277].
- JOHNSON, R. R., see Chou, S. M. [CTR84/275].
- KLEIN, L., see Brandel, D. L. [CTR84/266].
- LEWIS, D. H., see Schnicke, W. R. [CTR84/272].
- MACKENTHUN, K. M., "Block Orthogonal Convolutional Coding for the INTELSAT TDMA Data Channel," *COMSAT Technical Review*, Vol. 14, No. 2, Fall, pp. 261-284 [CTR84/269].
- MCCOSKEY, J. S., Redman, W., Morgart, W., Hung, B., and Agarwal, A., "An International High-Speed Packet-Switching Experiment," *COMSAT Technical Review*, Spring, Vol. 14, No. 1, pp. 1-24 [CTR84/260].
- MCCUNE, E. W., see Chakraborty, D. [CTR84/262].
- MORGART, W., see McCoskey, J. S. [CTR84/260].
- MOTT, R. C., see Potukuchi, J. R. [CTR84/274].
- POKLEMBBA, J. J., "A Joint Estimator-Detector for QPSK Data Transmission," *COMSAT Technical Review*, Vol. 14, No. 2, Fall, pp. 211-259 [CTR84/268].
- POTUKUCHI, J. R., Assal, F. T., and Mott, R. C., "A Computer-Controlled Communications Satellite Monitoring System for Time Division Multiple Access," *COMSAT Technical Review*, Vol. 14, No. 2, Fall, pp. 391-430 [CTR84/274].
- REDMAN, W., see McCoskey, J. S. [CTR84/260].
- ROSS, P. B., see Chou, S. M. [CTR84/275].
- SANDRIN, W. A., "Land-Mobile Satellite Start-Up Systems," *COMSAT Technical Review*, Vol. 14, No. 1, Spring, pp. 137-164 [CTR84/265].
- SCHMITT, C. H., "Geosynchronous Satellite Log," *COMSAT Technical Review*, Vol. 14, No. 1, Spring, pp. 169-189 [CTR84/267].
- SCHNICKE, W. R., Binckes, J. B., and Lewis, D. H., "Transponder Supply/Demand Analysis for the Geostationary Orbit," *COMSAT Technical Review*, Vol. 14, No. 2, Fall, pp. 339-368 [CTR84/272].
- SHIU, M. R., see Szarvas, G. G. [CTR84/273].
- SNYDER, J. S., and Hersey, W. J., "Pseudo-Bit-Error-Rate Measurement for 120-Mbit/s TDMA," *COMSAT Technical Review*, Vol. 14, No. 2, Fall, pp. 285-311 [CTR84/270].

- STRUHARIK, S. J., "Cross-Polarization Measurements at 4 and 6 GHz in the INTELSAT V System," *COMSAT Technical Review*, Vol. 14, No. 1, Spring, pp. 83-111 [CTR84/263].
- SZARVAS, G. G., Akerman, S., and Shiu, M. R., "Measurement of Data Activity on Satellite Carrier VF Channels," *COMSAT Technical Review*, Vol. 14, No. 2, Fall, pp. 369-390 [CTR84/273].
- URCUYO, M. J., see Chou, S. M. [CTR84/275].

## **Index of 1984 Publications by COMSAT Authors**

The following is a cross-referenced index of publications by COMSAT authors in 1984, not including papers published in the *COMSAT Technical Review*. The code number at the end of each entry is the reprint number by which copies may be ordered from Lab Records, COMSAT Laboratories, 22300 Comsat Drive, Clarksburg, MD 20871.

- ARNDT, R. A., see Meulenberg, A. [84CLR10].  
 ARNSTEIN, D. S., see Suyderhoud, H. [84CLR09].  
 ATIA, A. E., see LEE, Y. S. [84CLR55].  
 BAKER, W. E., and Sizemore, W. T., "Design of a Lightweight High-Voltage Spacecraft Power Conditioner," 11th Annual International Power Electronics Conference, Dallas, TX, April 10-12, 1984, *Proc.*, Session G, Paper 2, pp. 1-7 [84CLR44].  
 BAKER, W. E., see Billerbeck, W. J. [84CLR42].  
 BARGELLINI, P. L., "A Reassessment of Satellite Communications in the 20 and 30 GHz Bands," *International Journal of Satellite Communications*, Vol. 2, No. 2, April-June 1984, pp. 101-106 [84CLR41].  
 BARGELLINI, P. L., Kaiser, J.,\* and Dicks, J. L.,\* "International Teleconferencing via INTELSAT Satellites," ICC '84: International Conference on Communications, Amsterdam, The Netherlands, May 14-17, 1984, *Links for the Future*, P. Dewilde and C. A. May, Editors, pp. 1541-1545 [84CLR16].  
 BENNETT, J. A., "Propagation Through an Assembly of Anisotropic Electric and Magnetic Dipole Scatterers," *Radio Science*, Vol. 19, No. 5, September-October 1984, pp. 1376-1388 [84CLR24].  
 BENNETT, J. A.,\* Fang, D. J., and Boston, R. C.,\* "The Relationship between  $N_0$  and  $\lambda$  for Marshall-Palmer-Type Raindrop Size Distributions," *Journal of Climate and Applied Meteorology*, Vol. 23, No. 5, May 1984, pp. 768-771 [84CLR15].  
 BILLERBECK, W. J., "Minimizing Spacecraft Power Loss due to Single-Point Failures," 19th Intersociety Energy Conversion Engineering Conference, San Francisco, CA, August 19-24, 1984, *Proc.*, Vol. 1, pp. 345-356 [84CLR35].

\*Non-COMSAT author.

- BILLERBECK, W. J., and Baker, W. E., "Design of Reliable Power Systems for Communications Satellites," AIAA/NASA Space Systems Technology Conference, Costa Mesa, CA, June 5-7, 1984, *Technical Papers*, pp. 67-79 [84CLR42].  
 BILLERBECK, W. J., see Ijichi, K. [84CLR03].  
 BONETTI, R. R., and Williams, A. E., "Narrow Bandpass Filters Using the High-Q Cylindrical  $TE_{0m}$  Resonator Modes," IEEE MTT-S International Microwave Symposium, San Francisco, CA, May 30-June 1, 1984, *Digest*, pp. 288-289 [84CLR26].  
 BONETTI, R. R., see Williams, A. E. [84CLR27].  
 BUSH, W. G., see Williams, A. E. [84CLR27].  
 CAHANA, D., "Practical Aspects of Predistortion Diode Linearizers for Satellite Transponders," 14th European Microwave Conference, Liege, Belgium, September 10-13, 1984, *Proc.*, pp. 112-117 [84CLR43].  
 CAMPANELLA, S. J., and Harrington, J. V., "Satellite Communications Networks," *Proc. IEEE*, Vol. 72, No. 11, November 1984, pp. 1506-1519 [84CLR33].  
 CAMPANELLA, S. J., see Inukai, T. [84CLR13].  
 CARPENTER, E. W., "Dual-Band Smooth-Wall Conical Horn with Low Cross-Polarization," IEEE AP-S International Symposium on Antennas and Propagation, Boston, MA, June 25-29, 1984, *Digest*, Vol. 2, pp. 591-594 [84CLR20].  
 CHAHINE, K. A., "Regional Satellite System Design for Reduced Earth Station Cost and Increased Transponder Capacity," AIAA 10th Communication Satellite Systems Conference, Orlando, FL, March 19-22, 1984, *A Collection of Technical Papers*, pp. 413-420 [84CLR14].  
 CHANG, P. Y., "Satellite Channel Modeling Program for Coded Octal PSK Modulation Using a Viterbi Decoder," Symposium on Analysis and Simulation Software for Satellite Communications, Clarksburg, MD, November 15, 1984, *Proc.*, pp. 79-101 [84CLR47].  
 CHANG, P. Y., see Rhodes, S. A. [84CLR54].  
 CHEN, C. H., Tulintseff, A., and Sorbello, R. M., "Broadband Two-Layer Microstrip Antenna," IEEE AP-S International Symposium on Antennas and Propagation, Boston, MA, June 25-29, 1984, *Digest*, Vol. 1, pp. 251-254 [84CLR18].  
 COOK, W. L., "An Overview of Satellite System Modeling and Simulation," Symposium on Analysis and Simulation Software for Satellite Communications, Clarksburg, MD, November 15, 1984, *Proc.*, pp. 1-3 [84CLR45].  
 COOK, W. L., see Meadows, D. [84CLR46].  
 CORCORAN, F. L., see Suyderhoud, H. [84CLR09].

- DAVIES, D. E.,\* and McNally, P. J., "Enhanced Activation of Zn-Implanted GaAs," *Applied Physics Letters*, Vol. 44, No. 3, February 1, 1984, pp. 304-306 [84CLR05].
- EARL, M. W., and Noble, T. F., "Electrochemical Impregnation Bath Aging," *Journal of Power Sources*, Vol. 12, No. 3-4, July/August 1984, pp. 277-285 [84CLR08].
- EAVES, R. E., and Kolba, D. P.,\* "Unified Multiple-Beam Uplink Configuration for EHF Satellite Communications," *Journal of Spacecraft and Rockets*, Vol. 21, No. 1, January-February 1984, pp. 108-112 [84CLR02].
- FANG, D. J., see Bennett, J. A. [84CLR15].
- GELLER, B. D., and Zaghoul, A. I., "An MMIC/MIC-to-Waveguide Transition for Single- and Dual-Polarization Systems," IEEE MTT-S International Microwave Symposium, San Francisco, CA, May 30-June 1, 1984, *Digest*, pp. 412-413 [84CLR29].
- GETSINGER, W. J., see Gupta, R. K. [84CLR28].
- GHOSH, K. K., see Lec, B. S. [84CLR50].
- GREENE, K. H., see Paul, D. K. [84CLR55], [84CLR12].
- GUPTA, R. K., and Getsinger, W. J., "Quasi-Lumped-Element 3- and 4-Port Networks for MIC and MMIC Applications," IEEE MTT-S International Microwave Symposium, San Francisco, CA, May 30-June 1, 1984, *Digest*, pp. 409-411 [84CLR28].
- HAMID, A., "Channel Modeling and Simulation Program (CHAMP)," Symposium on Analysis and Simulation Software for Satellite Communications, Clarksburg, MD, November 15, 1984, *Proc.*, pp. 151-195 [84CLR48].
- HAN, W. K., and Hemmati, F., "Punctured PN Codes," *Electronics Letters*, Vol. 20, No. 12, June 7, 1984, pp. 494-495 [84CLR32].
- HARRINGTON, J. V., see Campanella, S. J. [84CLR33].
- HEMMATI, F., see Han, W. K. [84CLR32].
- HYDE, G., "Microwave Propagation," *Antenna Engineering Handbook*, 2nd ed., R. C. Johnson and H. Jasik, Editors, New York: McGraw-Hill, 1984, pp. 45-1-45-17 [84CLR53, reprint permission pending].
- HYDE, G., "Utilization of Frequency Spectrum by Commercial Communications Satellite Systems," 2nd Deep Space Sensor Surveillance Workshop, M.I.T. Lincoln Laboratory, Lexington, MA, April 3-5, 1984.
- HYDE, G., see Kelleher, K. S. [84CLR52].

\*Non-COMSAT author.

- IJICHI, K.,\* and Billerbeck, W. J., "Capacitor Bank Charging by Series-Parallel Switching of Solar Arrays," *Journal of Spacecraft and Rockets*, Vol. 21, No. 2, March-April 1984, pp. 196-201 [84CLR03].
- INUKAI, T., and Campanella, S. J., "ACTS TDMA Network Control," AIAA 10th Communication Satellite Systems Conference, Orlando, FL, March 19-22, 1984, *A Collection of Technical Papers*, pp. 188-195 [84CLR13].
- IRWIN, D. L., Main, E. L., and Smagala, T. J.,\* "INTELSAT V Attitude Determination and Control Subsystem Flight Simulator Architecture," IEEE Symposium on Analysis and Simulation Software for Satellite Communications, Clarksburg, MD, November 15, 1984, *Proc.*, pp. 322-348 [84CLR51].
- JACOBUS, N. M., "Designing Power Line Transient Protection Circuits," POWERCON 11: 11th Annual International Power Electronics Conference, Dallas, TX, April 10-12, 1984, *Proc.*, Session D, Paper 4, pp. 1-11 [84CLR22].
- KELLEHER, K. S.,\* and Hyde, G., "Reflector Antennas," *Antenna Engineering Handbook*, 2nd ed., R. C. Johnson and H. Jasik, Editors, New York: McGraw-Hill, 1984, pp. 17-1-17-54 [84CLR52, reprint permission pending].
- KING, C., Jankowski, J.,\* Duesing, R.,\* Roach, P.,\* and Trusty, P., "INTELSAT TDMA/DSI Burst Time Plan Development," Symposium on Analysis and Simulation Software for Satellite Communications, Clarksburg, MD, November 15, 1984, *Proc.*, pp. 196-226 [84CLR49].
- KIRKENDALL, T. D., see Remmel, T. P. [84CLR07].
- KOEPF, G. A., "Optical Processor for Phased-Array Antenna Beam Formation," SPIE '84 Technical Symposium East, Arlington, VA, April 29-May 4, 1984, *Proc.*, SPIE Vol. 477, Optical Technology for Microwave Applications, pp. 75-81 [84CLR23].
- KOEPF, G. A., "Technologies for Intersatellite Optical Communications," ESA Workshop on Space Laser Applications and Technology, Les Diablerets, Switzerland, March 26-30, 1984, *Proc.*, ESA SP-202, pp. P71-P76 [84CLR11].
- KOEPF, G. A., and Markey, B. J., "Fabrication and Characterization of a 2-D Fiber Array," *Applied Optics*, Vol. 23, No. 20, October 15, 1984, pp. 3515-3516 [84CLR34].
- KOEPF, G. A., and Molz, J. L., "Compact Optical Beam-Forming System for Large Phased-Array Antennas," MILCOM '84: IEEE Military Com-

\*Non-COMSAT author.

- munications Conference, Los Angeles, CA, October 21-24, 1984, *Conference Record*, Vol. 2, pp. 335-337 [84CLR25].
- KOEPPF, G. A., see Paul, D. K. [84CLR12].
- LEE, B. S., and Ghosh, K. K., "Simulation Software for Analysis of Multiple-Beam Reflector Antenna Systems," Symposium on Analysis and Simulation Software for Satellite Communications, Clarksburg, MD, November 15, 1984, *Proc.*, pp. 227-259 [84CLR50].
- LEE, B. S., and Siddiqi, S., "Multiple Scanning and Multiple Spot Beam Antenna Designs for CONUS Coverage," IEEE AP-S International Symposium on Antennas and Propagation, Boston, MA, June 25-29, 1984, *Digest*, Vol. 1, pp. 147-150 [84CLR17].
- LEE, Y. S., Atia, A. E., and Subran, F., "Technology Assessment for Improved Orbit/Spectrum Efficiency," IEEE Global Telecommunications Conference, Atlanta, GA, November 26-29, 1984, *Digest*, Vol. 1, pp. 97-104 [84CLR55].
- LEWIS, H., see Suyderhoud, H. [84CLR09].
- LYONS, J. W., "An Improved Technique for Prediction and Analysis of Solar Array Performance for Geosynchronous Spacecraft," 19th Intersociety Energy Conversion Engineering Conference, San Francisco, CA, August 19-24, 1984, *Proc.*, Vol. 1, pp. 464-470 [84CLR36].
- MAIN, E. L., see Irwin, D. L. [84CLR51].
- MARKEY, B. J., "High-Speed Photodetector Switching," 1st International Conference of Integrated Optical Circuit Engineering, Cambridge, MA, October 23-25, 1984, *Proc.*, SPIE Vol. 157, pp. 242-245 [84CLR39].
- MARKEY, B. J., see Koepf, G. A. [84CLR34].
- McNALLY, P. J., "Ion Implantation of Boron in GaAs MESFETs," *IEEE Electron Device Letters*, Vol. EDL-5, No. 4, April 1984, pp. 126-128 [84CLR04].
- McNALLY, P. J., see Davies, D. E. [84CLR05].
- MEADOWS, D., and Cook, W. L., "Systems Analysis Software," Symposium on Analysis and Simulation Software for Satellite Communications, Clarksburg, MD, November 15, 1984, *Proc.*, pp. 21-51 [84CLR46].
- MEULENBERG, A., "Evidence for a Permanent Single-Event Upset Mechanism," *IEEE Transactions on Nuclear Science*, Vol. NS-31, No. 6, December 1984, pp. 1280-1283 [84CLR30].
- MEULENBERG, A., Arndt, R. A., and Tyler, J. U., "Structurally Stable, Thin Silicon Solar Cells," *IEEE Transactions on Electron Devices*, Vol. ED-31, No. 5, May 1984, pp. 720-721 [84CLR10].
- MEULENBERG, A., see Parker, L. W. [84CLR31].
- MOLZ, J. L., see Koepf, G. A. [84CLR25].

- NOBLE, T. F., see Earl, M. W. [84CLR08].
- PALMER, L. C., "Computer Modeling and Simulation of Communications Satellite Channels," *IEEE Journal on Selected Areas in Communications*, Vol. SAC-2, No. 1, January 1984, pp. 89-102 [84CLR01].
- PARKER, L. W.,\* and Meulenbergh, A., "Theory of Radiation-Induced and Carrier-Enhanced Conductivity: Space Charge and Contact Effects," *IEEE Transactions on Nuclear Science*, Vol. NS-31, No. 6, December 1984, pp. 1368-1374 [84CLR31].
- PAUL, D. K., "Prospects for Undersea Fiberoptic Cable Communications Systems," *Laser Focus/Electro-Optics*, Vol. 20, No. 10, October 1984, pp. 175-177 [84CLR40].
- PAUL, D. K., and Greene, K. H., "Reliability of 1.3- $\mu\text{m}$  InGaAsP/InP Laser Diodes," *Fiber and Integrated Optics*, Vol. 5, No. 1, 1984, pp. 23-63 [Available as 82CLR55].
- PAUL, D. K., Greene, K. H., and Koepf, G. A., "Undersea Fiber Optic Cable Communications System of the Future: Operational, Reliability, and Systems Considerations," *IEEE Journal of Lightwave Technology*, Vol. LT-2, No. 4, August 1984, pp. 414-425 [84CLR12].
- POLLACK, L., and Weiss, H., "Communications Satellites: Countdown for INTELSAT VI," *Science*, Vol. 223, No. 4636, February 10, 1984, pp. 553-559 [84CLR06].
- RAPPAPORT, C. M., and Zaghoul, A. I., "Optimized Three-Dimensional Lenses for Two-Dimensional Scanning," IEEE AP-S International Symposium on Antennas and Propagation, Boston, MA, June 25-29, 1984, *Digest*, Vol. 2, pp. 608-611 [84CLR21].
- REMMEL, T. P., and Kirkendall, T. D., "Quantitative Analysis of Positive Battery Plates by Means of BSE Image Analysis," *Microbeam Analysis 1984*, A. D. Romig, Jr., and J. I. Goldstein, Editors, 1984, pp. 165-168 [84CLR07].
- RHODES, S. A., and Chang, P. Y., "Coded M-Ary Modulation for FDMA Satellite Communications," IEEE Global Telecommunications Conference, Atlanta, GA, November 26-29, 1984, *Conf. Rec.*, pp. 726-734 [84CLR54].
- ROGERS, D. V., and Allnut, J. E.,\* "Evaluation of a Site Diversity Model for Satellite Communications Systems," *IEE Proc.*, Part F, Vol. 131, No. 5, August 1984, pp. 501-506 [84CLR38].
- SIDDIQI, S., see Lee, B. S. [84CLR17].
- SIZEMORE, W. T., see Baker, W. E. [84CLR44].
- SORBELLO, R. M., see Chen, C. H. [84CLR18]; Zaghoul, A. I. [84CLR19].

\*Non-COMSAT author.

- STOCKEL, J. F., "Geosynchronous Performance of Nickel-Hydrogen Cells," 19th Intersociety Energy Conversion Engineering Conference, San Francisco, CA, August 19-24, 1984, *Proc.* pp. 464-470 [84CLR37].
- STOCKEL, J. F., see Vaidyanathan, H. [83CLR80].
- SUBRAN, F., see LEE, Y. S. [84CLR55].
- SUYDERHOUD, H., Corcoran, F. L., Arnstein, D. S., and Lewis, H. "Investigation of 9.6 kb/s Data Transmission via a PCM Link at 64 kb/ With and Without Link Errors," *International Journal of Satellite Communications*, Vol. 2, No. 1, January-March 1984, pp. 81-87 [84CLR09].
- SUYDERHOUD, H., see Williams, G. [84CLR56].
- TRUSTY, P., see King, C. [84CLR49].
- TULINTSEFF, A., see Chen, C. H. [84CLR18].
- TYLER, J. U., see Meulenberg, A [84CLR10].
- VAIDYANATHAN, H., and Stockel, J. F., "Gas-Permeable Microporous Separator for Ni-H<sub>2</sub> Cells," Symposium on Advances in Battery Material and Processes, 1984, *Proc.*, J. McBreen, Editor, Vol. 84-4, pp. 198-20 [Available as 83CLR80].
- WEISS, H., see Pollack, L. [84CLR06].
- WILLIAMS, A. E., Bush, W. G., and Bonetti, R. R., "Predistortion Techniques for Multicoupled Resonator Filters," IEEE MTT-S International Microwave Symposium, San Francisco, CA, May 30-June 1, 1984, *Digest*, pp. 290-291 [84CLR27].
- WILLIAMS, A. E., see Bonetti, R. R. [84CLR26].
- WILLIAMS, G.,\* and Suyderhoud, H., "Subjective Performance Evaluation of the 32-kbit/s ADPCM Algorithm," IEEE Global Telecommunication Conference, Atlanta, GA, November 26-29, 1984, *Digest*, Vol. 2, pp. 778-785 [84CLR56].
- ZAGHLOUL, A. I., and Sorbello, R. M., "20-GHz Phased Array Feeder Reflector Antennas With Distributed MMIC Modules," IEEE AP-International Symposium on Antennas and Propagation, Boston, MA, June 25-29, 1984, *Digest*, Vol. 1, pp. 441-444 [84CLR19].
- ZAGHLOUL, A. I., see Geller, B. D. [84CLR29]; Rappaport, C. M. [84CLR21].

---

\*Non-COMSAT author.